

PERFORMANCE INVESTIGATION OF ROTARY TABLES IN LARGE-SCALE
METROLOGY

by

Qichang Wang

A dissertation submitted to the faculty of
The University of North Carolina at Charlotte
in partial fulfillment of the requirements
for the degree of Doctor of Philosophy in
Mechanical Engineering

Charlotte

2019

Approved by:

Dr. Gert Goch

Dr. Jimmie A. Miller

Dr. Christopher J. Evans

Dr. Edward P. Morse

Dr. Stuart T. Smith

Dr. M. Yasin Raja

ABSTRACT

QICHANG WANG. Performance investigation of rotary tables in large-scale metrology.
(Under the direction of DR.-ING. GERT GOCH)

Rotary tables significantly improve the flexibility and efficiency of multi-axis measuring devices and multi-axis machining centers by providing a quick positioning of workpieces. Large-scale rotary tables are designed and produced for increasing demands of measuring volume and load capacity in industries, such as wind energy, aerospace and shipbuilding. Although the performances of rotary tables have been improved, there still exist non-trivial error motions. Moreover, it is not clear whether and how the error motions of a rotary table change under various loads. The traditional calibration methods are not suitable to investigate the mentioned issues because of their complicated and nonflexible setups.

A new calibration solution which provided a simple, quick and flexible setup, as well as a fully-automated measurement process, was proposed. The rotary table, the 3-axis measuring device and the artifact (circular ball plate) were calibrated simultaneously. A mathematical solution was developed, which covers all the deviation sources, occurring at the movement of a rotary axis. This solution was verified and validated by numerical simulations and by experimental comparison with a traditional method. The stability of this solution was investigated using the Monte Carlo simulation. The behaviors of rotary tables under symmetric and asymmetric loads were investigated experimentally. The simple calibration setup and developed evaluation procedure enabled a compensation of rotary table/axis deviations in a wide application field.

ACKNOWLEDGEMENTS

I would love to thank my PhD advisor, Prof. Gert Goch, for his support, guidance, time and encouragement in my PhD study. In my first semester at UNC Charlotte, he accepted me as his PhD student and allowed me to work on the project *Error Correction of Rotary Tables under Loads* funded by the Center for Precision Metrology. The research outcomes later became the core contents of my PhD dissertation. Prof. Goch is a very knowledgeable and supportive advisor. When I have problems, results or findings, he spends adequate amount of time and efforts to discuss them with me. I am very thankful for his high standard on the quality of research work.

I thank Prof. Jimmie A. Miller. He has spent large amount of time helping me check the core processing solution, set up spindle error analyzer on rotary tables, revise journal papers, conference papers and this dissertation. His humor and encouragement help me survive the difficult periods at the theoretical research phase.

I thank Mr. Norbert Steffens of Hexagon Metrology, Germany, for providing two internships in summer 2017 and fall 2018. In the first internship, I received adequate financial support and training resources to learn Leitz CMM operation at Wetlar, Germany and University of Bremen, Germany.

I would love to thank Dr. Felix Balzer of Hexagon Metrology, Germany, for his help and leadership in the last two years. In summer 2017, he coached me in the gear measurement using Quindos. Then, he invited me to take the second internship in fall 2018 and facilitated the application process. I had great opportunities to study the performance of multiple rotary tables in Hexagon Metrology, Germany. He also played a key role in the

cooperation with Physikalisch-Technische Bundesanstalt, Germany (PTB) to investigate its heavy duty aerostatic rotary table.

I would love to thank Mr. Axel von Freyberg of Bremen Institute for Metrology, Automation and Quality Science (BIMAQ), University of Bremen, Germany. He was very supportive during my training at BIMAQ in summer 2017 and accepted my proposal to investigate the behavior of BIMAQ's hydrostatic rotary table under various loads. Since then, he helped arrange tens of experiments and sent results to me for analysis. I am very thankful for his persistence in the past two years which has yielded lots of meaningful results.

I thank Mr. Frank Horn of BIMAQ, University of Bremen, Germany, for carrying out experiments which help us understand the behaviors of BIMAQ's hydrostatic rotary table.

I thank Dr. Martin Stein and Ms. Ann-Kathrin Wiemann of Physikalisch-Technische Bundesanstalt (PTB), Germany for their great contribution to the jointed research on *Improved Gear Metrology Based on the Calibration and Compensation of Rotary Table Error Motions*. They allowed me to use the famous large gear standard in this research and helped to carry out some experiments.

I thank Prof. Christopher J. Evans, Prof. Edward P. Morse, Prof. Dr. Stuart T. Smith and Prof. M. Yasin Raja for serving on my dissertation committee. They gave me lots of valuable suggestions in solving problems and improving the quality of dissertation.

I thank Prof. Tony L. Schmitz, who kindly offered me a teaching assistant position in ECGR 2161 lab session. It helped me to survive the first year before receiving funding from the affiliated project of Center for Precision Metrology.

I would love to give special thanks to my wife. Because we were admitted to two different graduate schools, we have been living separately since the very first day in United States. In the past six years, she was very brave and talented to live alone, maintain our relationship and conquer the challenges during her PhD study in Material Science and Engineering at the University of Illinois at Urbana Champaign.

I would love to thank Mr. Jesse Groover, Ms. Yue Peng and Dr. Kang Ni for their kind help in making circular ball plate and carrying out experiments. I am also very thankful for their valuable suggestions which helped me to solve many problems in research.

I thank my dear friends at Charlotte, NC, Rolla, MO and China for the friendship, encouragement and our wonderful memory together. Special thank goes to Mr. John Orr and his family.

DEDICATION

To my wife and parents

TABLE OF CONTENTS

LIST OF FIGURES	xiii
LIST OF TABLES	xxii
NONMENCLATURE.....	xxiv
LIST OF ABBREVIATIONS.....	xxx
CHAPTER 1: INTRODUCTION AND LITERATURE REVIEW	1
1.1 Background	1
1.2. Bearing systems of rotary tables (RTs)	4
1.2.1 Rolling-element bearing	4
1.2.2 External pressurized bearing	5
1.2.3 Magnetic bearing	7
1.3 Error motions of RT	8
1.4 Performance tests of RTs	9
1.4.1 Static and dynamic characteristics of RTs.....	9
1.4.2 Acceptance tests of entire systems	9
1.5 Review of calibration methods.....	11
1.5.1 Methods of geometric error mapping	11
1.5.2 Error identification of rotary tables/axes	11
1.6 Closure theory	13
1.7 Monte Carlo simulation.....	14
1.8 Error motions of RTs under loads	14
1.9 Contribution of this research	16

1.10 Dissertation layout.....	16
1.10.1 Development of a new calibration method.....	16
1.10.2 Error motions of RTs under loads	17
CHAPTER 2: A NEW ERROR MAPPING TECHNIQUE USING A CIRCULAR BALL PLATE	18
2.1 Introduction	18
2.1.1 Calibration methods for angular positioning deviation	18
2.1.2 Calibration methods for six error motions.....	19
2.1.3 Alternative solution	21
2.2 Experimental setup and data acquisition.....	22
2.3 Mathematical model	24
2.3.1 First chain of coordinate systems (CSs)	24
2.3.2 Second chain of CSs.....	28
2.4 Data processing	35
2.4.1 Extend three-rosette method for error separation.....	35
2.4.2 Extend three-rosette method for error separation (high sample density)	39
2.4.3 A complete solution.....	42
2.4.4 Artifact calibration.....	44
CHAPTER 3: NUMERICAL SIMULATION.....	45
3.1 Simulation input	45
3.1.1 Simulation input: circular ball plate (CBP) artifact.....	45
3.1.2 Simulation input: RT	46
3.1.3 Simulation input: coordinate measuring machine (CMM).....	47

3.2. Simulation results	51
3.2.1 Error motions	51
3.2.2 CMM deviations	54
3.2.3 Artifact deviations	55
3.3 Key factors	56
3.3.1 Ball plate radius r_{s0}	57
3.3.2 Number of spheres N and number of measuring positions M	58
3.3.3 CMM's random deviations	60
3.4 CMM drift	61
3.4.1 Drift test of CMM and workpiece	61
3.4.2 Influence of CMM's drift	63
CHAPTER 4: EXPERIMENTS	65
4.1 CBP artifact	65
4.1.1 Design of a CBP artifact	65
4.1.2 Fabrication and stability test of the artifact	69
4.2 Setup of ball step gage (BSG)	72
4.3 Spindle error analyzer (SEA)	73
4.3.1 Setup of SEA	73
4.3.2 Drift test of SEA system	74
4.4 Separation of CMM deviations	79
4.4.1 BSG	79
4.4.2 CMM systematic geometric deviations determined by the BSG and the CBP	89
4.4.3 Random components of the CMM's geometric deviations	90

4.5 Error motions of RT	92
4.5.1 Calibration procedure using spindle error analyzer.....	92
4.5.2 Experimental results	93
CHAPTER 5: ROTARY TABLES UNDER SYMMETRIC LOADS.....	97
5.1 Introduction of tested rotary tables.....	97
5.1.1 Hydrostatic RT	97
5.1.2 Aerostatic RTs	98
5.2 Experimental setups	100
5.2.1 Experimental setup for the RT A.....	100
5.2.2 Experimental setup for the RT B.....	101
5.2.3 Experimental setup for the RT C.....	102
5.2.4 Reference point.....	105
5.3. Calibration procedure	106
5.3.1 Warm up procedure	106
5.3.2 CMM deviations.....	107
5.4 Experimental results	110
5.4.1 RT A	110
5.4.2 RT B	112
5.4.3 RT C	112
CHAPTER 6: ROTARY TABLE UNDER ASYMMETRIC LOADS	115
6.1 Experimental setups	115
6.1.1 Weak asymmetric loads for RT A.....	115
6.1.2 Asymmetric loads for the RT C.....	116

6.2 Experimental results	118
6.2.1 Weak asymmetric loads for RT A	118
6.2.2 Asymmetric loads for the RT C.....	119
CHAPTER 7: SUMMARY	122
CHAPTER 8: FUTURE WORK.....	124
REFERENCES	125

LIST OF FIGURES

Figure 1.1. Large-scale parts: (a) turbine blades of turbofan aircraft engine [2] (2) gas turbine for an aluminum plant [3] (c) planet gears of an offshore wind turbine [4] (d) gears in a ship gear box [5] (e) combustion chamber of an automotive engine [6] (f) automotive frame [7].....	1
Figure 1.2. Multi-axis measuring devices: (a) Leitz PMM-F 30.20.16 (b) Zeiss Prismo Navigator CMM (c) Mahr MarSurf LD 260 combined contour and surface measuring station (d) Gleason 300 GMSL gear measuring instrument [9](e) Mitutoyo roundness tester.....	2
Figure 1.3. RTs installed on multi-axis measuring devices: (a) a built-in RT on a Zeiss CMM (b) a RT on a Mahr combined contour and surface measuring station (c) a RT on a Mitutoyo roundness tester.....	3
Figure 1.4. Manually operated RTs for machine tools [10]: (a) an installed RT (b) components of a disassembled RT.....	3
Figure 1.5. Heavy-duty RTs of machine tools [12]: (a) milling RT (b) swiveling milling RT (c) turning RT (d) grinding RT.....	4
Figure 1.6. Schematic of rolling-element bearing [13]: (a) an axial-radial combined roller bearing, including two thrust needle roller bearings and a radial cylindrical roller (b) a RT contains a roller bearing system.....	5
Figure 1.7. Large-scale RTs with external pressurized bearings: (a) Zollern ZHRT 1000.0340.0550 hydrostatic RT (b) Zollern ZART 1200.0390.0 aerostatic RT.	6

Figure 1.8. Magnetic bearing: (a) Schematic of magnetic bearing [17] (b) Schematic of basic operation [16].....	8
Figure 1.9. Error motions of a rotary table: (a) schematic design (b) six error motions of RT, including three translational terms δx , δy and δz , two tilt terms ϵx and ϵy , and one angular positioning deviation ϵz	8
Figure 1.10. Schematic of a test rig for measuring the static and dynamic characteristics of RT [15].....	9
Figure 1.11. WES gear loaded on a hydrostatic rotary table at the Bremen Institute for Metrology, Automation and Quality Science (BIMAQ), University of Bremen, Germany.	15
Figure 2.1. Schematic of three measurement setups to calibrate the angular positioning deviation ϵz	18
Figure 2.2. Schematic of six error motions of a rotary table.	20
Figure 2.3. Schematic of spindle error analyzer setup on the rotary table.....	20
Figure 2.4. Schematic of measurement setup for calibration of RT.	22
Figure 2.5. Schematic of the preparation and measurement procedure for rotary table calibration.	23
Figure 2.6. Position deviations of the j^{th} sphere in the ACS.....	25
Figure 2.7. Schematic of the artifact's eccentricity and tilt deviations.....	26
Figure 2.8. Path of probe in RT calibration: (a) the path of probe at measuring all spheres at a rotary position (b) the path of the probe through the experiment was enclosed by a narrow band.	28

Figure 2.9. Schematic of the $M \times N$ sphere centers after one complete rotation of the ball plate.....	29
Figure 2.10. Developed mathematical vector model illustrating the chain of coordinate systems from the frame CS (CMM) to the sphere center.	32
Figure 2.11. Rosette table ($N = 3$ and $M = 3N$) and its subtables for the angular direction, where the diagonals related to the measuring position k ($k = 1, 2, \dots, 9$) are marked with different colors.....	42
Figure 2.12. The complete error processing procedure.	43
Figure 3.1. Example of simulation input for a translational term.....	47
Figure 3.2. Probing strategy: (a) Spherical coordinate system (b) point distribution of 5-point probing strategy (c) point distribution of 15-point probing strategy.	48
Figure 3.3. Simulation inputs and outputs of the RT error motions (periods = 2π): (a) δx (b) δy (c) δz (d) ϵx (e) ϵy (f) ϵz	52
Figure 3.4. Simulation inputs and outputs of the δx deviation whose period did not equal to 2π : (a) 1.56π (b) 2.72π (c) 4.18π	53
Figure 3.5. Frequency components of input and output δx deviation with number of cycle 4 and cycle period: (a) $Ts = 2\pi$ (b) $Ts = 2.72\pi$	54
Figure 3.6. Inputs and outputs of CMM's systematic geometric deviations.	55
Figure 3.7. Simulation inputs and outputs of the spheres' position deviations.	56
Figure 3.8. μE_{max} and $\mu E_{max} \pm 3\sigma E_{max}$ ranges between the sampled input and output values, when the rs_0 increased from 50 mm to 400 mm: (a) δx (b) δy (c) δz (d) ϵx (e) ϵy (f) ϵz	58

Figure 3.9. μE_{max} and $\mu E_{max} \pm 3\sigma E_{max}$ ranges of between the sampled input and output values, when N was increased from 6 to 48: (a) δx (b) δy (c) δz (d) ϵx (e) ϵy (f) ϵz	59
Figure 3.10. μE_{max} and $\mu E_{max} \pm 3\sigma E_{max}$ ranges of between the sampled input and output values, when σgr was increased from 0.02 to 0.2: (a) δx (b) δy (c) δz (d) ϵx (e) ϵy (f) ϵz	61
Figure 3.11. Deviations of sphere centers along three axes in 20-hour drift: (a) x deviations (b) y deviations (c) z deviations.	62
Figure 3.12. μE_{max} and $\mu E_{max} \pm 3\sigma E_{max}$ ranges between the sampled input and output values, when the amplification factor of CMM drift increased from 0.5 to 3: (a) δx (b) δy (c) δz (d) ϵx (e) ϵy (f) ϵz	64
Figure 4.1. A CBP artifact made by Hexagon Manufacturing Intelligence, Germany.....	65
Figure 4.2. Schematic of double plate artifact.	66
Figure 4.3. Least deformation of top plate.....	67
Figure 4.4. Fixing a sphere on the base plate: (a) schematic of circular contact line between the sphere and countersink (b) epoxy glue applied between the sphere and the surface of countersink.	67
Figure 4.5. Illustration of assembly details: (a) fixturing a precision sphere on the countersink (b) Maxwell kinematic coupling between two plates.	68
Figure 4.6. Upper plate clamped on the RT for stability test.....	69
Figure 4.7. Monitored position variation of spheres after assembly: (a) relative z coordinates of spheres from the 52th hour to 68.8th hour (b) schematic of z coordinate variations of spheres between the 52th hour and 68.8th hour.	70

Figure 4.8. Assembled artifact: (a) lower plate fixed on the RT (b) entire artifact.	70
Figure 4.9. Position changes of spheres from the 74th hour to the 158th hour: (a) z coordinates (b) x coordinates (c) y coordinates (the sudden change of sphere coordinates at the 116th hour resulted from the interruption of experiment).	71
Figure 4.10. Setup of BSG on the RT: (a) structure and kinematic coupling (b) detailed view of the triangular beams supporting the spheres (c) schematic of location and alignment of BSG at the initial rotary position (0°).....	72
Figure 4.11. Setup of spindle error analyzer on a Zollern ZART 1200.0390.0 aerostatic rotary table: (a) illustration of an in-house made metrology frame, which fixed the sensor holder over the rotary table (b) fixture of SEA system on rotary table.	73
Figure 4.12. 18-hour drift test of SEA system: (a) temperature data of six sensors attached on an angle iron (b) ambient temperature near ball target (c) displacements data of five capacitive sensors (d) displacements and temperatures from the 11th hour to 12th hour.	76
Figure 4.13. Displacements of a master sphere, fixed at the center of RT, and repeatedly probed at a point in -x and -z directions, respectively: (a) displacement along x-axis (b) displacement along z-axis.	78
Figure 4.14. Sample inlet air pressure of the entire system.	78
Figure 4.15. Schematic of sphere positions in the test.....	79
Figure 4.16. Influence of each error motion to the coordinates of two spheres (small-angle approximation was applied: e.g., $\sin \epsilon x \approx \epsilon x$ and $\cos \epsilon x \approx 1 - \epsilon x^2$).	80
Figure 4.17. Probing strategy for a sphere on the BSG: (a) locations of probing points (b) orientation of probing points at rotary position of 0° and 90° (top view).	82

Figure 4.18. Schematic of probing error detection: (a) Probing direction for the same point on a probed sphere at various rotary position (b) Probing error calculation of an arbitrary measurement for the #8 point (c) Detected probing error at the eight sampled directions using the #8 point.....	83
Figure 4.19. Separated probing errors at 10 probing points on the #4 and #6 spheres when the table was rotated by 10 cycles in steps of 7.5°	84
Figure 4.20. Detected probing errors using different probing points, after removing the phase shifts due to different initial position.....	85
Figure 4.21. Deviations of sphere coordinates resulting from the probing system: (a), (d), (g) probing deviations at measuring the #6 sphere (b), (e), (h) probing deviations at measuring the #4 sphere (c), (f), (i) overall influence of the probing system on the relative coordinates of the #6 sphere.	86
Figure 4.22. Separated systematic components of the CMM's geometric deviations at 48 measuring positions by comparing the coordinates of the #4 and #6 spheres in 10 cycles: (a), (d), (g) deviations of the #6 sphere in three directions from its average path in each cycle (b), (e), (h) deviations of the #4 sphere in three directions from its average path in each cycle (c), (f), (i) separated CMM geometric deviations.	87
Figure 4.23. Separated systematic components of the CMM's geometric deviations by comparing the coordinates of the #4 and #5 spheres in 10 cycles: (a) radial deviations (b) tangential deviations (c) z deviations.....	88
Figure 4.24. Separated systematic components of the CMM's geometric deviations at 48 measuring positions, where the ideal paths was reduced by a factor of 0.00001: (a) polar plot (top view) (b) 3D plot.....	88

Figure 4.25. Systematic components of geometric deviations of the CMM at the 48 measuring positions: (a) x deviations (b) y deviations (c) z deviations.....	89
Figure 4.26. Standard deviations of the radial, tangential and z components of ΔPgr from the reference point (#4 sphere) to 48 measuring positions, by measuring the relative coordinates of the #2 sphere to the #4 sphere, as well as the #6 sphere to the #4 sphere: (a) radial deviations (b) tangential deviations (c) z deviations.	91
Figure 4.27. Standard deviations of the radial, tangential and z components of ΔPgr from the reference point (#4 sphere) to 48 measuring positions. by measuring the relative coordinates of the #3 sphere to the #4 sphere, as well as the #5 sphere to the #4 sphere: (a) radial deviations (b) tangential deviations (c) z deviations.	92
Figure 4.28. Error motions of the RT separated by the SEA T1 (blue curve), SEA T2 (black curve) and the CBP (red curve): (a) δx (b) ϵy	93
Figure 4.29. Error motions of the RT separated by the SEA T1 (blue curve), SEA T2 (black curve) and the CBP (red curve): (a) δy (b) δz (c) ϵx	94
Figure 4.30. RT at UNC Charlotte: (a) orientation of the RT in the measuring system (b) schematic of driving train (bottom view).....	95
Figure 4.31. Separated δx and ϵy of the RT by the CBP test.....	96
Figure 5.1. Loading procedure of a heavy gear onto hydrostatic RT: (a) preparation and placement of a helical gear on a measuring palette using traveling overhead crane (b) transportation of the measuring palette from loading gate to RT, with three hemisphere components for kinematic coupling (c) loading the measuring palette on RT.	98
Figure 5.2. Configuration of 4-axis CMM at PTB.....	99

Figure 5.3. Configuration of 4-axis CMM at UNC Charlotte: (a) Leitz PMM-F 30.20.16 (b) Zollern ZART 1200.0390.0 aerostatic RT.	99
Figure 5.4. Experimental setup for RT under symmetric loads: (a) case 1: non-load (b) case 3: measuring palette and a helical ring gear (c) case 5: palette, a helical ring gear and 8 spur gears as additional load.	100
Figure 5.5. Schematic of clamping method for the artifact on measuring palette.	101
Figure 5.6. Schematic of clamping method for artifact on top of helical gear.	101
Figure 5.7. Experimental setups to identify the error motions of RT under symmetric loads: (a) no load (b) 1 ton (c) 2 tons (d) the CBP fixed on top of steel disk in (b) and (c) with help of toe clamps and steel plates.	102
Figure 5.8. Distribution of loads on the RT C at UNC Charlotte: (a), (d) 224.6 kg symmetric load (b), (e) 489.2 kg symmetric load (c), (f) 666.2 kg symmetric load.	103
Figure 5.9. Illustration of three artifact positions in the experiments, with a reference point defined as the center of approximated workpiece coordinate system at the #3 position.	105
Figure 5.10. Measured z coordinates of six sphere centers in four cycles in non-load case. No warm-up routine was executed.	106
Figure 5.11. Original and adjusted geometric deviations of CMM B at 48 measuring positions at three heights: (a) x deviations (b) y deviation (c) z deviations.	107
Figure 5.12. Amplitudes of polynomial components for CMM B's geometric deviations at three heights: (a) x deviations (b) y deviations (c) z deviations.	109
Figure 5.13. Amplitudes of polynomial components for CMM A's geometric deviations in five cases: (a) x deviations (b) y deviations (c) z deviations.	109

Figure 5.14 Original and adjusted geometric deviations of CMM A at 48 measuring positions in five cases: (a) x deviations (b) y deviation (c) z deviations.	110
Figure 5.15. Separated error motions of a hydrostatic RT under symmetric loads from no load to 3.45 ton: (a) δx (b) δy (c) δz (d) ϵx (e) ϵy (f) ϵz	111
Figure 5.16. Six error motions of the rotary table B under three levels of symmetric loads: (a) δx (b) δy (c) δz (d) ϵx (e) ϵy (f) ϵz	112
Figure 5.17. Separated δx , δy and δz of the rotary table C under four levels of symmetric loads.	113
Figure 5.18. Separated ϵx , ϵy and ϵz of the RT C under four levels of symmetric loads.	114
Figure 6.1. Experimental setup for RT under weak asymmetric loads: (a) loading the ring gear onto the linear motion guides; (b) three linear motion guides and accessories; (c) preset the positions of three blocks and three short pins to constraint the position of the gear.	115
Figure 6.2. Asymmetric loading cases for the RT C: (a) case 1 (reference case, symmetric load) (b) case 2 (c) case 3 (d) case 4 (e) case 5 (f) case 6.	116
Figure 6.3. Asymmetric loading cases: (a) x and y coordinates of the gravity centers (b) load values (c) normalized torques.	117
Figure 6.4. Separated error motions of a hydrostatic RT under seven asymmetric 1.7 tons loads: (a) δx (b) δy (c) δz (d) ϵx (e) ϵy (f) ϵz	119
Figure 6.5. Separated δx , δy and δz of the RT C under asymmetric loads.	120
Figure 6.6. Separated ϵx , ϵy and ϵz of the RT C under asymmetric loads.	121

LIST OF TABLES

Table 2.1. Nomenclature (vector model).....	31
Table 2.2. Nomenclature (AWCS).....	34
Table 2.3. Rosette table for the angular direction ($M = N = 3$).....	36
Table 2.4. Rosette table for the radial direction ($M = N = 3$).....	37
Table 2.5. Rosette table for the axial direction ($M = N = 3$).....	38
Table 2.6. Rosette table for the angular direction ($N = 3$ and $M = 3N$).....	40
Table 2.7. Rosette table for the radial direction ($N = 3$ and $M = 3N$).....	40
Table 2.8. Rosette table for the axial direction ($N = 3$ and $M = 3N$).....	41
Table 3.1. Parameter setting for the artifact.....	46
Table 3.2. Parameter setting for the RT error motions.....	47
Table 3.3. Probing deviations for 5-point probing strategy. (Leitz PMM-F, 80 mm length reference probe, 5 mm probe tip diameter).....	49
Table 3.4. Probing deviations for 15-point probing strategy. (Leitz PMM-C, 80 mm reference probe, 5 mm probe tip diameter, severe drift of the sphere center observed ($x = 1 \mu\text{m}$, $y = 1.5 \mu\text{m}$ and $z = 0.6 \mu\text{m}$)).....	49
Table 3.5. Parameter setting for CMM deviations.....	50
Table 3.6. Simulated deviations of the ball plate artefact.....	56
Table 4.1. Influence of each error motion to the measured relative position of the off-centered #6 sphere to the centered #4 sphere.....	81

Table 5.1. Mass and position deviations of steel slugs (symmetric loads). The coordinates of the #6, #7 and #8 slugs in load case #4 were different from the ones in the load cases #2 and #3 (see Table 5.2).....	104
Table 5.2. Gravity centers of loads.	104
Table 6.1. Load value and gravity center for asymmetric loads.	117
Table 6.2. Mass and position deviations of steel slugs (asymmetric loads).	118

NONMENCLATURE

$E_{L,MPE}$	maximum permissible error for length measurement
$F_{input,sys}$	simulated polynomial functions for the systematic components of the error motions
$F_{\Delta x_{gs}}$	trigonometric polynomial function for the x components of CMM's systematic geometric deviations at measuring positions.
$[H]_{RT}$	coordinates of artifact center in the Rotary table CS
H_x	x coordinate of artifact center
H_y	y coordinate of artifact center
H_z	z coordinate of artifact center
H_c	height difference between the center of circular ball plate artifact and the reference z coordinate
$L_{r(i,j)}$	distance of the (i^{th}, j^{th}) sphere to the center of a sphere approximated to $M \times N$ measured spheres
M	number of evenly spaced rotary positions in one cycle of rotary table
M_1	lowest frequency component of a polynomial function
M_2	highest frequency component of a polynomial function
N	number of spheres of circular ball plate artifact
$P_{m(i,j)}$	measured coordinates of the (i^{th}, j^{th}) sphere center
$R_{0,MPL}$	repeatability range of length measurement
$R_{A,RT}$	rotation matrix from the artifact CS to the rotary table CS
$R_{RT,F}$	rotation matrix from the rotary table CS to the frame CS

$R_{RT,AW}$	rotation matrix from the rotary table CS to the aligned workpiece CS
S	actual coordinates of a sphere in the circular ball plate CS
T	coordinates of origin O_C in the FCS
T_s	defined period of simulated polynomial functions for the systematic components of the error motions
$T_{s(m)}$	defined period of the m^{th} frequency component of simulated polynomial functions for the systematic components of the error motions
X	X-axis of a Cartesian coordinate system
Y	Y-axis of a Cartesian coordinate system
Z	Z-axis of a Cartesian coordinate system
$a_{m.c}$	coefficient of the m^{th} cosine term of a trigonometric polynomial
$a_{m.s}$	coefficient of the m^{th} sine term of a trigonometric polynomial
i	i^{th} rotary position of rotary table
j	j^{th} sphere on the circular ball plate artifact
k	k^{th} measuring position defined for the CMM
q	q^{th} probing point on the sphere
r_H	radial position of the center of artifact in the rotary table CS
r_{s0}	average radial position of spheres
t	t^{th} cycle of the rotary table
$w_{m.c}$	weighting factor of the m^{th} cosine term of a trigonometric polynomial
$w_{m.s}$	weighting factor of the m^{th} sine term of a trigonometric polynomial
$x_{m(i,j)}$	x coordinate of the $(i^{\text{th}}, j^{\text{th}})$ measured sphere center
x_{wo}	x coordinate of the center of a sphere approximated to $M \times N$ measured

	spheres
$y_{m(i,j)}$	y coordinate of the $(i^{\text{th}}, j^{\text{th}})$ measured sphere center
y_{wo}	y coordinate of the center of a sphere approximated to $M \times N$ measured spheres
$z_{m(i,j)}$	z coordinate of the $(i^{\text{th}}, j^{\text{th}})$ measured sphere center
z_{wo}	z coordinate of the center of a sphere approximated to $M \times N$ measured spheres
r_{wo}	radius of a sphere approximated to $M \times N$ measured spheres
ΔC	translational error motions of rotary table
ΔP_{gr}	random components of 21 parametric deviations
ΔP_{gs}	systematic components of 21 parametric deviations
$\Delta P_{m(i,j)}$	deviations of the $(i^{\text{th}}, j^{\text{th}})$ sphere center relative to its nominal position
ΔP_{pr}	random components of probing error
ΔP_{ps}	systematic components of probing error
$\Delta r_{ct(i,j)}$	radial error motion of the rotary table for the $(i^{\text{th}}, j^{\text{th}})$ measurement resulted from the δ_x and δ_y
Δr_s	radial deviation of a sphere on the circular ball plate
$\Delta r_{m(i,j)}$	radial deviation of the $(i^{\text{th}}, j^{\text{th}})$ sphere center relative to its nominal position
Δx_{gr}	random component of 21 parametric deviations along the X-axis
Δx_{gs}	systematic component of 21 parametric deviations along the X-axis

Δx_{pr}	random components of probing error along the X-axis
Δx_{ps}	systematic component of probing error along the X-axis
Δy_{gr}	random component of 21 parametric deviations along the Y-axis
Δy_{gs}	systematic component of 21 parametric deviations along the Y-axis
Δy_{pr}	random components of probing error along the Y-axis
Δy_{ps}	systematic component of probing error along the Y-axis
Δz_{gr}	random component of 21 parametric deviations along the Z-axis
Δz_{gs}	systematic component of 21 parametric deviations along the Z-axis
$\Delta z_{m(i,j)}$	axial deviation of the (i^{th}, j^{th}) sphere center relative to its nominal position
Δz_s	axial deviation of a sphere
Δz_{ps}	systematic component of probing error along the Z-axis
Δz_{pr}	random component of probing error along the Z-axis
$\Delta \varphi$	angular deviation of a sphere on the circular ball plate
$\Delta \tau_{m(i,j)}$	tangential deviation of the (i^{th}, j^{th}) sphere center relative to its nominal position
$\Delta \theta_{ct(i,j)}$	angular error motion of the rotary table for the (i^{th}, j^{th}) measurement resulted from the δ_x and δ_y
α	azimuthal angle in the XY plane from the x-axis in a spherical CS
β	polar angle from the positive z-axis in a spherical CS
φ_H	angle of the center of artifact in the rotary table CS
φ_0	nominal angular position of a sphere center

θ_0	nominal rotary angle
θ	actual rotary angle
δ_x	translational error motion of rotary table along the X-axis
δ_{xs}	systematic component of translational error motion along the X-axis
δ_{xr}	random component of translational error motion along the X-axis
δ_y	translational error motion of rotary table along the Y-axis
δ_{ys}	systematic component of translational error motion along the Y-axis
δ_{yr}	random component of translational error motion along the Y-axis
δ_z	translational error motion of rotary table along the Z-axis
δ_{zs}	systematic component of translational error motion along the Z-axis
δ_{zr}	random component of translational error motion along the Z-axis
ε_{Ax}	tilt deviation of artifact about the X-axis
ε_{Ay}	tilt deviation of artifact about the Y-axis
ε_x	tilt error motion of rotary table around the X-axis
ε_{xr}	random component of tilt error motion around the X-axis
ε_{xs}	systematic component of tilt error motion around the X-axis
ε_y	tilt error motion around the Y-axis
ε_{yr}	random component of tilt error motion around the Y-axis
ε_{ys}	systematic component of tilt error motion around the Y-axis
ε_y	tilt error motion of rotary table around the Y-axis
ε_{yr}	random component of tilt error motion around the Y-axis
ε_{ys}	systematic component of tilt error motion around the Y-axis

ε_z	angular positioning deviation of rotary table
ε_{zr}	random component of angular positioning deviation
ε_{zs}	systematic component of angular positioning deviation
μ	mean value in multiple measurement
$\mu_{ E_{\max} }$	mean value in multiple tests of the maximum deviation between measure signal and actual signal
$\mu_{ E_{\max} , \delta_x}$	mean value in multiple tests of the maximum deviation between measure δ_x and actual δ_x
$\mu_{ E_{\max} , \delta_y}$	mean value in multiple tests of the maximum deviation between measure δ_y and actual δ_y
$\mu_{ E_{\max} , \delta_z}$	mean value in multiple tests of the maximum deviation between measure δ_z and actual δ_z
σ	standard deviation
$\sigma_{ E_{\max} }$	standard deviation in multiple tests of the maximum deviations between actual signal and ideal signal
ξ	angular position of a gravity center respect to the +x direction of the frame CS.

LIST OF ABBREVIATIONS

3D	Three dimension
ACS	Artifact CS
AIST	Japan National Institute of Advanced Industrial Science and Technology
AWCS	Aligned workpiece CS
BIMAQ	Bremen Institute for Metrology, Automation and Quality Science
BSG	Ball step gage
CBP	Circular ball plate
CCW	Counter-clock-wise
CNC	Computer numerical control
CMM	Coordinate measuring machine
CTE	Coefficient of thermal expansion
CS	Coordinate system
CW	Clock-wise
CYL	Cylindrical
DAQ	Data acquisition
FCS	Frame coordinate system
GMI	Gear Measuring Instrument
HMI	Hexagon Manufacturing Intelligence
ISO	International Organization for Standardization
LSM	Large scale metrology
LVDT	Linear variable differential transformer

MPE	Maximum permissible error
MPL	Maximum permissible limit
NIST	National Institute of Standards and Technology
NMIJ	National Metrology Institute of Japan
PDF	Probability density function
PDGEPs	Position-dependent geometric error parameters
PIGEPs	Position-independent geometric error parameters
PTB	Physikalisch-Technische Bundesanstalt
RCS	Rotary table CS
RT	Rotary table
SEA	Spindle error analyzer
TMBB	Telescoping magnetic ball bar
ACS	Artifact coordinate system

CHAPTER 1: INTRODUCTION AND LITERATURE REVIEW

1.1 Background

Geometric inspections of large-scale parts, at affordable costs and within reasonable measuring time, are necessary in manufacturing industries. For example, to improve their reliability and safety over the lifetime of 20 years, wind energy system (WES) manufacturers need to inspect a variety of WES components, such as main bearings, gear boxes, pitch bearings and pitch drives. Figure 1.1 shows some large-scale workpieces in aerospace, wind energy, ship and automotive industries.

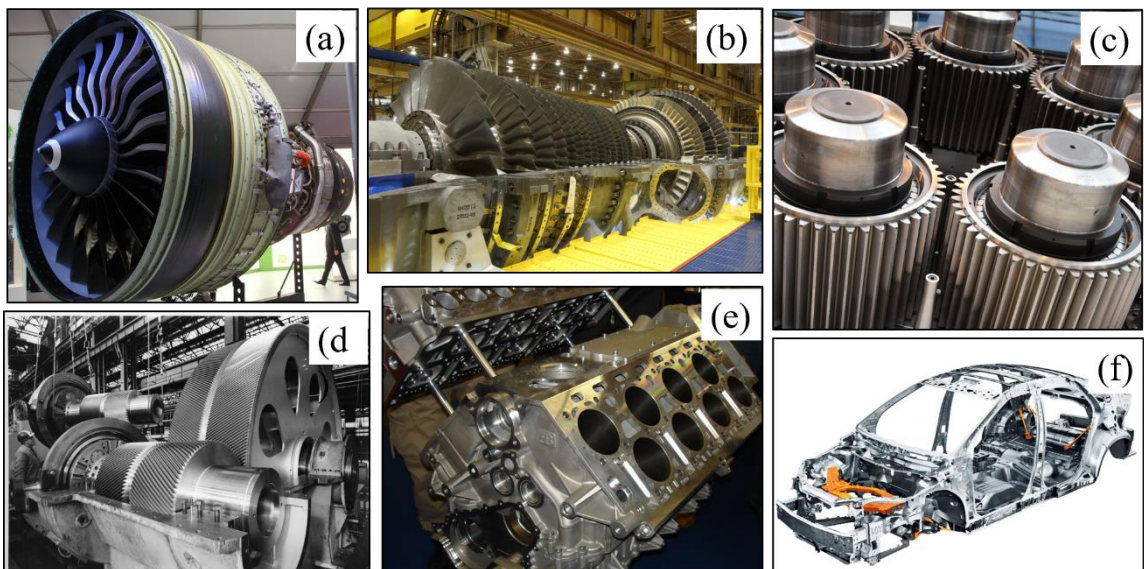


Figure 1.1. Large-scale parts: (a) turbine blades of turbofan aircraft engine [2] (2) gas turbine for an aluminum plant [3] (c) planet gears of an offshore wind turbine [4] (d) gears in a ship gear box [5] (e) combustion chamber of an automotive engine [6] (f) automotive frame [7].

4-axis measuring devices including coordinate measuring machines (CMMs), gear measuring instruments (GMI), form testers, etc. are versatile instruments for these

applications (Figure 1.2). CMMs are particularly well suited to applications, where low measurement uncertainties are required or when the features to be measured are difficult to access [8].

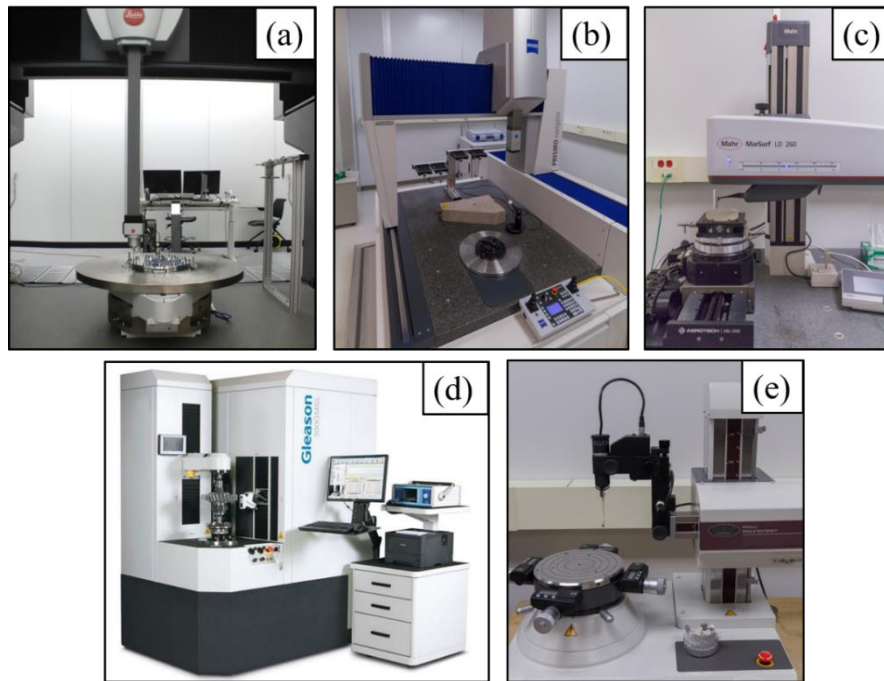


Figure 1.2. Multi-axis measuring devices: (a) Leitz PMM-F 30.20.16 (b) Zeiss Prismo Navigator CMM (c) Mahr MarSurf LD 260 combined contour and surface measuring station (d) Gleason 300 GMSL gear measuring instrument [9](e) Mitutoyo roundness tester.

As key components of multi-axis measuring devices, rotary tables (RTs) provide a quick rotary positioning of components to assess measurands (Figure 1.3). Before computer numerical control (CNC) systems were widely introduced to industrial production, only manually operated RTs were available for measuring devices and machine tools. Figure 1.4(a) shows a 10" manual RT [10] and Figure 1.4(b) shows components of a disassembled table [11]. Nowadays, computer-controlled RTs effectively improve the throughput of manufacturing process and measuring tasks. Moreover, many heavy-duty,

high precision and fully automated RTs have been developed for the manufacturing of large-scale parts (Figure 1.5) [12].

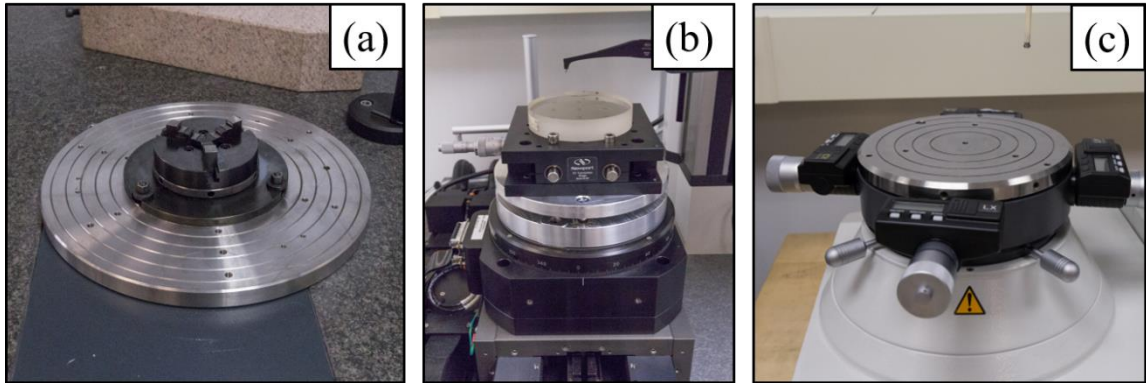


Figure 1.3. RTs installed on multi-axis measuring devices: (a) a built-in RT on a Zeiss CMM (b) a RT on a Mahr combined contour and surface measuring station (c) a RT on a Mitutoyo roundness tester.

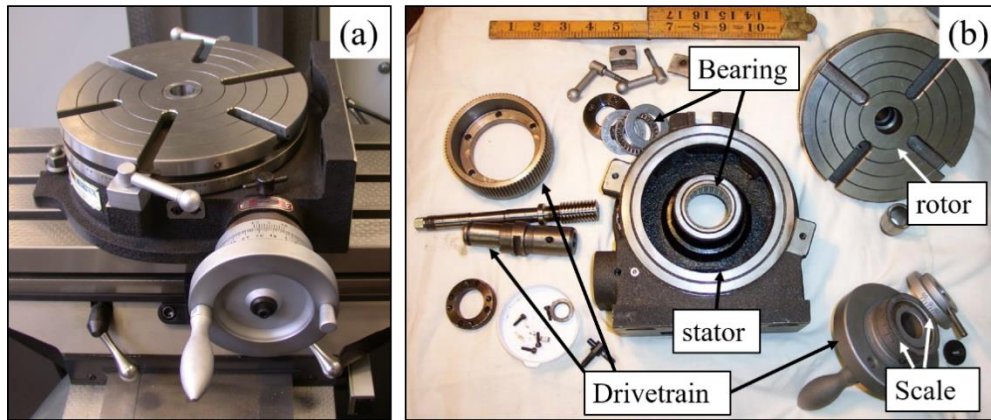


Figure 1.4. Manually operated RTs for machine tools [10]: (a) an installed RT (b) components of a disassembled RT.

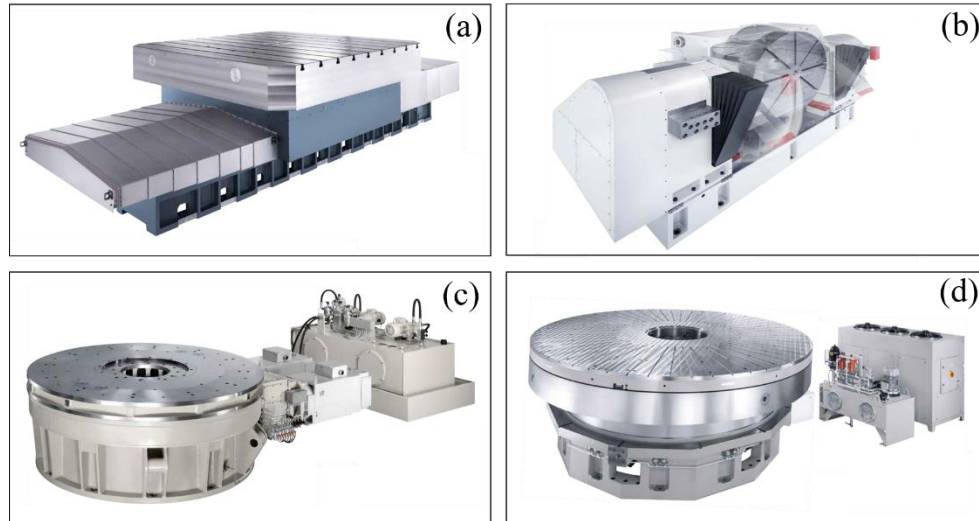


Figure 1.5. Heavy-duty RTs of machine tools [12]: (a) milling RT (b) swiveling milling RT (c) turning RT (d) grinding RT.

1.2. Bearing systems of rotary tables (RTs)

As shown in Figure 1.4(b), a RT consists of rotor, stator, hand wheel, worm drive, scale, bearings and accessories. Bearing systems reduce the friction between rotor and stator so that smooth rotary motion can be achieved. Three types of bearings are used for RTs: rolling-element bearings, external pressurized bearings and magnetic bearings.

1.2.1 Rolling-element bearing

A rolling-element bearing has rolling elements arranged between the rotating and stationary races. There are many types of rolling elements including spherical rollers, cylindrical rollers, tapered rollers, barrel rollers and needle rollers. Figure 1.6 shows a common axial-radial combined roller bearing, including two thrust needle roller bearings and a radial cylindrical roller, to support axial and radial loads [13]. The table's positioning accuracy is affected by form deviations of the rolling elements, geometric accuracy of

races, assembly accuracy and so on. Moreover, the long-term wear of rolling elements under loads might degrade the accuracy of the bearing system as well.

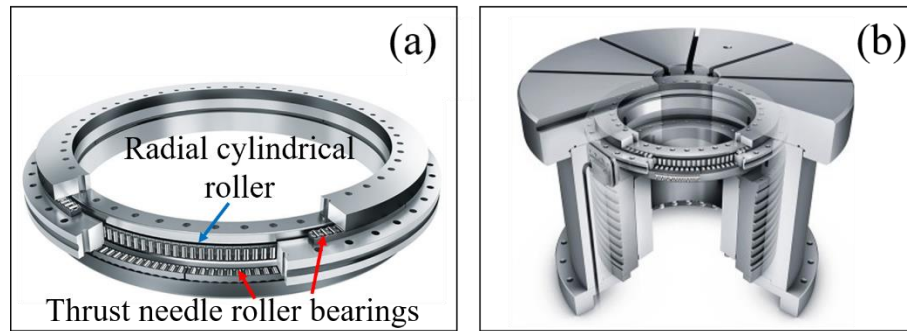


Figure 1.6. Schematic of rolling-element bearing [13]: (a) an axial-radial combined roller bearing, including two thrust needle roller bearings and a radial cylindrical roller (b) a RT contains a roller bearing system.

1.2.2 External pressurized bearing

In external pressurized bearings, the surfaces of rotor and stator are separated by a thin film of fluid, forced between the surfaces under pressure, which is generated by an external pump. A complete lubricant film is maintained whenever the bearing is pressurized, even at zero speed [14]. External pressurized bearings are widely applied in large machines, which require low friction and high load support to achieve high positioning accuracy. They are also the dominant solution for precision machines, which require high motion precision, high load capacity and high stiffness. External pressurized bearing can be further classified into two subgroups: aerostatic bearing and hydrostatic bearing. The former employs pressurized air or gas as lubricating fluid, while the latter is based on liquid fluids. Figure 1.7 shows two large-scale RTs with hydrostatic and aerostatic bearings, respectively.

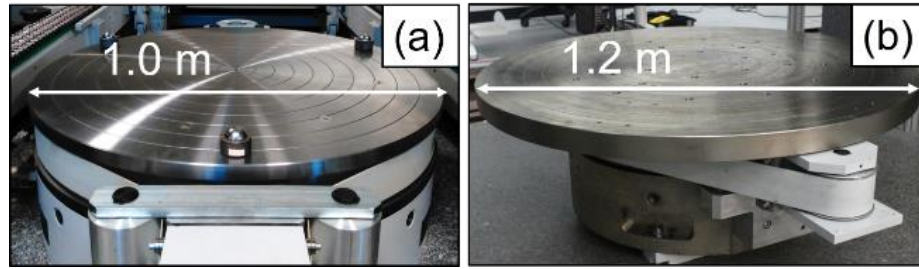


Figure 1.7. Large-scale RTs with external pressurized bearings: (a) Zollern ZHRT 1000.0340.0550 hydrostatic RT (b) Zollern ZART 1200.0390.0 aerostatic RT.

Hydrostatic bearings have two advantages over aerostatic bearings: (1) For the same mechanical structure, hydrostatic bearings have a higher maximum load compared to aerostatic bearings under same supply pressure. The lower maximum load of aerostatic bearings results from the smaller and shallower recesses, which have two purposes: (i) maintain necessary respond time between the application or change of load and the required change in recess pressure; (ii) overcome the occurrence of self-excited vibrations called “pneumatic hammering” [14]. (2) Hydrostatic bearings show a higher stiffness.

On the other hand, aerostatic bearings also have two main advantages over hydrostatic bearing: (1) lower cost: Aerostatic RT may use the centralized air supply available at production plants, while hydrostatic bearings require an independent high-pressure fluid supply system. (2) Thermal control of aerostatic RT is easier: Less heat is generated from friction forces in aerostatic bearings than hydrostatic bearings. Moreover, the high-speed air flow in aerostatic bearings effectively carries heat from the bearing to the environment. In comparison, a hydrostatic bearing needs an additional cooling system to remove the heat from the closed system.

For RTs in metrology systems, the static characteristics of external pressurized bearing films, such as load carrying capacity and mean bearing pressure, are the major consideration over dynamic characteristics.

For RTs in machine tools, dynamic characteristics become the main consideration. The concept of active compensation is introduced to enhance the dynamic characteristics of external pressurized bearing films. The system comprises one or a combination of active elements, including support and conicity piezo actuators, and supply pressure controllers [15]. These elements actuate the gap geometry or supply pressure to affect dynamic bearing forces as needed.

1.2.3 Magnetic bearing

Magnetic bearings support loads using magnetic levitation (Figure 1.8). For instance, they can levitate a rotating shaft and permit relative motion with very low friction and no mechanical wear. Magnetic bearings support the highest speeds of all kinds of bearing and have no maximum relative speed [16].

Active magnetic bearings have been successfully applied to turbomachinery and precision scanning [18]. The former one has requirements on high speed but less on accuracy and stiffness, while the main goal of the latter one is to achieve high precision. However, magnetic bearings are not suitable for machine tool applications which require high stiffness. To solve this issue, Lu et al [18] proposed a new spindle concept, where the rotor's axial position was controlled by a novel large-stroke magnetic bearing and the spindle rotor's radial position was maintained by externally pressurized fluid bearings.

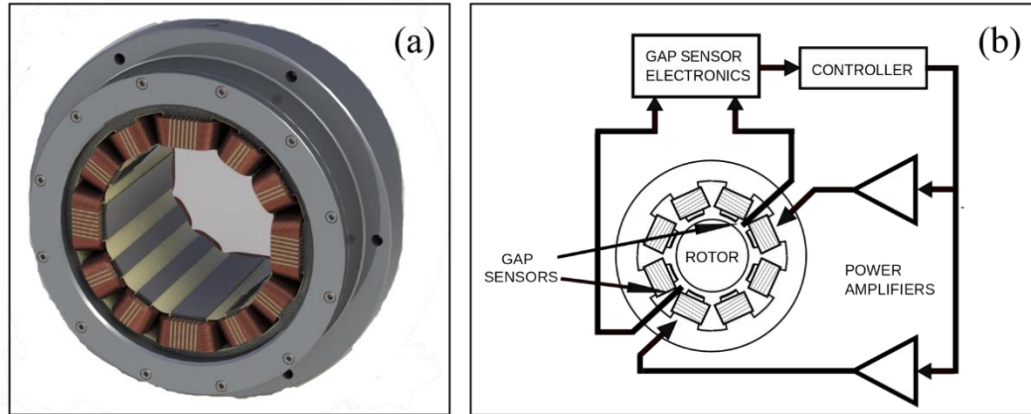


Figure 1.8. Magnetic bearing: (a) Schematic of magnetic bearing [17] (b) Schematic of basic operation [16].

1.3 Error motions of RT

Although the performances of RTs have been improved by numerous efforts in design and production, there still exist non-trivial error motions, originating from the drive train, bearings, rotary encoder, etc (Figure 1.9(a)). A rotary table/axis has three translational errors motions (δ_x , δ_y and δ_z) and three rotational error motions (ϵ_x , ϵ_y and ϵ_z) (Figure 1.9(b)). In many cases, rotary table/axes are also the dominant sources of the quasi-static and dynamic errors, due to the magnification of angular positioning errors [19].

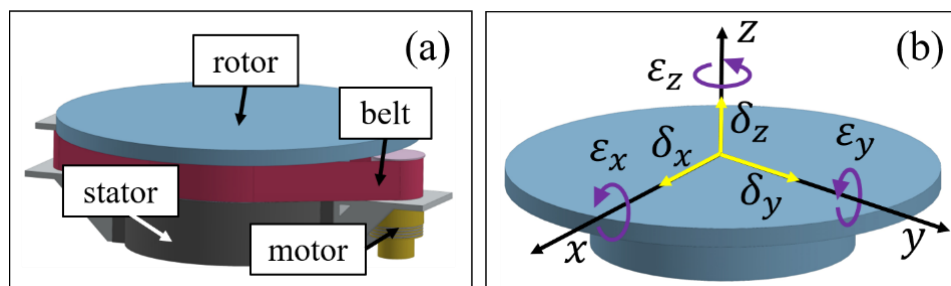


Figure 1.9. Error motions of a rotary table: (a) schematic design (b) six error motions of RT, including three translational terms δ_x , δ_y and δ_z , two tilt terms ϵ_x and ϵ_y , and one angular positioning deviation ϵ_z .

1.4 Performance tests of RTs

1.4.1 Static and dynamic characteristics of RTs

Figure 1.10 shows the schematic of a test rig for measuring the dynamic stiffness of RT [15]. The electromagnetic exciter (shaker) has an axially moveable pin, which has steel balls on both ends to act as point joints. Three non-contacting displacement sensors measure the movement of the platen, which is placed on the bearing pad and loaded by the exciter. Stiffness of the dynamometric table is several orders higher than the bearing film. There are four main sources of error in this type of experiment: bearing geometry, gap height and pressure in the air-pot, supply pressure, measurement equipment [15].

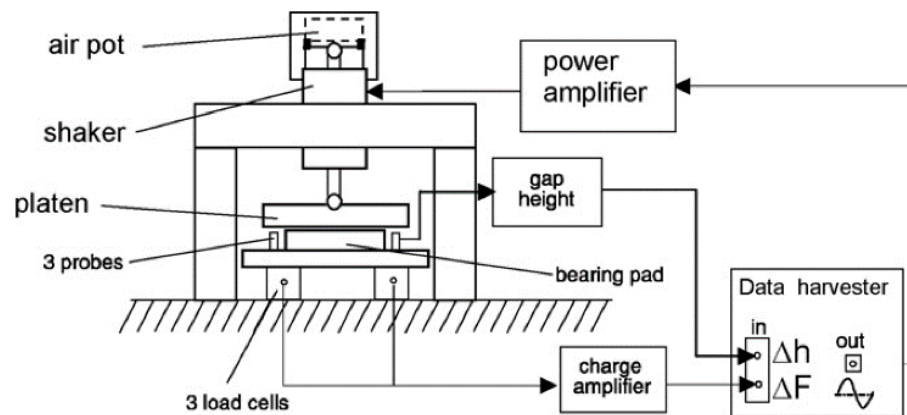


Figure 1.10. Schematic of a test rig for measuring the static and dynamic characteristics of RT [15].

1.4.2 Acceptance tests of entire systems

After the installation of rotary tables/axes on measuring devices or machine tools, acceptance tests are carried out.

Acceptance tests and reverification tests of the 4-axis CMMs are standardized by the International Organization for Standardization (ISO) [20]. Two spheres are mounted at

the outer radius of the table and located diametrically opposite to each other. One sphere is close to the table surface, while the other one is above the table. By measuring the spheres at 14 rotary positions, the deviations are measured and compared to the three maximum permissible four-axis errors MPE_{FR} , MPE_{FT} and MPE_{FA} in the radial, tangential and axial directions, respectively.

Three types of configurations can be used in performance tests or periodic maintenances of four-axis and five-axis machine tools. The first one uses the well-known telescoping magnetic ball bar (TMBB) invented by Bryan in 1982 [21][22]. Inspired by it, Lei et al [23][24] presented a probe-ball measuring device, which consisted of a 3D measuring probe, an extension bar and a plate assembly (mounted on the table). The second one is the radial test (R-test) proposed by Weikert in 2004 [25]. In the setup, a master sphere attached to the spindle is brought in contact simultaneously with three orthogonal-arranged contact-type displacement sensors which have flat tips. Commercial products are produced by IBS Precision Engineering [26] and Fidia [27]. Hong and Ibaraki [28] investigated the performance of non-contact laser displacement sensors for R-tests. Zargarbashi and Mayer [29] proposed the Cap-ball, which had a reverse configuration to the R-test. In the first two types of configurations, the components on the RT are fixed eccentrically. The spindles and RTs are moved along specified paths to gather data. In the last configuration proposed by Ibaraki et al in 2010 [30][31], a touch-trigger probe is mounted in the spindle, while three square column artifacts are fixed on the table. The locations of the three artifacts are measured at different rotary positions.

1.5 Review of calibration methods

1.5.1 Methods of geometric error mapping

Before 1980, geometric errors of CMMs and machine tools were minimized by mechanical optimization, which was time-consuming and expensive. In 1985, Zhang et al. [32] proposed computer error compensation of geometric errors and some thermal effects occurring at commercial CMM, based on a rigid body model of workpiece motion in the machine coordinate frame.

Since then, many methods have been developed for mathematical error compensation. Schwenke [33] classified the geometric error identification methods into direct and indirect measurements: Direct measurements analyze each deviation. It can be further classified into three subgroups, based on their metrological reference: the material-based methods use artefacts, such as straightedges, line scales or step gauges; the laser-based methods use the laser light's linear propagation and its wavelength as a reference; the gravity-based methods measure in reference to the gravity field of the earth. Indirect measurements imply methods focusing on superimposed errors. They require multi-axes motion of the machine under test.

1.5.2 Error identification of rotary tables/axes

The parameters influencing the positioning accuracy of 4-axis measuring devices or five-axis machine tools can be classified into two groups: the position-independent geometric error parameters (PIGEPs), which define the machine geometry; the position-dependent geometric error parameters (PDGEPs) [34]. The former group

describes the relative locations of machine's successive rotary and prismatic joints, while the latter group are motion errors.

Abbaszadeh-Mir and Mayer [34] proposed an approach and presented the simulation results for the estimation of all the eight PIGEPs from data acquired using a telescoping magnetic ball bar. Bringmann and Knapp [35] developed an error model and used nonlinear optimization methods to separate all the PIGEPs of five axes using the R-test setup. There are five out of eight PIGEPs associated with the rotary axes in 5-axis machine tools. Tsutsumi et al [36][37] used special multi-axis trajectories to estimate them, while the squareness errors of the linear axes were pre-measured using traditional methods.

In coordinate metrology, the PDGEPs (six error motions) of rotary tables/axes are dominant factors over the PIGEPs. The approaches to quantify the six error motions (PDGEPs) in a 5-axis machine tool can be classified into three groups. The first group of methods introduces external measuring devices. Conventional setup employs three LVDTs plus a sphere for the measurement of the three translational errors motions. A polygon mirror and two autocollimators are used for the calibration of the three rotational error motions [38]. Another choice is the well-known spindle error analyzer (SEA) [26][39], which can measure all the error motions except the angular positioning deviation. Schwenke et al. [40] extended the tracking interferometers used in the calibration of linear axes to the calibration of rotary axes. The second group of approaches enables the exclusive motion of the targeted one or two rotary axes, while keeping the other axes stationary to avoid contributions from the PDGEPs of the other axes. TMBB is frequently employed in the measurement setup. Multiple works are reported by Zargarbashi and Mayer (a trunnion axis) [41], Lei et al (a rotary axis) [42] and Lee et al (two rotary axes) [43][44]. The last

type of approaches uses the acceptance test outcomes directly, by assuming the error motions of the linear axes are negligible [30][31]. However, this assumption is not suitable for many cases.

1.6 Closure theory

Although introducing external measuring devices for the calibration is not inappropriate, the complicated setups and operation procedures are not convenient. A simple setup plus a full automated process may be realized with existing CMM and a circular ball plate (CBP) artifact [45]. However, since the designs of the classical CMMs inherently violate the Abbe principle, even the accuracies of the high-end CMMs are not sufficient for this task. Evans et al. [46] reviewed the reversal techniques to minimize the systematic errors of CMMs in many scenarios. They also discussed the closure principle, which was used in the separation of pitch deviations between a workpiece and a measuring device. The closure principle offers a complete, analytical solution with the help of an additional boundary condition or constraint. For example, the angles between adjacent elements of a rotational symmetric workpiece sums up to 360° . The first well-known work was reported by Troughton in 1809 [47] to calibrate divided circular scales. Reeve [48] applied the closure theory to calibrate polygons using a RT and two autocollimators. The Japan National Institute of Advanced Industrial Science and Technology (NMIJ/AIST) determined the gear pitch deviations [49] using multiple-measuring technique [50], which was also based on the closure, to separate the pitch deviations of gear teeth from the ones of the four-axis CMM. The Physikalisch-Technische Bundesanstalt (PTB) accomplished the same task [49] using the three-rosette method [51], which further separated the pitch

deviation of the RT and the three-axis CMM. Günther et al [52] applied the three-rosette method to calibrate a ball plate artifact on a 4-axis CMM.

1.7 Monte Carlo simulation

A calibration method cannot be characterized by an uncertainty value, because this belongs to the entire measurement process. Instead, the term “stability” is used to describe the resistance of a calibration method to different deviation sources.

Monte Carlo simulation is a suitable and often applied tool to investigate this issue. The Monte Carlo method randomly picks a value for each of the deviation contributors, according to their probability density functions (PDFs), and calculates the corresponding deviations of the measurand. After repeating numerous times, a histogram is achieved, which represents the possible outcomes and the statistics of its distribution [53].

1.8 Error motions of RTs under loads

To keep pace with the increasing demands on the measuring volume and load capacity, large-scale RTs are designed and built. Figure 1.11 shows a 1255 kg WES gear placed on a hydrostatic RT for measurement tasks. Complicated aerostatic and hydrostatic bearing systems are employed to provide smooth rotational motion under various maximum loads up to several metric tons.

Although the performances of RTs have been improved by numerous efforts in design and production, there still exist non-trivial and undesired error motions, originating from the drive train, bearings, etc. Commonly, error maps are produced at non-load situations and are used for all loading scenarios. However, this strategy needs to be

reconsidered, when large workpieces with masses up to several tons become the measuring objects. Different loads may deviate the operation conditions of bearings and drive train components by different amounts. It is also not clear whether and how the error motions change in asymmetric loading scenarios. In real applications, gravity centers of non-rotationally symmetric parts may be eccentric to the rotary axis. Rotationally symmetric parts might also not be centered very precisely, because large-scale parts are loaded onto and unloaded off RTs by traveling overhead cranes, fork lifters or lift carriages.

Because of the complicated and nonflexible setup, the traditional calibration methods [38] are not suitable for cases when the RTs are under load. A new calibration method is needed to provide error maps for large RTs with respect to rotary position, load value and load distribution.



Figure 1.11. WES gear loaded on a hydrostatic rotary table at the Bremen Institute for Metrology, Automation and Quality Science (BIMAQ), University of Bremen, Germany.

1.9 Contribution of this research

This research proposes a new RT calibration solution, and verifies it by formula derivation, numerical solution and experimental verification. This solution is characterized by a simple and quick setup, as well as a fully automated measurement process, which makes it suitable to replace the classic methods used for periodical error mapping of RTs in manufacturing facilities and research institutes. Moreover, because the simple and flexible setup is compatible with large-scale workpieces, this new method becomes a powerful tool to study the error motions of RT under various loading scenarios.

The second part of this research observes the error motions of a hydrostatic and an aerostatic RT under various static load scenarios. It provides examples to produce complete error maps regarding the rotary position of RTs, load value and load distribution.

1.10 Dissertation layout

1.10.1 Development of a new calibration method

This research aims at the development of a new solution, which decouples the error motions of RT from the deviations originated from the CMM and from the plate artifact. The development and verification of this method will consist of formula derivation, numerical simulation and experimental verification. Monte Carlo Simulation will be used to investigate the stability of this method.

A mathematical model will be developed, which covers all the deviation sources, occurring at the movement of a rotary axis. Formula derivation will first verify the strengths and limitations of the three-rosette method. Then, an improved solution will combine the

advantages of the three-rosette method and traditional methods. Formula derivation will verify whether the error motions of a RT can be separated using the proposed solution.

Numerical simulations will be performed based on the mathematical model to validate the proposed solution. Simulated data of sphere centers will be generated with given deviation values of the CMM, RT and artifact. Then, the simulated data will be processed to separate the deviations originating from different sources. The separated deviations will be compared to the simulation input for verification purpose.

Experimental verification will be performed by comparing the calibration result of the proposed method with data captured by a spindle error analyzer (SEA) of an aerostatic RT. A ball plate artifact will be fabricated. The metrology frame of a spindle error analyzer (SEA) will be set up.

Stability investigation of this method will be conducted by Monte Carlo simulation. The probability density functions (PDFs) of deviation contributors will be gathered by three ways: experiment, product data sheet and proper assumption.

1.10.2 Error motions of RTs under loads

The error motions of a hydrostatic RT under various load values and load distributions will be studied. Symmetric and asymmetric loading scenarios will be created by manipulating several WES gears. Similar experiments will be performed on two aerostatic RTs. More loading scenarios will be investigated to generate an error map regarding the rotary position, load value and load distribution.

CHAPTER 2: A NEW ERROR MAPPING TECHNIQUE USING A CIRCULAR BALL PLATE

2.1 Introduction

2.1.1 Calibration methods for angular positioning deviation

Commonly, RT calibration refers to the determination of the angular positioning deviation ε_z at multiple rotary positions. The applied measurement setups consist of two parts: an angle measuring instrument including interferometer (or autocollimator) and a calibrated standard such as a precision polygon mirror or a precision indexing table.

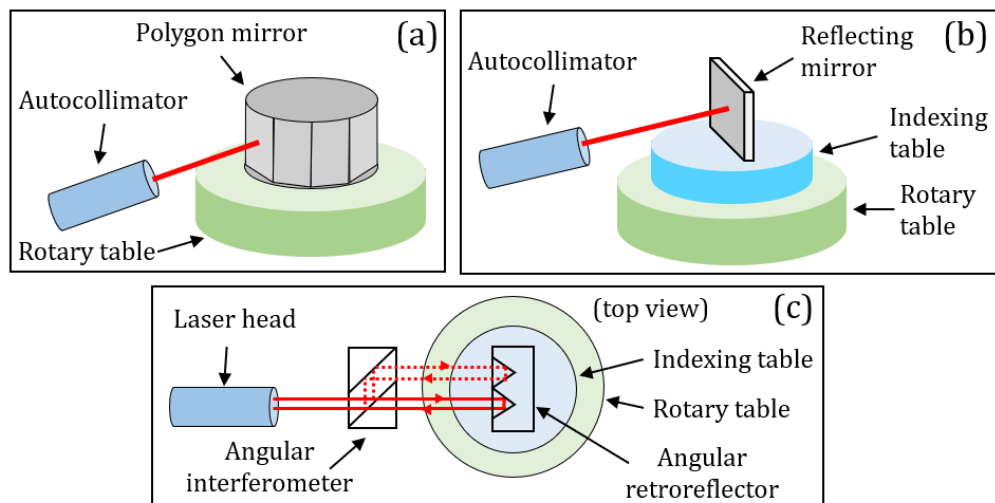


Figure 2.1. Schematic of three measurement setups to calibrate the angular positioning deviation ε_z .

Figure 2.1 shows three usable combinations: (i) an autocollimator and a polygon mirror; (ii) an autocollimator, an indexing table and a reflecting mirror; (iii) an angular interferometer, an indexing table and an angular reflector (double retroreflectors).

In the first setup, one mirror of the precision polygon is initially adjusted perpendicular to the autocollimator. In every step, the table is rotated to align the next mirror. The deviation ε_z is determined by comparing the angle of rotation to the pre-calibrated angle between the current mirror and the previous adjacent mirror. The minimum angular step of the RT equals to 360° divided by the number of mirrors.

In the second and third setups, the standards are also aligned initially towards the angle measuring devices. In every step, the indexing table is rotated by an amount (e.g. 5°) in one direction, and the RT is rotated in the reverse direction to re-align the standard. The differences of absolute rotated angles between the indexing table and the RT is the deviation ε_z . The minimum angular step equals to the resolution of the indexing table. Self-calibration technique can be applied if an uncalibrated indexing table is used in the second and third setups.

2.1.2 Calibration methods for six error motions

Besides ε_z , a RT has additional five error motions. δ_x , δ_y and δ_z denote three translational error motions of RT along x-, y- and z- axes of the CMM's frame coordinate system (CS), respectively. ε_x and ε_y denote two tilt error motions around the x- and y- axes, respectively. (Figure 2.2). Calibrating these five error motions brings significant benefits: (i) in high precision machining, the tool paths can be adjusted to reduce the form deviations of workpieces (ii) in high precision metrology, the measurement data can be corrected to reduce the measurement uncertainties.

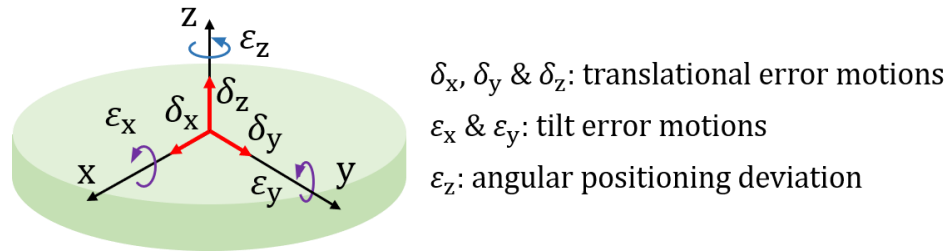


Figure 2.2. Schematic of six error motions of a rotary table.

The conventional calibration method requires two measurement setups for the detection of three translational error motions and three rotational error motions, respectively. In the first setup, three orthogonally-arranged capacitance sensors or linear variable differential transformers (LVDTs) are brought close to a master sphere, which is centered on the RT. The second one is the autocollimation setup for the determination of ϵ_z . If the angular measuring device is aligned along the x-axis, the tilt error motion ϵ_x can be extracted by further processing the data. Similarly, placing the angular measuring device along y-axis can separate ϵ_y [38].

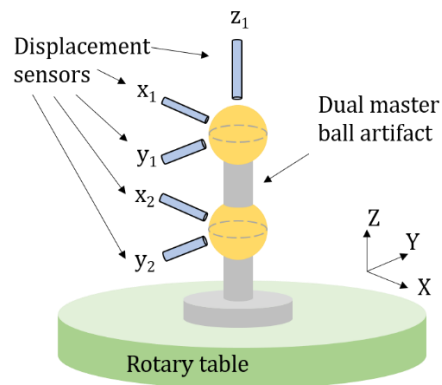


Figure 2.3. Schematic of spindle error analyzer setup on the rotary table.

Alternatively, the tilt error motions ϵ_x and ϵ_y can be determined using a spindle error analyzer. It has a double master ball artifact centered on the RT (Figure 2.3). By

comparing the x displacement motions of the two spheres, ε_x can be extracted. ε_y is determined similarly. This setup can also determine the δ_x , δ_y and δ_z . Nevertheless, another setup is needed to calibrate the ε_z .

Altogether, the conventional calibration methods require two separated measurement setups, an experienced operator and considerable efforts in alignments. Moreover, it is difficult to reduce the measurement uncertainties of angular terms, which are resulting from the measuring device, artifact and alignment process.

2.1.3 Alternative solution

Coordinate measuring machines (CMMs) are versatile instruments that might replace all the measuring devices mentioned before. However, since the designs of the classical CMMs inherently violate the Abbe principle, even the accuracy of the high-end CMMs is not sufficient for this task.

A promising alternative solution is the self-calibration technique. It repeatedly measures the same workpiece at different angular orientation, to separate the pitch deviations between a workpiece and a measuring device. It uses the closure principle, which offers a complete, analytical solution with the help of an additional boundary condition or constraint. For example, the angles between adjacent elements of a rotational symmetric workpiece sums up to 360° . Important works include the calibration of divided circular scales by Troughton in 1809 [47], polygons by Reeve [48], cylindrical workpieces by the Japan National Institute of Advanced Industrial Science and Technology (AIST) and the Physikalisch-Technische Bundesanstalt (PTB) [49][50], a CBP artifact by Günther [52].

While reducing measurement uncertainties, the self-calibration technique further increases the burden for the manual alignment of the artifact and indexing table. The process is very tedious when a small angular step of the RT is desired.

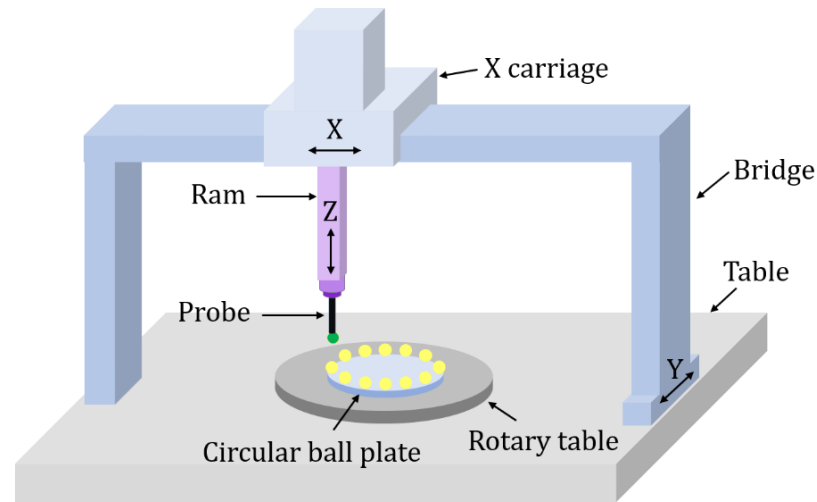


Figure 2.4. Schematic of measurement setup for calibration of RT.

2.2 Experimental setup and data acquisition

CMMs and automatic RTs offer the advantage of repeated measurements. To determine all six error motions, an artifact combining the advantages of precision polygon and master balls was used: a CBP. This rotational symmetric artifact had N ($N \geq 3$) precision spheres evenly distributed in a circular pattern on a base plate. It was centered and kinematically clamped on the RT (Figure 2.4).

The data acquisition procedure consisted of preparation phase and the measurement, as shown in Figure 2.5. During preparation, the first two steps were qualifying a vertical probe and building the RT CS. Then, the artifact was centered on the RT by measuring the cylindrical surface of the base plate. A trial and error method was used to reduce the eccentricity of the artifact to less than $100 \mu\text{m}$. Because the center of

artifact was defined by the least squares center of all the spheres, the exact eccentricity values were calculated later. Once the alignment was completed, the artifact was fixed on the table. The spheres should be cleaned carefully to avoid influences of sampled points affected by dirt. In the fourth step, the CMM coordinates of all the spheres were monitored every few minutes, until their coordinates become stable. Next, the RT should be warmed up by rotating tens of cycles in both rotating directions to reach a stable operating condition.

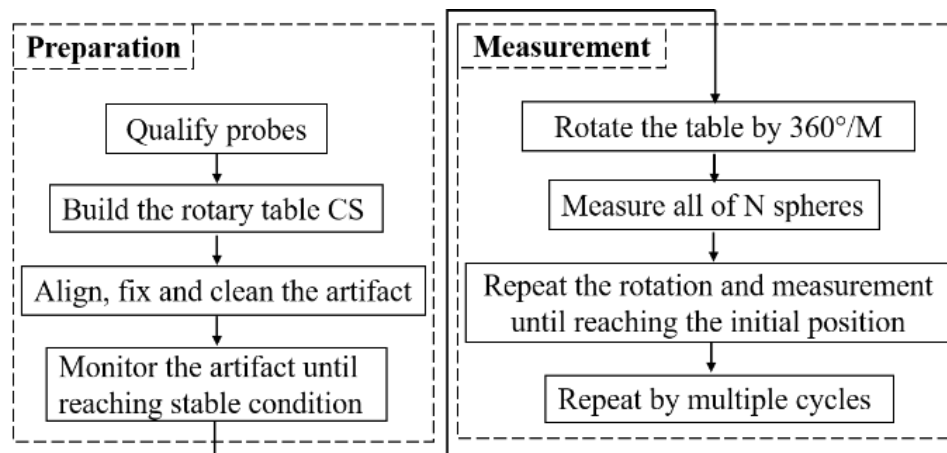


Figure 2.5. Schematic of the preparation and measurement procedure for rotary table calibration.

The measurement was based on a M -step repeated measurement. In each step, the table was rotated by $360^\circ/M$ and all the spheres are measured. Usually, M was a multiple of N to increase the sample density. The RT should be calibrated by more than one cycle for three purposes: (i) the period of error motions may be longer than 2π ; (ii) check the repeatability; (iii) double check to see if the RT was properly warmed up (i.e. thermally stable).

Compared with conventional methods, the proposed method had a simpler setup, easier alignment procedure and fully automated measurement procedure.

2.3 Mathematical model

Rigid body kinematics is one of the most commonly used modelling techniques for machine tool error characterization. To understand how a sphere center was measured and calculated by CMM, a frame-based vector model was developed. It included two chains of coordinate systems from the origin of the frame CS (FCS) to a sphere center of the CBP: (i) the first chain was from the FCS to the rotary table CS (RTCS) to the artifact CS (ACS) to the sphere center, providing the actual coordinates of a sphere center in the FCS; (ii) the second chain was from the FCS to the XCS to the YCS to the ZCS to the probe CS (SCS) to the sphere center, giving the measured coordinates of a sphere in the FCS. XCS, YCS and ZCS were coordinate systems associated with the X, Y and Z carriages respectively. Taking all the deviation sources into account, the two chains lead to same coordinates of a sphere center in the FCS.

2.3.1 First chain of coordinate systems (CSs)

The first chain is explained as follows.

The 1st sphere on the CBP was aligned on the positive x-axis of the FCS. Spheres were numbered in the counter-clock-wise (CCW) direction. Equation 2.1 gives the nominal angular position $\varphi_{0(j)}$ of the j^{th} sphere.

$$\varphi_{0(j)} = (j - 1) \times \frac{2\pi}{N} \quad (2.1)$$

The ACS was defined as following. A plane and a circle were approximated to all the sphere centers at the initial rotary position (0°), respectively. The circle center was defined as the origin O_A of the ACS. The positive x-axis was from the O_A to the 1st

sphere's center. The z-axis was parallel to the normal vector of the approximated plane. The nominal and actual coordinates of the j^{th} sphere in the ACS, $[S_{0(j)}]_A$ and $[S_j]_A$, are given in Equation 2.2 and Equation 2.3, respectively.

$$[S_{0(j)}]_A = \begin{bmatrix} r_{s0} \cos \varphi_{0(j)} \\ r_{s0} \sin \varphi_{0(j)} \\ 0 \end{bmatrix}_A \quad (2.2)$$

$$[S_j]_A = \begin{bmatrix} (r_{s0} + \Delta r_{s(j)}) \cos(\varphi_{0(j)} + \Delta \varphi_j) \\ (r_{s0} + \Delta r_{s(j)}) \sin(\varphi_{0(j)} + \Delta \varphi_j) \\ \Delta z_{s(j)} \end{bmatrix}_A \quad (2.3)$$

As shown Figure 2.6, in $\Delta r_{s(j)}$, $\Delta \varphi_j$ and $\Delta z_{s(j)}$ denoted the deviations of the j^{th} sphere center along the radial, angular and z directions, respectively. r_{s0} denoted the mean radial position of all the spheres.

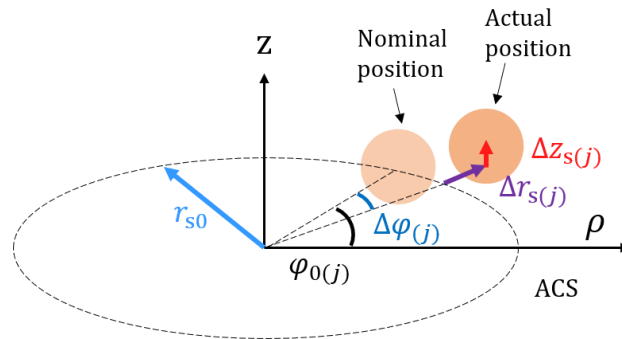


Figure 2.6. Position deviations of the j^{th} sphere in the ACS.

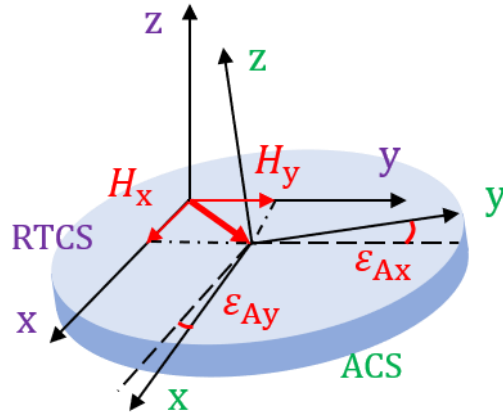


Figure 2.7. Schematic of the artifact's eccentricity and tilt deviations.

Figure 2.7 demonstrates the tilt and eccentricity of the ACS referring to the RTCS. A plane was approximated to all sphere centers at the initial rotary position. In rotational matrix $R_{A,RT}$ from the ACS to the RTCS (Equation 2.4), ϵ_{Ax} and ϵ_{Ay} denoted the tilt deviations of the ACS about the x-axis and y-axis of the RTCS, respectively. Vector $[H]_{RT}$ refers to coordinates of O_A in the RTCS (Equation 2.5).

$$R_{A,RT} = \begin{bmatrix} 1 & 0 & \epsilon_{Ay} \\ 0 & 1 & -\epsilon_{Ax} \\ -\epsilon_{Ay} & \epsilon_{Ax} & 1 \end{bmatrix} \quad (2.4)$$

$$[H]_{RT} = \begin{bmatrix} H_x \\ H_y \\ H_z \end{bmatrix}_{RT} \quad (2.5)$$

Therefore, the coordinates of the j^{th} sphere in the RTCS were given in Equation 2.6.

$$[L(j)]_{RT} = [H]_{RT} + R_{A,RT}[S(j)]_A \quad (2.6)$$

According to ASME B89.3.4 [54], The axis average line is a line segment passing through two axially separated radial error motion polar profile centers. In this dissertation, the origin O_{RT} of the RTCS was defined as the intersection point of axis average line and

the XY plane which contained O_A . Therefore, H_z was equal to zero. The z-axis was along the axis average line. The x-axis and y-axis were along the corresponding axes of the FCS, respectively. The coordinates of O_{RT} in the FCS were given in Equation 2.7, without considering the translational error motions.

$$[T]_F = \begin{bmatrix} T_x \\ T_y \\ T_z \end{bmatrix}_F \quad (2.7)$$

The translational error motions of the RT at the i^{th} rotary position were given in Equation 2.8.

$$[\Delta C_{(i)}]_F = \begin{bmatrix} \delta_{x(i)} \\ \delta_{y(i)} \\ \delta_{z(i)} \end{bmatrix}_F \quad (2.8)$$

Rotation matrix $R_{RT,F}$ from the RTCS to the FCS was the product of two matrices (Equation 2.9). One matrix described the rotation of the RT, while the other one defined the tilt error motions of the RT. $\theta_{0(i)}$ was the nominal rotary angle of the RT at the i^{th} rotary position.

$$R_{RT,F(i)} = \begin{bmatrix} 1 & 0 & \varepsilon_{y(i)} \\ 0 & 1 & -\varepsilon_{x(i)} \\ -\varepsilon_{y(i)} & \varepsilon_{x(i)} & 1 \end{bmatrix} \begin{bmatrix} \cos(\theta_{0(i)} + \varepsilon_{z(i)}) & -\sin(\theta_{0(i)} + \varepsilon_{z(i)}) & 0 \\ \sin(\theta_{0(i)} + \varepsilon_{z(i)}) & \cos(\theta_{0(i)} + \varepsilon_{z(i)}) & 0 \\ 0 & 0 & 1 \end{bmatrix} \quad (2.9)$$

$[P_{F(i,j)}]_F$ in Equation 2.10 denotes the actual coordinates of the j^{th} sphere at the i^{th} rotary position in the FCS.

$$[P_{F(i,j)}]_F = R_{RT,F(i)}[L_{(j)}]_{RT} + [\Delta C_{(i)}]_F + [T]_F \quad (2.10)$$

2.3.2 Second chain of CSs

A key challenge to separate the various error motions was the identification and compensation of the CMM's deviations. With limited information, it was not possible to fully calibrate the 21 deviations of CMM guideways. Therefore, an alternative solution is given.

At each rotary position, the probe moved along the boundary of a polygon area, defined by the CBP, to measure all the spheres (Figure 2.8(a)). The path of the probe through the experiment was enclosed by a narrow band (Figure 2.8(b)), where $r_{out} = r_{s0}$ and $r_{in} = r_{s0} \cos \frac{180}{N}$.

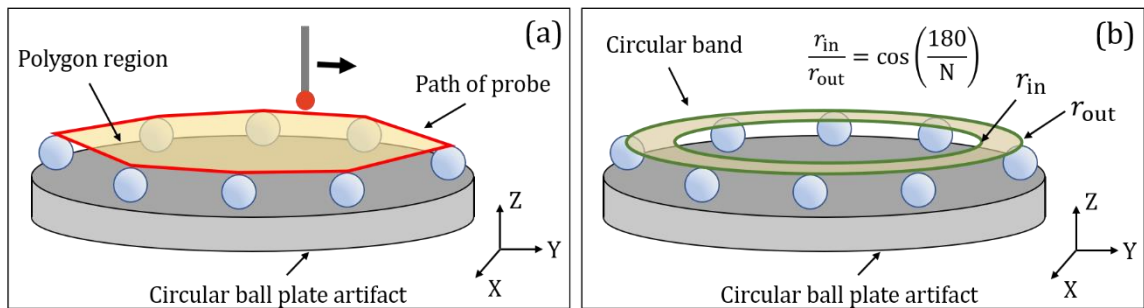


Figure 2.8. Path of probe in RT calibration: (a) the path of probe at measuring all spheres at a rotary position (b) the path of the probe through the experiment was enclosed by a narrow band.

Figure 2.9 shows the schematic of $M \times N$ spheres centers after one complete rotation of the ball plate ($M = 24$, $N = 6$). Each sphere was positioned once near each of the 24 defined measuring positions. The position deviations of every sphere center to the nominal one resulted from four sources: (i) the error motions of the RT; (ii) fabrication accuracy of the artifact's base plate; (iii) assembly accuracy of the artifact; (iv) eccentricity of artifact relative to axis of rotation. Although there are no strict requirements on

sources (ii) – (iv), reaching the following conditions helps simplifying the model of CMM deviations: (1) the radial, pitch and axial deviations of each sphere on the ball plate should be less than $100 \mu\text{m}$ [10]; (2) the artifact should be centered on the table within a $100 \mu\text{m}$ range.

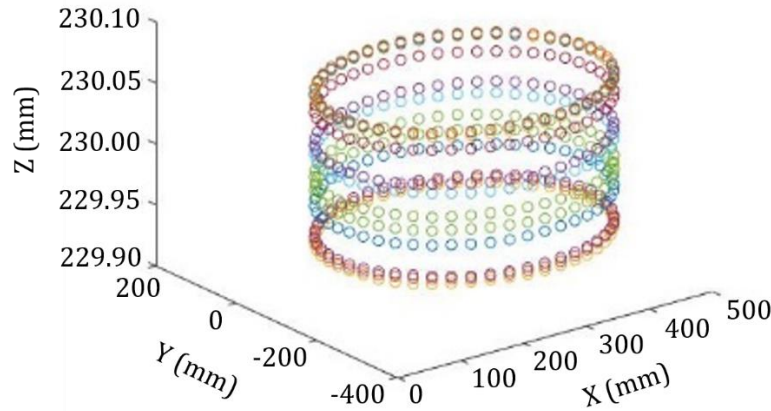


Figure 2.9. Schematic of the $M \times N$ sphere centers after one complete rotation of the ball plate.

The $M \times N$ sphere centers were within a 1 mm distance from the corresponding measuring positions. Consequently, it seemed reasonable to assume that the CMM's systematic deviations were nearly constant within this range around one ideal measuring position, where N different spheres centers were measured. Therefore, this method focused on the CMM's geometric deviations at measuring the relative coordinates of these 24 positions to with respect to the reference point.

In this case, the 21 parametric deviations of CMM guideways were replaced by two $[x, y, z]$ vectors: $[\Delta P_{gs(k)}]$ and $[\Delta P_{gr(i,j)}]$. $[\Delta P_{gs(k)}]$ denoted the systematic deviations and $[\Delta P_{gr(i,j)}]$ denoted the stochastic deviations, respectively, of length measurement from the artifact center to one sphere center.

The orders of rotary positions ($i = 1, 2, \dots, M$) and measuring positions ($k = 1, 2, \dots, M$) were all defined in the CCW direction. The order of spheres ($j = 1, 2, \dots, N$) was defined in the CW direction. The relationships of i, j and k are given in Equation 2.11. If the Equation 2.11 yielded a value larger than M , i should be deducted by M .

$$i = k + \frac{M}{N}(j - 1) \quad (2.11)$$

The deviation sources from probing system were classified into three subgroups: (a) uncorrected systematic probing deviations, form deviation of stylus tip, sampling strategy, probing parameter; (b) apparent random probing deviations; (c) probe changing and probe articulation uncertainties.

In this model, the vector $[\Delta P_{ps(i,j)}]$ referred to the systematic probing deviation at the point-based measurement of a master sphere. This vector was the superimposed result of all the sources in each subgroup (a). Due to the necessary accuracy and the complexity of interactions, group (a) deviation sources cannot be determined with experiments or predicted with simulation. Alternatively, the subscripts i and j were dropped by applying the same probing system setup and data acquisition strategy, including number, location and sequence of probing points, probe approaching speed and probing force, etc. Vector $[\Delta P_{pr(i,j)}]$ represented the stochastic components of probing error from subgroup (b). Subgroup (c) deviation sources can be avoided by using a single vertical stylus in the entire experiment.

The determined coordinates of the j^{th} sphere center at the i^{th} rotary position are expressed by Equation 2.12. Every component is explained in Table 2.1. This model

provided a foundation to investigate the applicability of the self-calibration technique in identifying the error motions.

$$\begin{aligned} [P_{m(i,j)}]_F = & R_{RT,F} \left([H]_{RT} + R_{A,RT} [S_{(j)}]_A \right) + [\Delta C_{(i)}]_F + [T]_F + [\Delta P_{gs(k)}]_F \\ & + [\Delta P_{gr(i,j)}]_F + [\Delta P_{ps}]_F + [\Delta P_{pr(i,j)}]_F \end{aligned} \quad (2.12)$$

Table 2.1. Nomenclature (vector model).

ACS	artifact CS
FCS	frame CS
RTCS	rotary table CS
$[P_{m(i,j)}]_F$	coordinates of the (i^{th}, j^{th}) sphere center in the FCS
$R_{A,RT}$	rotation matrix from the ACS to the RTCS
$R_{RT,F}$	rotation matrix from the RTCS to the FCS
$[S_{(j)}]_A$	coordinates of the center of the j^{th} sphere in the ACS
$[H]_{RT}$	coordinates of the artifact center in the RTCS
$[\Delta C_{(i)}]_F$	translational error motions at the i^{th} rotary position in the FCS
$[T]_F$	coordinates of the origin O_C in the FCS
$[\Delta P_{gs(k)}]_F$	systematic components of the 21 parametric deviations at the k^{th} measuring position
$[\Delta P_{ps}]_F$	systematic components of the probing error in the measurement
$[\Delta P_{pr(i,j)}]_F$	random components of the probing error in the (i^{th}, j^{th}) measurement

Figure 2.10 shows that a frame-based vector model was developed to illustrate the chain of coordinate systems from the frame CS (CMM) to the sphere center.

The vector equation is

$$\vec{T} + \vec{H} + \vec{L} = \vec{X} + \vec{Y} + \vec{Z} + \vec{S} + \vec{P} \quad (2.13)$$

where

\vec{L} is the position of the probe tip represented in the artifact CS (ACS);

\vec{H} is the position of the origin O_A in the rotary table CS (RTCS);

\vec{T} is the position of the origin O_{RT} in the frame CS (FCS);

\vec{X} is the position of the origin O_X in the FCS;

\vec{Y} is the position of the origin O_Y in the XCS;

\vec{Z} is the position of the origin O_Z in the YCS;

\vec{S} is the position of the origin O_S in the ZCS;

\vec{P} is the position of the probe tip in the Probe CS (PCS).

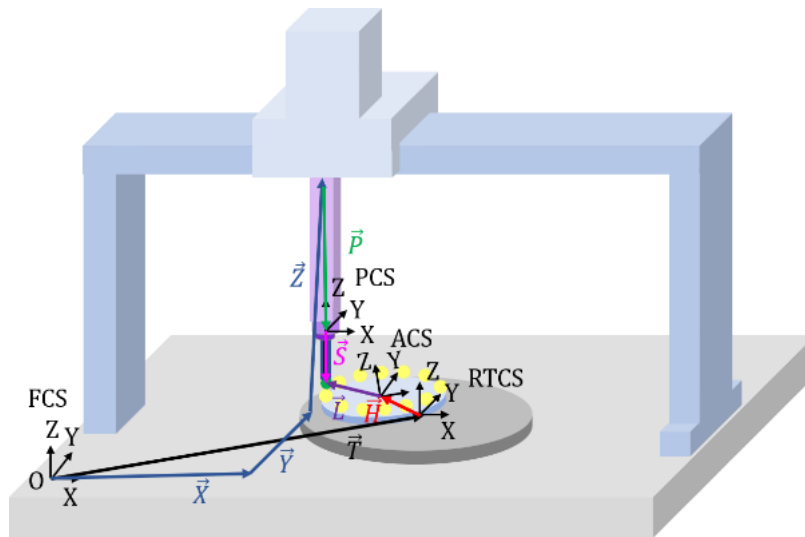


Figure 2.10. Developed mathematical vector model illustrating the chain of coordinate systems from the frame CS (CMM) to the sphere center.

An aligned workpiece CS (AWCS) was built as follows. A sphere was approximated to the coordinates of $M \times N$ spheres. The sphere was represented by Equation 2.14.

$$(x - x_{wo})^2 + (y - y_{wo})^2 + (z - z_{wo})^2 = r_{wo}^2 \quad (2.14)$$

The square root of the sum of squared deviations was defined in Equation 2.15.

$$E(x_{wo}, y_{wo}, z_{wo}, r_{wo}) = \sqrt{\sum_{i=1}^M \sum_{j=1}^N (L_{r(i,j)} - r_{wo})^2} \quad (2.15)$$

where

$$L_{r(i,j)} = \sqrt{(x_{m(i,j)} - x_{w0})^2 + (y_{m(i,j)} - y_{w0})^2 + (z_{m(i,j)} - z_{w0})^2} \quad (2.16)$$

The partial derivatives of $E(x_{w0}, y_{w0}, z_{w0}, r_{w0})$ with respect to r_{w0} , x_{w0} , y_{w0} and z_{w0} were set as zeros. Then, the solutions for the r_{w0} , x_{w0} , y_{w0} and z_{w0} were given in Equation 2.17 and Equation 2.18:

$$r_{w0} = \frac{\sum_{i=1}^M \sum_{j=1}^N L_{r(i,j)}}{MN} \quad (2.17)$$

$$\begin{bmatrix} x_{w0} \\ y_{w0} \\ z_{w0} \end{bmatrix} = \frac{1}{\sum_{i=1}^M \sum_{j=1}^N \left(1 - \frac{r_{w0}}{L_{r(i,j)}}\right)} \begin{bmatrix} \sum_{i=1}^M \sum_{j=1}^N x_{m(i,j)} \left(1 - \frac{r_{w0}}{L_{r(i,j)}}\right) \\ \sum_{i=1}^M \sum_{j=1}^N y_{m(i,j)} \left(1 - \frac{r_{w0}}{L_{r(i,j)}}\right) \\ \sum_{i=1}^M \sum_{j=1}^N z_{m(i,j)} \left(1 - \frac{r_{w0}}{L_{r(i,j)}}\right) \end{bmatrix} \quad (2.18)$$

Iterative process involving Equation 2.15, Equation 2.16, Equation 2.17 and Equation 2.18 gave the center position and radius of the sphere. The initial values of x_{w0} , y_{w0} and z_{w0} used the mean coordinates of all the measured spheres. The center of the approximated sphere as defined as the origin of AWCS. x-axis and z-axis were same as the ones of FCS. Equation 2.19 and its expansion Equation 2.20 described the (i^{th} , j^{th}) sphere center position in the AWCS. The random deviations $[\Delta P_{gr(i,j)}]$ and $[\Delta P_{pr(i,j)}]$ were temporarily ignored in the formula derivation of Equation 2.19. It should be emphasized that the vector $[\Delta P_{ps}]$ representing the systematic probing errors was eliminated because it was a constant vector. Therefore, the calibration results of the RT were freed from this uncertainty source.

$$[P_{m(i,j)}]_{AW} = R_{RT,AW} \left([H]_{RT} + R_{A,RT} [S_{(j)}]_A \right) + [\Delta C_{(i)}]_{AW} + [\Delta P_{gs(k)}]_{AW} \quad (2.19)$$

$$\begin{aligned} \begin{bmatrix} x_{m(i,j)} \\ y_{m(i,j)} \\ z_{m(i,j)} \end{bmatrix}_{AW} &= \begin{bmatrix} 1 & 0 & \varepsilon_{y(i)} \\ 0 & 1 & -\varepsilon_{x(i)} \\ -\varepsilon_{y(i)} & \varepsilon_{x(i)} & 1 \end{bmatrix} \begin{bmatrix} \cos(\theta_{0(i)} + \varepsilon_{z(i)}) & -\sin(\theta_{0(i)} + \varepsilon_{z(i)}) & 0 \\ \sin(\theta_{0(i)} + \varepsilon_{z(i)}) & \cos(\theta_{0(i)} + \varepsilon_{z(i)}) & 0 \\ 0 & 0 & 1 \end{bmatrix} \\ &\times \left\{ \begin{bmatrix} H_x \\ H_y \\ H_z \end{bmatrix}_{RT} + \begin{bmatrix} 1 & 0 & \varepsilon_{Ay} \\ 0 & 1 & -\varepsilon_{Ax} \\ -\varepsilon_{Ay} & \varepsilon_{Ax} & 1 \end{bmatrix} \begin{bmatrix} (r_{s0} + \Delta r_{s(j)}) \cos(\varphi_{0(j)} + \Delta \varphi_j) \\ (r_{s0} + \Delta r_{s(j)}) \sin(\varphi_{0(j)} + \Delta \varphi_j) \\ \Delta z_{s(j)} \end{bmatrix}_A \right\} \\ &+ \begin{bmatrix} \delta_{x(i)} \\ \delta_{y(i)} \\ \delta_{z(i)} \end{bmatrix}_{AW} + \begin{bmatrix} \Delta x_{gs(k)} \\ \Delta y_{gs(k)} \\ \Delta z_{gs(k)} \end{bmatrix}_{AW} \end{aligned} \quad (2.20)$$

Table 2.2. Nomenclature (AWCS).

Artifact	
H_x	position of the artifact center in the RTCS along the x-axis
H_y	position of the artifact center in the RTCS along the y-axis
H_z	position of the artifact center in the RTCS along the z-axis
ε_{Ax}	tilt deviation of the artifact about the x-axis
ε_{Ay}	tilt deviation of the artifact about the y-axis
r_{s0}	average radial distance of the spheres to the artifact's center
$\Delta r_{s(j)}$	radial deviation of the j^{th} sphere
$\varphi_{0(j)}$	nominal angular position of the j^{th} sphere center
$\Delta \varphi_{(j)}$	angular deviation of the j^{th} sphere center
$\Delta z_{s(j)}$	axial deviation of the j^{th} sphere
RT	
$\theta_{0(i)}$	nominal rotary angle of RT at the i^{th} rotary position
θ_i	actual rotary angle of RT at the i^{th} rotary position
CMM	
$\Delta x_{gs(k)}$	systematic components of the geometric deviations at the k^{th} measuring position along the x-axis
$\Delta y_{gs(k)}$	systematic components of the geometric deviations at the k^{th} measuring position along the y-axis
$\Delta z_{gs(k)}$	systematic components of the geometric deviations at the k^{th} measuring position along the z-axis

2.4 Data processing

2.4.1 Extend three-rosette method for error separation

The coordinates of sphere centers in the AWCS $[P_{m(i,j)}]_{AWCS}$ were translated from the Cartesian CS (Equation 2.21) to Cylindrical CS (Equation 2.22).

$$[P_{m(i,j)}]_{AWCS} = \begin{bmatrix} x_{m(i,j)} \\ y_{m(i,j)} \\ z_{m(i,j)} \end{bmatrix}_{AWCS} \quad (2.21)$$

$$[P_{m(i,j)}]_{AWCS,CYL} = \begin{bmatrix} r_{m(i,j)} \\ \tau_{m(i,j)} \\ z_{m(i,j)} \end{bmatrix}_{AWCS,CYL} \quad (2.22)$$

The differences between the actual and nominal coordinates, $[\Delta P_{m(i,j)}]_{AWCS,CYL}$, were calculated in Equation 2.23 and its expansion: Equation 2.24 and Equation 2.25. In the process, $\delta_{x(i)}$ and $\delta_{y(i)}$ were converted to a radial term $\Delta r_{ct(i,j)}$ and an angular term $\Delta \theta_{ct(i,j)}$. The latter one also deviated the angular position of a targeted sphere. As shown in Equation 2.23, there were four deviation sources in the radial direction and five deviation sources in angular direction, respectively.

$$\begin{bmatrix} \Delta r_{m(i,j)} \\ \Delta \tau_{m(i,j)} \\ \Delta z_{m(i,j)} \end{bmatrix} = \left\{ \begin{bmatrix} r_{H(j)} \\ \varphi_{H(j)} \\ 0 \end{bmatrix} + \begin{bmatrix} \Delta r_{s(j)} \\ \Delta \varphi_{(j)} \\ \Delta z_{s(j)} \end{bmatrix} \right\} + \left\{ \begin{bmatrix} 0 \\ \varepsilon_{z(i)} \\ 0 \end{bmatrix} + \begin{bmatrix} \Delta r_{ct(i,j)} \\ \Delta \theta_{ct(i,j)} \\ \delta_{z(i)} \end{bmatrix} \right\} + \begin{bmatrix} \Delta r_{gs(k)} \\ \Delta \tau_{gs(k)} \\ \Delta z_{gs(k)} \end{bmatrix} \quad (2.23)$$

where

$$\begin{bmatrix} \Delta r_{m(i,j)} \\ \Delta \tau_{m(i,j)} \\ \Delta z_{m(i,j)} \end{bmatrix} = \begin{bmatrix} \sqrt{x_{m(i,j)}^2 + y_{m(i,j)}^2} - r_{s0} \\ \tan^{-1} \frac{y_{m(i,j)}}{x_{m(i,j)}} - \varphi_{0(j)} - \theta_{0(i)} \\ z_{m(i,j)} - L_{(i,j)} \end{bmatrix} \quad (2.24)$$

$$\begin{aligned}
\begin{bmatrix} r_{H(j)} \\ \varphi_{H(j)} \\ 0 \end{bmatrix} + \begin{bmatrix} \Delta r_{ct(i,j)} \\ \Delta \theta_{ct(i,j)} \\ \delta_{z(i)} \end{bmatrix} + \begin{bmatrix} \Delta r_{gs(k)} \\ \Delta \tau_{gs(k)} \\ \Delta z_{gs(k)} \end{bmatrix} &= \begin{bmatrix} \sqrt{H_x^2 + H_y^2} \cos\left(\tan^{-1} \frac{H_y}{H_x} - \varphi_{0(j)}\right) \\ \sqrt{H_x^2 + H_y^2} \sin\left(\tan^{-1} \frac{H_y}{H_x} - \varphi_{0(j)}\right) \\ r_{s0} \\ 0 \end{bmatrix} \\
+ \begin{bmatrix} \cos(\varphi_{0(j)} + \theta_{0(i)}) & \sin(\varphi_{0(j)} + \theta_{0(i)}) & 0 \\ -\frac{\sin(\varphi_{0(j)} + \theta_{0(i)})}{r_{s0}} & \frac{\cos(\varphi_{0(j)} + \theta_{0(i)})}{r_{s0}} & 0 \\ 0 & 0 & 1 \end{bmatrix} \left\{ \begin{bmatrix} \delta_{x(i)} \\ \delta_{y(i)} \\ \delta_{z(i)} \end{bmatrix} + \begin{bmatrix} \Delta x_{gs(k)} \\ \Delta y_{gs(k)} \\ \Delta z_{gs(k)} \end{bmatrix} \right\} & \quad (2.25)
\end{aligned}$$

where

$$L_{(i,j)} \approx r_{s0} \begin{pmatrix} \varepsilon_{x(i)} \sin(\varphi_{0(j)} + \theta_{0(i)}) - \varepsilon_{y(i)} \cos(\varphi_{0(j)} + \theta_{0(i)}) \\ + \varepsilon_{Ax} \sin \varphi_{0(j)} - \varepsilon_{Ay} \cos \varphi_{0(j)} \end{pmatrix} \quad (2.26)$$

PTB proposed the three-rosette method [49] to separate the angular deviations of the workpiece from those of the RT and 3-axis CMM. It should be noted that the number of rotary positions M was equal to the number of features N (e.g., tooth number of a gear).

Table 2.3. Rosette table for the angular direction ($M = N = 3$).

		Sphere		
		#1	#2	#3
Rotary position	#1	$\Delta \tau_{m(1,1)}$	$\Delta \tau_{m(1,2)}$	$\Delta \tau_{m(1,3)}$
	#2	$\Delta \tau_{m(2,1)}$	$\Delta \tau_{m(2,2)}$	$\Delta \tau_{m(2,3)}$
	#3	$\Delta \tau_{m(3,1)}$	$\Delta \tau_{m(3,2)}$	$\Delta \tau_{m(3,3)}$

To explain the applicability of this method in calibrating the angular positioning deviation of a RT, a 3×3 table ($M = N = 3$) was created (Table 2.3). This table was filled with the total angular deviations $\Delta \tau_{m(i,j)}$, which consisted of five components from the three deviation sources. The i^{th} row represented the i^{th} rotary position, while the j^{th} column represented the j^{th} sphere. This method stated that averaging the j^{th} column

returned the component from the j^{th} sphere, since the components from the other two parts were neutralized because of closure. Similarly, the components of the RT and the CMM can be determined by averaging every column and every diagonal, respectively. Here, the three diagonals in Table 2.3 were defined as: (i) (1,1) \rightarrow (2,2) \rightarrow (3,3); (ii) (2,1) \rightarrow (3,2) \rightarrow (1,3). (ii) (3,1) \rightarrow (1,2) \rightarrow (2,3). The three-rosette method also minimized the negative contributions from the stochastic components from the CMM's 21 parametric deviations and the probing errors, because of averaging effect.

With proper boundary conditions, it is possible to extend this method to the radial and axial directions by filling the $\Delta r_{m(i,j)}$ and $\Delta z_{m(i,j)}$ into two tables (Table 2.4 and Table 2.5). Boundary conditions to fulfil closure were employed. First, the accumulative deviations of the spheres in the angular, radial and z directions equal to zeros, respectively. Then, it was assumed that the 3-axis CMM showed a consistent performance, when the probe returned the same position following a closed loop. Therefore, the accumulative deviations of the CMM along the closed x, y and z paths equal to zeros, respectively. At last, it is assumed that the six error motions of RT have periods equal to 2π (This can be an incorrect assumption and is shown later).

Table 2.4. Rosette table for the radial direction ($M = N = 3$).

		Sphere		
		#1	#2	#3
Rotary position	#1	$\Delta r_{m(1,1)}$	$\Delta r_{m(1,2)}$	$\Delta r_{m(1,3)}$
	#2	$\Delta r_{m(2,1)}$	$\Delta r_{m(2,2)}$	$\Delta r_{m(2,3)}$
	#3	$\Delta r_{m(3,1)}$	$\Delta r_{m(3,2)}$	$\Delta r_{m(3,3)}$

Table 2.5. Rosette table for the axial direction ($M = N = 3$).

		Sphere		
		#1	#2	#3
Rotary position	#1	$\Delta z_{m(1,1)}$	$\Delta z_{m(1,2)}$	$\Delta z_{m(1,3)}$
	#2	$\Delta z_{m(2,1)}$	$\Delta z_{m(2,2)}$	$\Delta z_{m(2,3)}$
	#3	$\Delta z_{m(3,1)}$	$\Delta z_{m(3,2)}$	$\Delta z_{m(3,3)}$

Each diagonal in Table 2.3, Table 2.4 and Table 2.5 was averaged. It was equal to calculate the mean value of three cells in each diagonal according to the Equation 2.23.

$$\frac{1}{3} \begin{bmatrix} \sum_{j=1}^3 \Delta r_{m(i,j)} \\ \sum_{j=1}^3 \Delta \tau_{m(i,j)} \\ \sum_{j=1}^3 \Delta z_{m(i,j)} \end{bmatrix} = \frac{1}{3} \begin{bmatrix} \sum_{j=1}^3 r_{H(j)} \\ \sum_{j=1}^3 \varphi_{H(j)} \\ 0 \end{bmatrix} + \frac{1}{3} \begin{bmatrix} \sum_{j=1}^3 \Delta r_{s(j)} \\ \sum_{j=1}^3 \Delta \varphi(j) \\ \sum_{j=1}^3 \Delta z_{s(j)} \end{bmatrix} + \frac{1}{3} \begin{bmatrix} 0 \\ \sum_{i=1}^3 \varepsilon_{z(i)} \\ 0 \end{bmatrix} +$$

$$\frac{1}{3} \begin{bmatrix} \sum_{j=1}^3 \Delta r_{ct(i,j)} \\ \sum_{j=1}^3 \Delta \theta_{ct(i,j)} \\ \sum_{j=1}^3 \delta_{z(i)} \end{bmatrix} + \begin{bmatrix} \Delta r_{gs(k)} \\ \Delta \tau_{gs(k)} \\ \Delta z_{gs(k)} \end{bmatrix} = \frac{1}{3} \begin{bmatrix} 0 \\ 0 \\ 0 \end{bmatrix} + \frac{1}{3} \begin{bmatrix} 0 \\ 0 \\ 0 \end{bmatrix} + \frac{1}{3} \begin{bmatrix} 0 \\ 0 \\ 0 \end{bmatrix} + \frac{1}{3} \begin{bmatrix} 0 \\ 0 \\ 0 \end{bmatrix} + \begin{bmatrix} \Delta r_{gs(k)} \\ \Delta \tau_{gs(k)} \\ \Delta z_{gs(k)} \end{bmatrix} \quad (2.27)$$

where

$$i = k + j - 1 \quad (i = i - 3 \text{ if } i > 3) \quad (2.28)$$

Therefore,

$$\begin{bmatrix} \Delta r_{gs(k)} \\ \Delta \tau_{gs(k)} \\ \Delta z_{gs(k)} \end{bmatrix} = \frac{1}{3} \begin{bmatrix} \sum_{j=1}^3 \Delta r_{m(i,j)} \\ \sum_{j=1}^3 \Delta \tau_{m(i,j)} \\ \sum_{j=1}^3 \Delta z_{m(i,j)} \end{bmatrix} \quad (2.29)$$

As shown in Equation 2.27, 2.28 and 2.29, the CMM's deviations were separated. Then, the three tables were updated by removing the determined CMM deviations. At separating the error motions of the RT, the Δr_{ct} and $\Delta \theta_{ct}$ were neutralized (Equation 2.30). On one hand, no information about the δ_x and δ_y was acquired. On the other hand, the $\Delta \theta_{ct}$ did not influence the separation of ε_z .

$$\begin{aligned} \frac{1}{3} \begin{bmatrix} \sum_{j=1}^3 \Delta r_{ct(i,j)} \\ \sum_{j=1}^3 \Delta \theta_{ct(i,j)} \end{bmatrix} &= \frac{1}{3} \begin{bmatrix} \sum_{j=1}^3 \cos(\varphi_{0(j)} + \theta_{0(i)}) & \sum_{j=1}^3 \sin(\varphi_{0(j)} + \theta_{0(i)}) \\ \frac{-1}{r_{s0}} \sum_{j=1}^3 \sin(\varphi_{0(j)} + \theta_{0(i)}) & \frac{1}{r_{s0}} \sum_{j=1}^3 \cos(\varphi_{0(j)} + \theta_{0(i)}) \end{bmatrix} \begin{bmatrix} \delta_{x(i)} \\ \delta_{y(i)} \end{bmatrix} \\ &= \begin{bmatrix} 0 \\ 0 \end{bmatrix} \end{aligned} \quad (2.30)$$

Moreover, the r_H and φ_H were also neutralized (Equation 2.31).

$$\frac{1}{3} \begin{bmatrix} \sum_{j=1}^3 r_{H(j)} \\ \sum_{j=1}^3 \varphi_{H(j)} \end{bmatrix} = \frac{\sqrt{H_x^2 + H_y^2}}{3} \begin{bmatrix} \sum_{j=1}^3 \cos\left(\tan^{-1} \frac{H_y}{H_x} - \varphi_{0(j)}\right) \\ \frac{1}{r_{s0}} \sum_{j=1}^3 \sin\left(\tan^{-1} \frac{H_y}{H_x} - \varphi_{0(j)}\right) \end{bmatrix} = \begin{bmatrix} 0 \\ 0 \end{bmatrix} \quad (2.31)$$

It had important practical meaning that ideally centering the artifact was not necessary for the extraction of ε_z (Equation 2.32). Although the second terms on the right side of Equation 2.32 were not always equal to zeros, they can be calculated with results from Equation 2.27. The δ_z was also extracted successfully.

$$\begin{bmatrix} 0 \\ \varepsilon_{z(i)} \\ \delta_{z(i)} \end{bmatrix} = \frac{1}{3} \begin{bmatrix} \sum_{j=1}^3 \Delta r_{m(i,j)} \\ \sum_{j=1}^3 \Delta \tau_{m(i,j)} \\ \sum_{j=1}^3 \Delta z_{m(i,j)} \end{bmatrix} - \frac{1}{3} \begin{bmatrix} \sum_{j=1}^3 \Delta r_{gs(k)} \\ \sum_{j=1}^3 \Delta \tau_{gs(k)} \\ 0 \end{bmatrix} \quad (2.32)$$

where

$$k = i + j \quad (k = k - 3 \text{ if } k > 3) \quad (2.33)$$

2.4.2 Extend three-rosette method for error separation (high sample density)

To increase the sample density of rotary positions, M was a multiple of N . In the following example, M was set to $3N$ while N was still equal to 3. Hence, the rosette tables turned to non-quadratic tables (Table 2.6, Table 2.7 and Table 2.8).

Table 2.6. Rosette table for the angular direction ($N = 3$ and $M = 3N$).

		Sphere		
		#1	#2	#3
Rotary position	#1	$\Delta\tau_{m(1,1)}$	$\Delta\tau_{m(1,2)}$	$\Delta\tau_{m(1,3)}$
	#2	$\Delta\tau_{m(2,1)}$	$\Delta\tau_{m(2,2)}$	$\Delta\tau_{m(2,3)}$
	#3	$\Delta\tau_{m(3,1)}$	$\Delta\tau_{m(3,2)}$	$\Delta\tau_{m(3,3)}$
	#4	$\Delta\tau_{m(4,1)}$	$\Delta\tau_{m(4,2)}$	$\Delta\tau_{m(4,3)}$
	#5	$\Delta\tau_{m(5,1)}$	$\Delta\tau_{m(5,2)}$	$\Delta\tau_{m(5,3)}$
	#6	$\Delta\tau_{m(6,1)}$	$\Delta\tau_{m(6,2)}$	$\Delta\tau_{m(6,3)}$
	#7	$\Delta\tau_{m(7,1)}$	$\Delta\tau_{m(7,2)}$	$\Delta\tau_{m(7,3)}$
	#8	$\Delta\tau_{m(8,1)}$	$\Delta\tau_{m(8,2)}$	$\Delta\tau_{m(8,3)}$
	#9	$\Delta\tau_{m(9,1)}$	$\Delta\tau_{m(9,2)}$	$\Delta\tau_{m(9,3)}$

Table 2.7. Rosette table for the radial direction ($N = 3$ and $M = 3N$).

		Sphere		
		#1	#2	#3
Rotary position	#1	$\Delta r_{m(1,1)}$	$\Delta r_{m(1,2)}$	$\Delta r_{m(1,3)}$
	#2	$\Delta r_{m(2,1)}$	$\Delta r_{m(2,2)}$	$\Delta r_{m(2,3)}$
	#3	$\Delta r_{m(3,1)}$	$\Delta r_{m(3,2)}$	$\Delta r_{m(3,3)}$
	#4	$\Delta r_{m(4,1)}$	$\Delta r_{m(4,2)}$	$\Delta r_{m(4,3)}$
	#5	$\Delta r_{m(5,1)}$	$\Delta r_{m(5,2)}$	$\Delta r_{m(5,3)}$
	#6	$\Delta r_{m(6,1)}$	$\Delta r_{m(6,2)}$	$\Delta r_{m(6,3)}$
	#7	$\Delta r_{m(7,1)}$	$\Delta r_{m(7,2)}$	$\Delta r_{m(7,3)}$
	#8	$\Delta r_{m(8,1)}$	$\Delta r_{m(8,2)}$	$\Delta r_{m(8,3)}$
	#9	$\Delta r_{m(9,1)}$	$\Delta r_{m(9,2)}$	$\Delta r_{m(9,3)}$

Table 2.8. Rosette table for the axial direction ($N = 3$ and $M = 3N$).

		Sphere		
		#1	#2	#3
Rotary position	#1	$\Delta z_{m(1,1)}$	$\Delta z_{m(1,2)}$	$\Delta z_{m(1,3)}$
	#2	$\Delta z_{m(2,1)}$	$\Delta z_{m(2,2)}$	$\Delta z_{m(2,3)}$
	#3	$\Delta z_{m(3,1)}$	$\Delta z_{m(3,2)}$	$\Delta z_{m(3,3)}$
	#4	$\Delta z_{m(4,1)}$	$\Delta z_{m(4,2)}$	$\Delta z_{m(4,3)}$
	#5	$\Delta z_{m(5,1)}$	$\Delta z_{m(5,2)}$	$\Delta z_{m(5,3)}$
	#6	$\Delta z_{m(6,1)}$	$\Delta z_{m(6,2)}$	$\Delta z_{m(6,3)}$
	#7	$\Delta z_{m(7,1)}$	$\Delta z_{m(7,2)}$	$\Delta z_{m(7,3)}$
	#8	$\Delta z_{m(8,1)}$	$\Delta z_{m(8,2)}$	$\Delta z_{m(8,3)}$
	#9	$\Delta z_{m(9,1)}$	$\Delta z_{m(9,2)}$	$\Delta z_{m(9,3)}$

To comply with the three-rosette method, 9 diagonals were defined and marked with different colors in Figure 2.11. Three cells for the k^{th} diagonal ($k = 1, 2, \dots, 9$) were corresponding to the three spheres measured at the k^{th} measuring position. For example, the (1st, 1st), (4th, 2nd) and (7th, 3rd) sphere centers in pink cells were measured at the 1st measuring position. The relationship of i, j and k was explained in Equation 2.11.

To separate the CMM deviations at 9 measuring positions, each table was further split into three 3×3 subtables, as shown in Figure 2.11. In subtable #1, all three spheres were measured at the #1, #4 and #7 rotary positions. It was same as calibrating the RT in steps of 120° . For better understanding, the orders #1, #4 and #7 in the subtable #1 can be replaced by #1, #2 and #3, which yielded Table 2.3. The CMM's angular deviations at three measuring positions were separated using the three-rosette method described in Section 2.4.1 (Equation 2.27, Equation 2.28 and Equation 2.29). The angular positioning deviations of the rotary table were calculated according to Equation 2.32. Alternatively,

data in the 9×3 tables can be processed directly to separate the CMM deviations and the error motions of RT, with clear understanding of the definition of measuring positions.

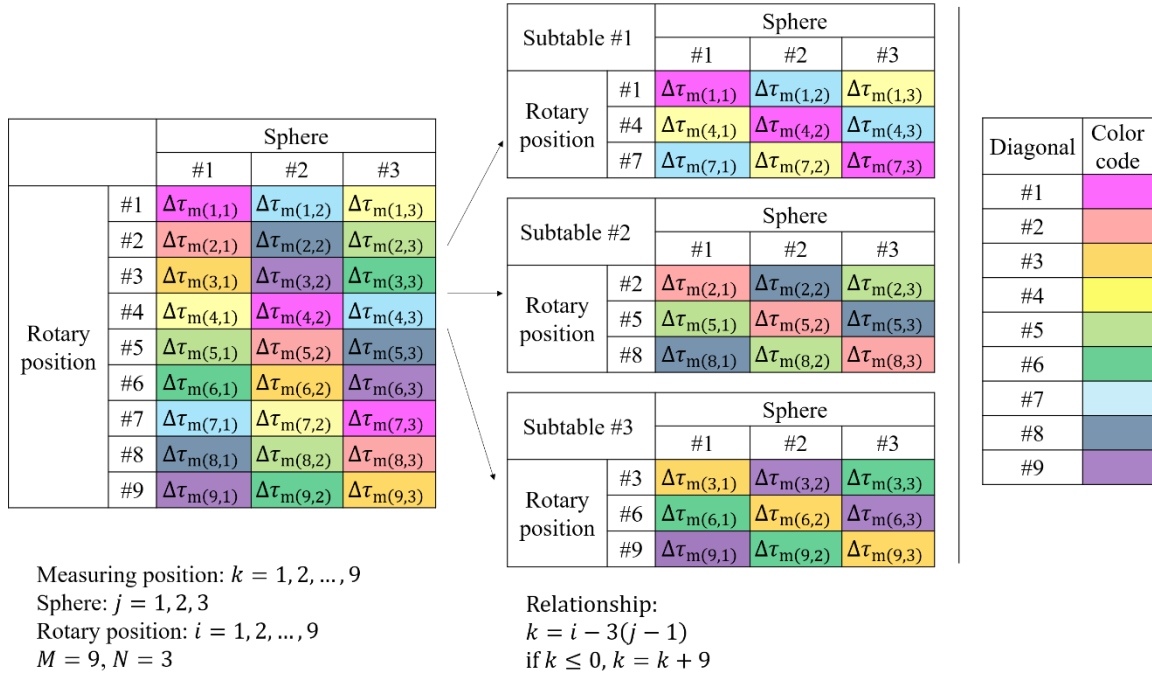


Figure 2.11. Rosette table ($N = 3$ and $M = 3N$) and its subtables for the angular direction, where the diagonals related to the measuring position k ($k = 1, 2, \dots, 9$) are marked with different colors.

2.4.3 A complete solution

In summary, the three-rosette method is a good starting point, because it compensates the $[\Delta P_{gs}]$ and calculates the ε_z and δ_z . Additional steps are needed to determine the δ_x , δ_y , ε_x and ε_y . An 11-step complete data processing procedure is given in Figure 2.12.

In the 3rd step of error separation phase in Figure 2.12, the compensated coordinates of sphere centers were translated back to the Cartesian CS. Then, a circle was approximated to the compensated coordinates of N sphere centers at every rotary position. Two methods

can be used to extract the frequency components of δ_x from the movement of artifact center in the x direction. The first method approximated a pre-defined trigonometric polynomial F_{sys} to the data. In Equation 2.34, the first order terms gave the eccentricity of the ball plate artifact, while the other terms denoted the coefficient of trigonometric terms for δ_x . Similarly, δ_y is separated. The second method was Fourier transformation from time domain to frequency domains.

$$F_{sys} = \sum_{m=1}^{N_1} [a_{m.c} \cos(m\theta) + a_{m.s} \sin(m\theta)] + \sum_{n=2}^{N_2} \left[a_{n.c} \cos\left(\frac{\theta}{n}\right) + a_{n.s} \sin\left(\frac{\theta}{n}\right) \right] \quad (2.34)$$

A plane was approximated to the compensated coordinates of N sphere centers at every rotary position. A similar approach was used to decouple the tilt error motions ε_x and ε_y from the tilt deviations of the artifact ε_{Ax} and ε_{Ay} .

For some RTs with ball bearings or roller bearings, the periods of error motions were not equal to integer cycles. In these cases, the Fourier transformation was used to extract the error motions of δ_x , δ_y , ε_x and ε_y .

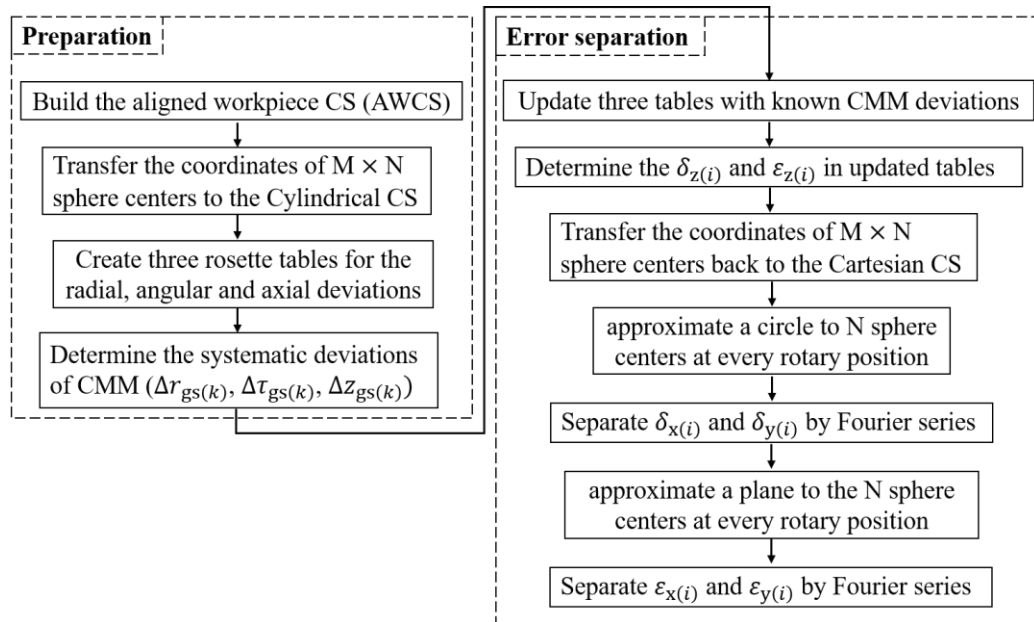


Figure 2.12. The complete error processing procedure.

2.4.4 Artifact calibration

The three-rosette method calculates the angular deviations of the spheres by averaging each column in Table 2.3. The radial deviations $\Delta r_{s(j)}$ and the axial deviations $\Delta z_{s(j)}$ were calculated in the same way in Table 2.4 and Table 2.5 (Equation 2.35). However, two sets of unknown values increased the calibration uncertainty: (i) the eccentricity of artifact $r_{H(j)}$ and $\varphi_{H(j)}$; (ii) the $\Delta r_{ct(i,j)}$ and $\Delta \theta_{ct(i,j)}$, both of which include $\delta_{x(i)}$ and $\delta_{y(i)}$. It may be confusing why $\sum_{i=1}^9 \Delta r_{ct(i,j)}$ and $\sum_{j=1}^9 \Delta \theta_{ct(i,j)}$ did not equal to zero. 2π periods of $\delta_{x(i)}$ yielded $\sum_{i=1}^9 \delta_{x(i)} = 0$. $\theta_{0(i)}$ also changed with the index of rotary position i that $\sum_{i=1}^9 \cos(\varphi_{0(j)} + \theta_{0(i)}) \times \delta_{x(i)} \neq 0$. The other accumulative results in Equation 2.36 also differed from zero. An applicable solution for the first issue is reducing the eccentricity down to 1 μm or less, using precision XY stage. The influence of the second issue may be reduced but not eliminated by using a high-end RT.

In comparison, the proposed solution determines $\delta_{x(i)}$, $\delta_{y(i)}$ and eccentricities H_x and H_y . Therefore, the deviation of spheres can be separated.

$$\begin{bmatrix} \Delta r_{s(j)} \\ \Delta \varphi_{(j)} \\ \Delta z_{s(j)} \end{bmatrix} = \frac{1}{9} \begin{bmatrix} \sum_{i=1}^9 \Delta r_{m(i,j)} \\ \sum_{i=1}^9 \Delta \tau_{m(i,j)} \\ \sum_{i=1}^9 \Delta z_{m(i,j)} \end{bmatrix} - \frac{1}{9} \begin{bmatrix} \sum_{k=1}^9 \Delta r_{gs(k)} \\ \sum_{k=1}^9 \Delta \tau_{gs(k)} \\ 0 \end{bmatrix} - \begin{bmatrix} r_{H(j)} \\ \varphi_{H(j)} \\ 0 \end{bmatrix} - \frac{1}{9} \begin{bmatrix} \sum_{i=1}^9 \Delta r_{ct(i,j)} \\ \sum_{i=1}^9 \Delta \theta_{ct(i,j)} \\ 0 \end{bmatrix} - \frac{1}{9} \begin{bmatrix} 0 \\ 0 \\ \sum_{i=1}^9 L(i,j) \end{bmatrix} \quad (2.35)$$

$$\frac{1}{9} \begin{bmatrix} \sum_{i=1}^9 \Delta r_{ct(i,j)} \\ \sum_{j=1}^9 \Delta \theta_{ct(i,j)} \end{bmatrix} = \frac{1}{9} \sum_{i=1}^9 \begin{bmatrix} \cos(\varphi_{0(j)} + \theta_{0(i)}) & \sin(\varphi_{0(j)} + \theta_{0(i)}) \\ \frac{-\sin(\varphi_{0(j)} + \theta_{0(i)})}{r_{so}} & \frac{\cos(\varphi_{0(j)} + \theta_{0(i)})}{r_{so}} \end{bmatrix} \begin{bmatrix} \delta_{x(i)} \\ \delta_{y(i)} \end{bmatrix} \neq \begin{bmatrix} 0 \\ 0 \end{bmatrix} \quad (2.36)$$

CHAPTER 3: NUMERICAL SIMULATION

The proposed method was validated via numerical simulations. Simulation inputs were generated via two ways: (i) proper assumptions based on product sheets and experience (ii) experimental data.

3.1 Simulation input

3.1.1 Simulation input: circular ball plate (CBP) artifact

The number of spheres N was set as 6. Unavoidably, spheres had position deviations due to imperfect fabrication and assembly of artifact. Günther et al. [52] reported a circular ball plate (CBP) with radial, pitch and z deviations within $[-20, 20] \mu\text{m}$. In this simulation, the radial and pitch deviations were randomly selected within $[-50, 50] \mu\text{m}$, and z deviations were randomly selected within $[-20, 20] \mu\text{m}$.

The radius r_{s0} was set as 100 mm. Several factors affected the tilt deviations of the artifact, including the tilt of RT surface, fabrication accuracy of the base plate, assembly of the artifact, base plate distortion resulted from the clamping force and weight. The ranges of tilt deviation and eccentricity of artifact are given in Table 3.1.

Table 3.1. Parameter setting for the artifact.

	Parameter	Range	Distribution	
Spheres	Number N	6	-	
	Radial deviation Δr_s	$[-50, 50] \mu\text{m}$	Rectangular	
	Pitch deviation	$[-50, 50] \mu\text{m}$	Rectangular	
	Axial deviation Δz_s	$[-20, 20] \mu\text{m}$	Rectangular	
Artifact	Radius r_{s0}	100 mm	-	
	Eccentricity	H_x	$[-100, 100] \mu\text{m}$	Rectangular
		H_y	$[-100, 100] \mu\text{m}$	Rectangular
	Tilt	ε_{Ax}	$[-20, 20] "$	Rectangular
		ε_{Ay}	$[-20, 20] "$	Rectangular

3.1.2 Simulation input: RT

The systematic components of the error motions were simulated with polynomial functions $F_{\text{input,sys}}$ (Equation 3.1). T_s was the defined period of signal. The constants $a_{m,c}$ and $a_{m,s}$ were randomly selected within $[-1, 1]$ at every new iteration. $w_{m,c}$ and $w_{m,s}$ were the weight factors, which decreased linearly, while the degrees increased (Equation 3.2). M_1 and M_2 were constants defining the minimum and maximum degrees of trigonometric polynomial. M_1 was set as 1 for δ_z and ε_z , while it equaled to 2 for the other error motions. M_2 was the smaller value of 10 and $N - 1$, where N denoted the number of spheres.

$$F_{\text{input,sys}} = \sum_{m=M_1}^{M_2} \left[a_{m,c} w_{m,c} \cos\left(\frac{2\pi m \theta}{T_s}\right) + a_{m,s} w_{m,s} \sin\left(\frac{2\pi m \theta}{T_s}\right) \right] \quad (3.1)$$

$$w_{m,c} = w_{m,s} = 1 - \frac{m - M_1}{M_2} \quad (3.2)$$

The maximum absolute values of the translational terms and rotational terms were normalized to $1 \mu\text{m}$ and 1 arc second , respectively.

Non-repeatable components of the simulation input $F_{\text{input,sys}}$ followed normal distribution, with standard deviations defined as 2% of the peak amplitudes of the

corresponding systematic components. Table 3.2 summarizes the parameter setting for RT error motions. Figure 3.1 shows an example for the simulation input of a translational term.

Table 3.2. Parameter setting for the RT error motions.

Error motions	Systematic components			Random components
	M_1	M_2	Normalized amplitude of curve	Standard deviation
δ_x	1	Min (10, N - 1)	1.00 μm	0.02 μm
δ_y	1			
δ_z	2			
ε_x	1		1.00 "	0.02 "
ε_y	1			
ε_z	2			

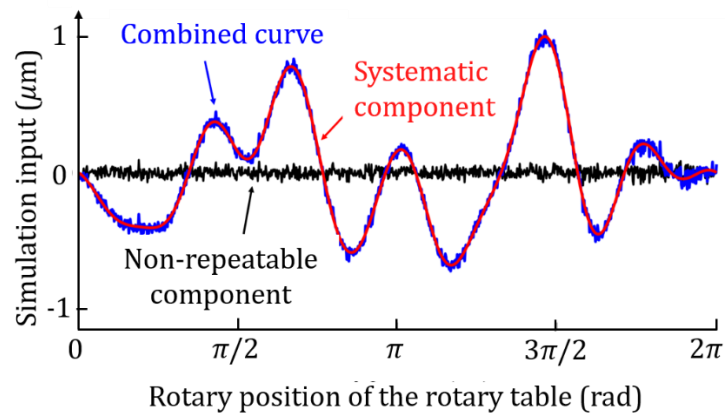


Figure 3.1. Example of simulation input for a translational term.

3.1.3 Simulation input: coordinate measuring machine (CMM)

3.1.3.1 Probing error

The coordinates of probed points on the sphere were defined as (ρ, α, β) in the spherical CS (Figure 3.2(a)). α denoted the azimuthal angle in the XY plane starting from

the x-axis, while β denoted the polar angle starting from the positive z-axis. Because a vertical probe can only reach the upper hemisphere, the range of β was limited to $[0, \pi/2]$.

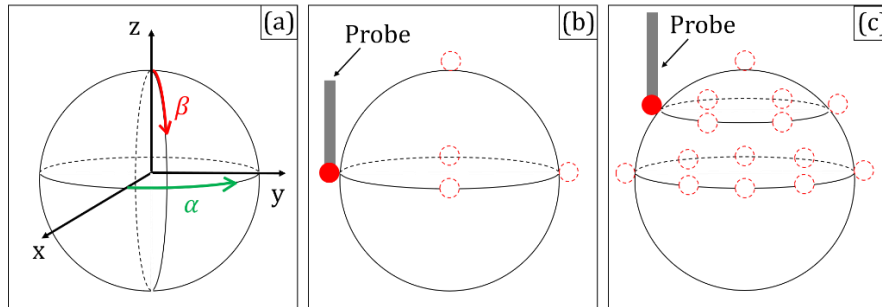


Figure 3.2. Probing strategy: (a) Spherical coordinate system (b) point distribution of 5-point probing strategy (c) point distribution of 15-point probing strategy.

Commercial CMM software like Quindos usually provided multiple default probing strategies, with point numbers ranging from 5 to several hundred. The points were split into several layers with different β , and points in each layer were evenly distributed. The number of points in one layer increased with β , in order to cover larger perimeter. A probing strategy achieving an acceptable uncertainty at a low number of points should be chosen. In this experiment, 5-point and 15-point strategies were tested on a Leitz PMM-F, using a 80 mm reference probe, whose tip diameter is 5 mm. Positions of probed points for each sampling strategy are demonstrated in Figure 3.2 (b) and (c). Table 3.3 and Table 3.4 report the probing deviations for each strategy, respectively, based on 50 repetitions.

Table 3.3. Probing deviations for 5-point probing strategy. (Leitz PMM-F, 80 mm length reference probe, 5 mm probe tip diameter).

No. of point	α	β	Mean dev. (μm)	Standard dev. (μm)
1	0	0	0.0008	0.0020
2	90	90	-0.0428	0.0050
3	180	90	0.0377	0.0044
4	270	90	-0.0377	0.0047
5	0	90	0.0419	0.0052

Table 3.4. Probing deviations for 15-point probing strategy. (Leitz PMM-C, 80 mm reference probe, 5 mm probe tip diameter, severe drift of the sphere center observed ($x = 1 \mu\text{m}$, $y = 1.5 \mu\text{m}$ and $z = 0.6 \mu\text{m}$)).

No. of point	α	β	Mean dev. (μm)	Standard dev. (μm)
1	0	0	-0.2062	0.0127
2	0	45	0.2164	0.0143
3	60	45	-0.1641	0.0215
4	120	45	-0.0064	0.0182
5	180	45	-0.0958	0.0177
6	240	45	0.1284	0.0215
7	300	45	0.2146	0.0160
8	0	90	-0.2738	0.0180
9	45	90	0.0982	0.0286
10	90	90	-0.3087	0.0624
11	135	90	0.4222	0.0249
12	180	90	0.1048	0.0250
13	225	90	-0.2225	0.0276
14	270	90	-0.0836	0.0506
15	315	90	0.1766	0.0407

3.1.3.2 Geometric deviations

The CMM geometric deviations were defined in the following way. The systematic deviation component $\Delta P_{gs(k)}$ was randomly selected within the following range: $0.5 \times [-E_{L,MPE} + R_{0,MPL}, E_{L,MPE} - R_{0,MPL}]$. $E_{L,MPE}$ denoted the maximum permissible error for length measurement [55]. $R_{0,MPL}$ denoted the maximum permissible limit of the repeatability range of the length measurement error. $L_x(k)$ and $L_y(k)$ were the maximum x

and y systematic geometric deviation components for the k^{th} measuring position (Equation 3.3). ξ denoted the azimuthal angle in the XY plane.

$$\begin{bmatrix} L_{x(k)} \\ L_{y(k)} \end{bmatrix} = |E_{L,MPE} - R_{0,MPL}| \begin{bmatrix} \cos \xi_k \\ \sin \xi_k \end{bmatrix} \quad (3.3)$$

Two strategies were used to generate the random components of geometric deviations. The first strategy used experimental data of the ball step gage (BSG) test. The reported standard deviations of Δx_{gr} , Δy_{gr} and Δz_{gr} were within $[0.02, 0.06] \mu\text{m}$. In the second strategy, the Δx_{gr} , Δy_{gr} and Δz_{gr} had the same standard deviations, which were denoted by σ_{gr} . In a similar way, σ_{pr} denoted the standard deviations of the random probing error in each of the three axes, i.e., $\sigma_{\text{pr}} = \sigma_{\text{pr},x} = \sigma_{\text{pr},y} = \sigma_{\text{pr},z}$. σ_{gr} and σ_{pr} were set to $0.05 \mu\text{m}$. The parameter setting is summarized in Table 3.5.

Table 3.5. Parameter setting for CMM deviations.

Parameter	Range	Distribution
$\Delta x_{\text{gr}(i,j)}$	$\mu_{\text{gr}} = 0, \sigma_{\text{gr}} = 0.05 \mu\text{m}$	Gaussian
$\Delta y_{\text{gr}(i,j)}$		
$\Delta z_{\text{gr}(i,j)}$		
$\Delta x_{\text{pr}(i,j)}$	$\mu_{\text{pr}} = 0, \sigma_{\text{pr}} = 0.05 \mu\text{m}$	Gaussian
$\Delta y_{\text{pr}(i,j)}$		
$\Delta z_{\text{pr}(i,j)}$		
$\Delta x_{\text{gs}(k)}$	$L_{x(k)} \times [-0.5, 0.5]$	Rectangular
$\Delta y_{\text{gs}(k)}$	$L_{x(k)} \times [-0.5, 0.5]$	Rectangular
$\Delta z_{\text{gs}(k)}$	$[-0.3, 0.3] \mu\text{m}$	Rectangular
Δx_{ps}	$[-0.5, 0.5] \mu\text{m}$	Rectangular
Δy_{ps}	$[-0.5, 0.5] \mu\text{m}$	Rectangular
Δz_{ps}	$[-0.5, 0.5] \mu\text{m}$	Rectangular

3.2. Simulation results

The angular step of rotary table was 7.5° ($M = 48$) and the number of repeated cycles was 4. Since the CBP had 6 spheres, the maximum degrees of error motions M_2 were set to 5 according to Table 3.2.

As discussed in Section 2.3, the coordinates of the j^{th} sphere center at the i^{th} rotary position in the FCS were expressed by Equation 2.6. The simulated inputs defined in Section 3.1 were used to generate the sphere centers at each rotary position. Therefore, the point cloud of 1152 sphere centers were processed using the method fully described in Section 2.4.2 to extract the error motions of rotary tables, as well as the deviations of artifact and the systematic geometric deviations of the CMM. Fourier transformation was used to extract the error motions of δ_x , δ_y , ε_x and ε_y .

3.2.1 Error motions

In the first simulation, the periods of all six error motions were set to 2π . In Figure 3.3 (a) – (f), the squares represent the simulation inputs provided to the simulator. The solid dots represents the simulation outputs, which means the error motions of rotary table separated from the point cloud of sphere centers using the proposed method. The separated error motions matched the corresponding input error motions.

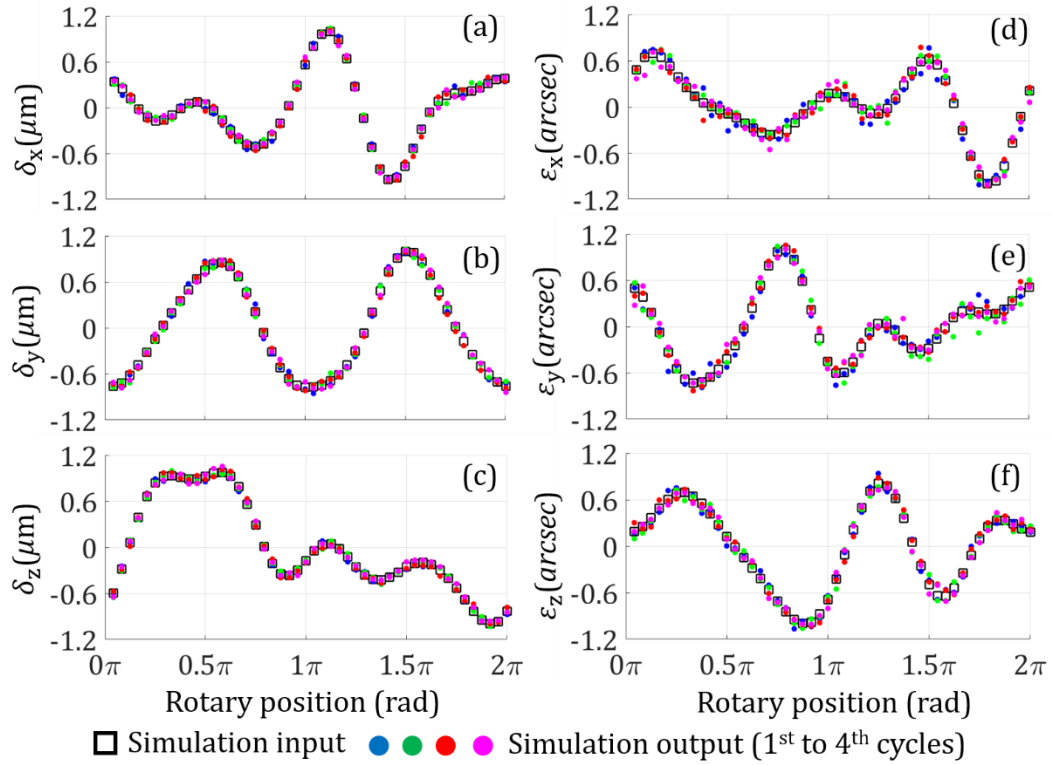


Figure 3.3. Simulation inputs and outputs of the RT error motions (periods = 2π): (a) δ_x (b) δ_y (c) δ_z (d) ε_x (e) ε_y (f) ε_z .

In the next three tests, the periods of error motions were set as 1.56π , 2.72π and 4.18π . Figure 3.4 shows the inputs and outputs of δ_x in three cases. Longer period needed more angular positions to cover the whole range. In the third case (Figure 3.4(c)), the period of error motions were set to 4.18π , which covered less than two times ($8\pi / 4.18\pi < 2$). Although the error motions were still successfully separated, increasing the number of cycles M to 6 or more can reduce the uncertainty.

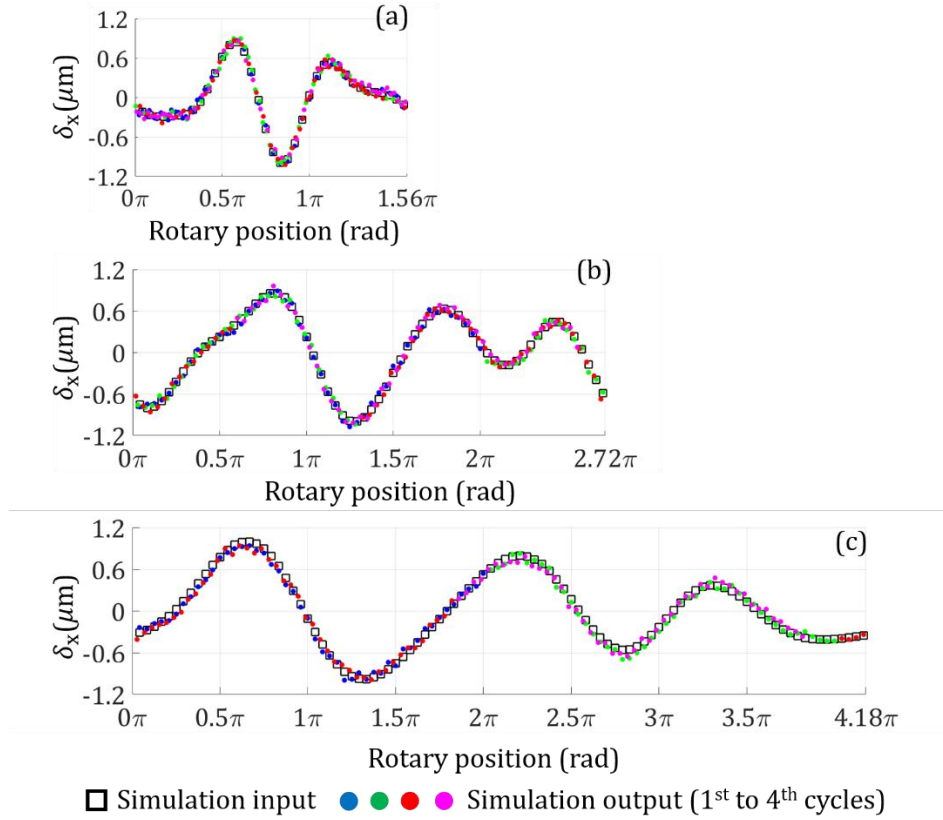


Figure 3.4. Simulation inputs and outputs of the δ_x deviation whose period did not equal to 2π : (a) 1.56π (b) 2.72π (c) 4.18π .

Figure 3.5 gives two examples of input and output frequency components of δ_x , which were detected by Fourier transformation. $T_{s(m)}$ is the period of the m^{th} frequency component.

$$T_{s(m)} = \frac{T_s}{m} \quad (3.4)$$

For the δ_x deviation, the minimum degree of polynomial M_1 was set to 2. The $m = 1$ component in Figure 3.5 was corresponding to the eccentricity of artifact. In both cases, the frequency components were successfully detected.

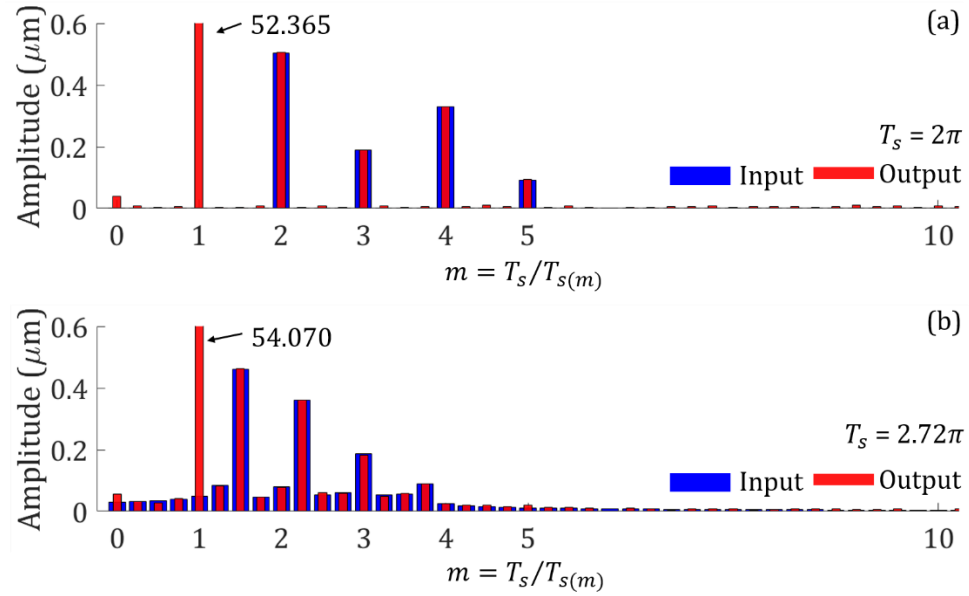


Figure 3.5. Frequency components of input and output δ_x deviation with number of cycle 4 and cycle period: (a) $T_s = 2\pi$ (b) $T_s = 2.72\pi$.

3.2.2 CMM deviations

As shown in Figure 3.6, the CMM's systematic geometric deviations at 48 measuring positions were separated. The output values matched input values. The residuals mainly resulted from the CMM's non-repeatable geometric deviations $\Delta p_{gr(i,j)}$ and non-repeatable probing deviations $\Delta p_{pr(i,j)}$.

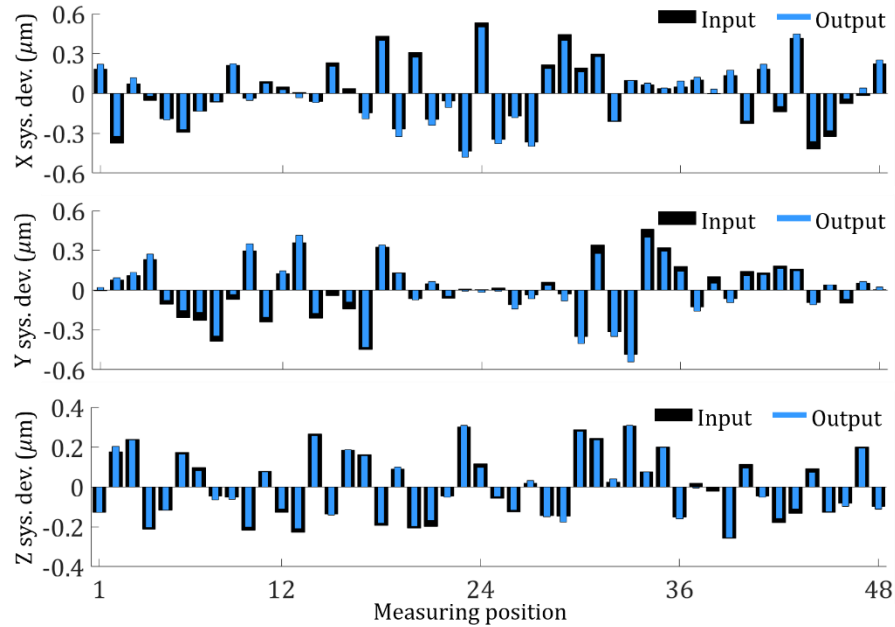


Figure 3.6. Inputs and outputs of CMM's systematic geometric deviations.

3.2.3 Artifact deviations

As experimental data will show in Chapter 4, compared with its nominal position, each sphere usually showed a two-digit micrometer deviation. This primarily resulted from two groups of sources: (i) imperfect fabrication of base plate and assembly of the artifact; (ii) clamping force and imperfect centering of the artifact. Deviations of the first type can be pre-determined by using a more accurate measuring device. Deviations of the second type can only be determined in situ, but even a high-end 3-axis CMM is not sufficient to accomplish the second task alone. The three-rosette method [49] is a good option, since the CMM's systematic deviations are neutralized. The proposed solution in Section 2.4 also decoupled the eccentricity of the artifact (Table 3.6) from the radial and angular position deviations of spheres. Therefore, a very precise centering of the artifact was not necessary.

Table 3.6. Simulated deviations of the ball plate artefact.

Deviation	Parameter	Input	Output	Residual
Eccentricity	H_x	24.000 μm	23.996 μm	-0.004 μm
	H_y	-18.000 μm	-17.992 μm	0.008 μm
Tilt	ε_{Ax}	1.023"	1.017"	-0.006"
	ε_{Ay}	6.460"	6.461"	0.001"

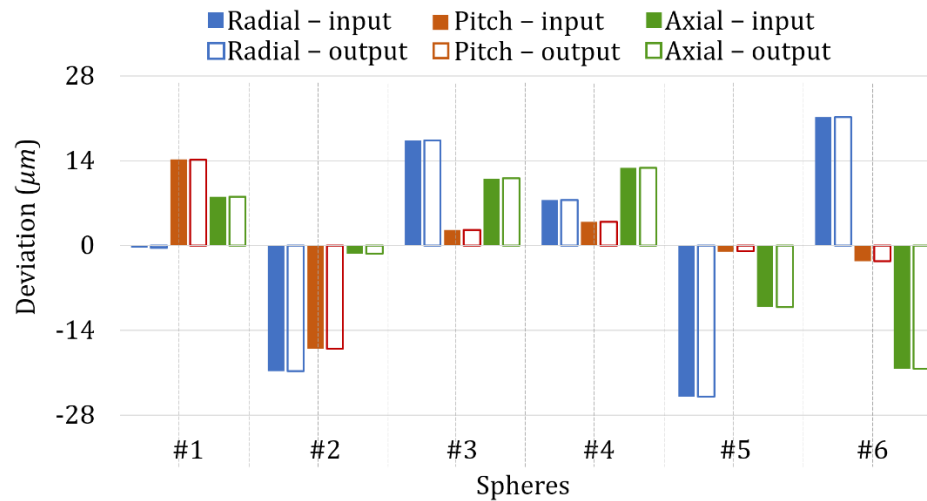


Figure 3.7. Simulation inputs and outputs of the spheres' position deviations.

3.3 Key factors

This section discusses the influences of some parameters. In each case, the ranges and distributions of all the parameters, except the targeted parameter, were the same as in Section 3.1. Four parameters were investigated independently: (1) ball plate radius r_{s0} ; (2) number of spheres N ; (3) number of measuring positions M ; (4) CMM's random deviations. In every of 500 repetitions, all the parameters values were regenerated, as well as the patterns of error motions and CMM deviations. The maximum absolute residual $|E_{\max}|$ between the sampled input and output values was recorded.

3.3.1 Ball plate radius r_{s0}

The r_{s0} was increased from 50 mm to 400 mm, in a step of 5 mm. Figure 3.8 shows the average values $\mu_{|E_{\max}|}$ and $\mu_{|E_{\max}|} \pm 3\sigma_{|E_{\max}|}$ range of 500 repetitions performed at each r_{s0} . In Figure 3.8 (a) to (c), the three curves were horizontal with small variations. Namely, increasing r_{s0} had negligible influence on δ_x , δ_y and δ_z .

In (d) to (f), the three curves decreased fast between 50 mm and 200 mm and the decreasing rate slowed down after 200 mm. The band width, which was equal to the difference between the $\mu_{|E_{\max}|} + 3\sigma_{|E_{\max}|}$ and $\mu_{|E_{\max}|} - 3\sigma_{|E_{\max}|}$ curves, decreased in a similar trend.

For ε_x , ε_y and ε_z , the uncertainty sources from the CMM's random deviations $\Delta P_{gr}/r_{s0}$ and $\Delta P_{pr}/r_{s0}$ decreased when r_{s0} increased, which effectively reduced the residuals and uncertainties. However, the drawback of increasing r_{s0} is dominating, because the artifact is, less portable, and more expensive. Common values are chosen between 100 mm and 200 mm.

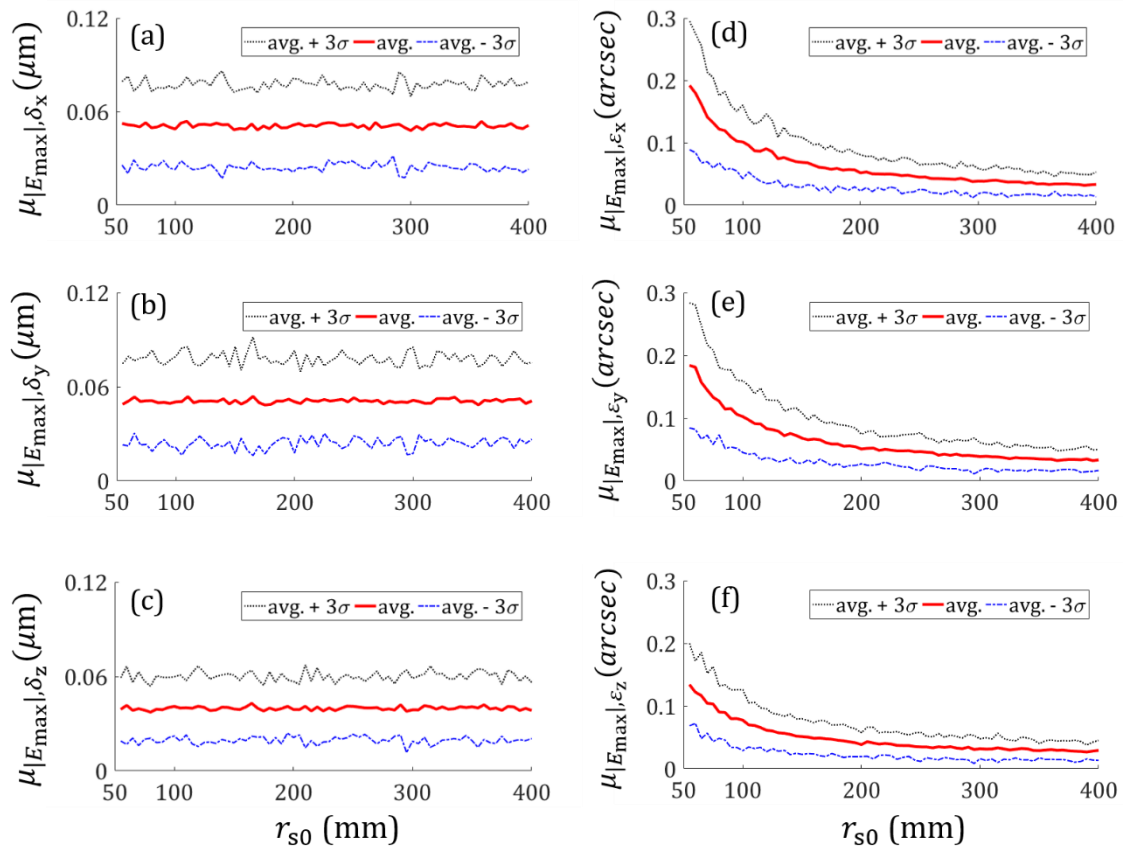


Figure 3.8. $\mu_{|E_{max}|}$ and $\mu_{|E_{max}|} \pm 3\sigma_{|E_{max}|}$ ranges between the sampled input and output values, when the r_{s0} increased from 50 mm to 400 mm: (a) δ_x (b) δ_y (c) δ_z (d) ϵ_x (e) ϵ_y (f) ϵ_z .

3.3.2 Number of spheres N and number of measuring positions M

As discussed in Section 2, the number of measuring positions M was a multiple of N . Since the highest degree of error motions was 5, the lower limit of N was set as 6. The upper limit was set to 48.

In Figure 3.9(a), the $\mu_{|E_{max}|, \delta_x}$ at $N = 6$ was 50 nm. This value was reduced by 20% (10 nm) and 32% (16 nm), when N was doubled and quadrupled, respectively. Similarly, the $\mu_{|E_{max}|, \epsilon_x}$ in Figure 3.9(d) was reduced by 23.1% (0.022 ") and 41.8% (0.042 "), respectively. Increasing the number of spheres helps neutralize the

nonrepeatable deviations of CMM ΔP_{gr} and ΔP_{pr} . However, these improvements were at the expense of doubling and quadrupling the total measurement time, which was not very reasonable considering the very low absolute values. The major concern for selection of the lowest acceptable N is to ensure that all significant frequency components are included. Therefore, a preliminary test with high N and low M values was carried out to determine the acceptable N .

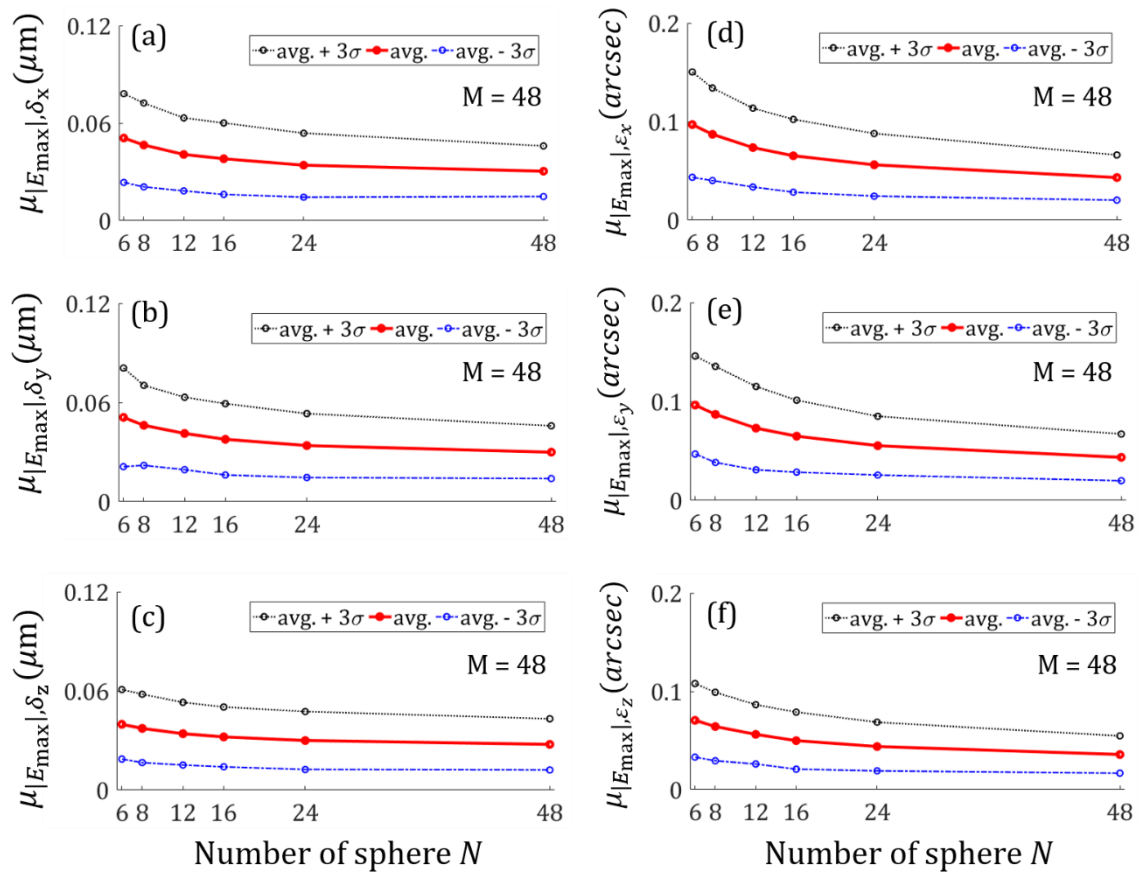


Figure 3.9. $\mu_{|E_{max}|}$ and $\mu_{|E_{max}|} \pm 3\sigma_{|E_{max}|}$ ranges of between the sampled input and output values, when N was increased from 6 to 48: (a) δ_x (b) δ_y (c) δ_z (d) ϵ_x (e) ϵ_y (f) ϵ_z .

Smaller angular steps improve the sample density to approximate the error motions, at the expense of longer measurement time. Since there is no a universal standard for M , preliminary test can help find the proper value.

3.3.3 CMM's random deviations

CMM measurements are affected by two random deviations denoted by ΔP_{gr} and ΔP_{pr} . Apparently, they have the same effects on the separated error motions according to Equation 2.12. Therefore, only the ΔP_{gr} was studied in this test. σ_{gr} was increased from 0.02 μm to 0.2 μm , where 0.05 μm was the value for standard case (see Figure 3.10). $\mu_{|E_{\max}|}$ and $\sigma_{|E_{\max}|}$ increased linearly with σ_{gr} , which showed that the random deviations are major uncertainty resources to the results.

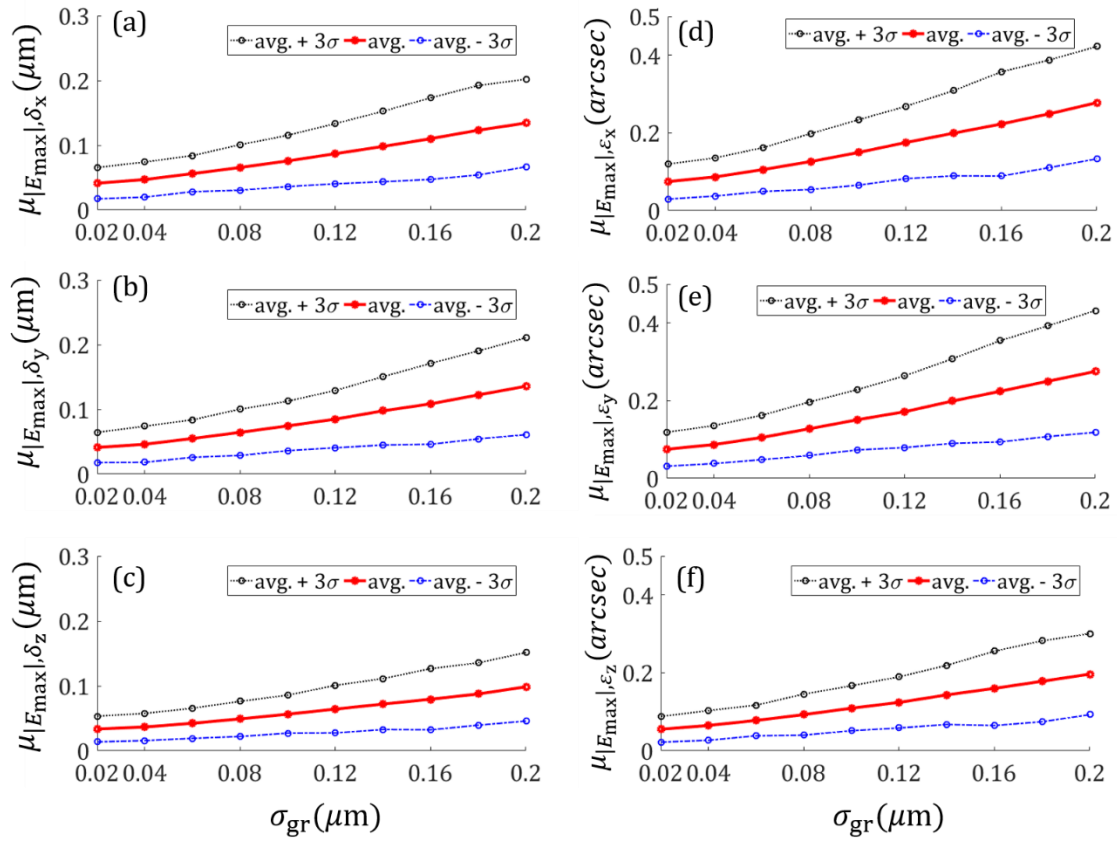


Figure 3.10. $\mu_{|E_{max}|}$ and $\mu_{|E_{max}|} \pm 3\sigma_{|E_{max}|}$ ranges of between the sampled input and output values, when σ_{gr} was increased from 0.02 to 0.2: (a) δ_x (b) δ_y (c) δ_z (d) ε_x (e) ε_y (f) ε_z .

3.4 CMM drift

3.4.1 Drift test of CMM and workpiece

A $\varnothing 400$ mm 12-sphere CBP artifact was built (Section 4.1). The artifact was fixed on the static RT (Figure 4.8). The CMM repeatedly measured the coordinates of all spheres over 20 hours in a drift test. 12 temperature sensors in the CMM guideways and one sensor near the artefact reported less than 0.1°C temperature variation.

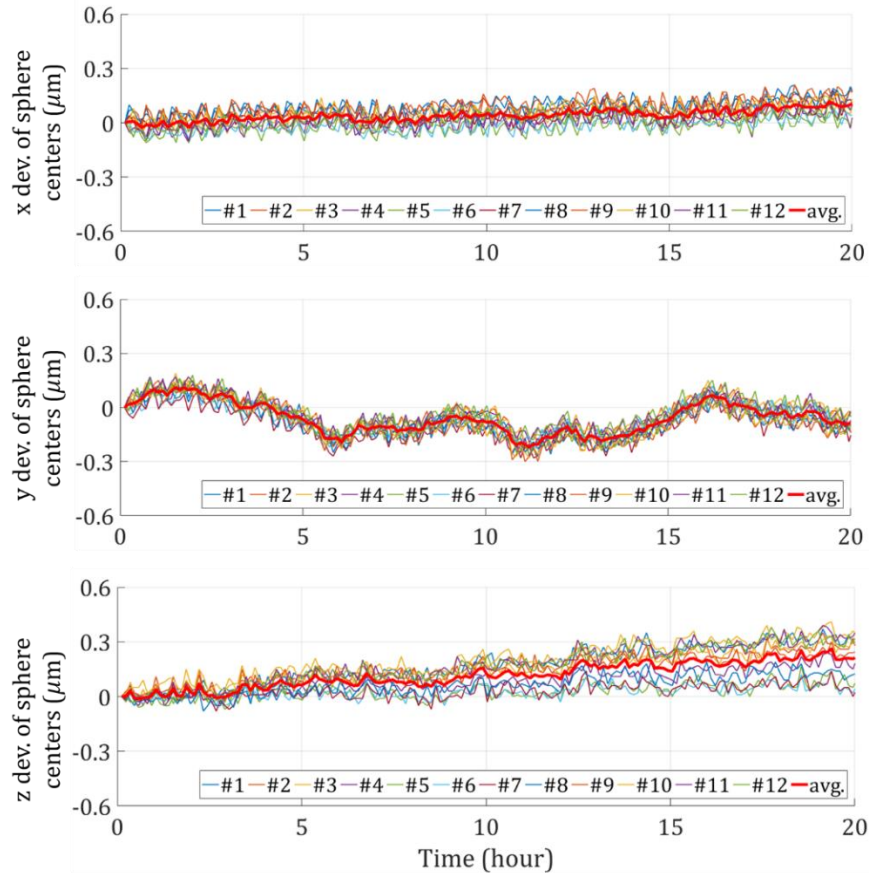


Figure 3.11. Deviations of sphere centers along three axes in 20-hour drift: (a) x deviations (b) y deviations (c) z deviations.

As shown in the Figure 3.11(b), the deviations of 12 sphere centers had same trends in the y direction. Moreover, the deviations of sphere centers were stable in the x direction (Figure 3.11(a)). These results indicated low thermal expansion of the base plate in radial directions. Position variations reflected a drift of the CMM. The y-axis showed more drift than the x-axis, because the y-axis was parallel to the traveling beam in this gantry-type CMM. In Figure 3.11(c), 12 spheres had various drifts between $0.05 \mu\text{m}$ and $0.3 \mu\text{m}$. It is possible that the glue was not fully cured when the drift test was conducted. The mean deviations of the 12 spheres (red curves) was regarded as the CMM drift along the three axes.

In sample experiments, a 6-sphere circular ball plate was used as the artifact. In common case, the rotary table was calibrated for 4 cycles in a step of 7.5° . At each rotary position, the CMM probed 5 points on each of 6 spheres. It cost 4 hours to finish the measurement.

CMM real time drift is unpredictable and cannot be compensated. Therefore, a stable CMM is always desired. To understand the influence of CMM drift, acquired drift data was fed into the simulator.

3.4.2 Influence of CMM's drift

In each repetition, 4-hour continuous drift data in Figure 3.11 was fed to the simulator. The begin time was randomly picked between the 0th and 17th hour. This numerical simulation was repeated for 500 times.

$\mu_{|E_{\max}|}$ and $\sigma_{|E_{\max}|}$ of all error motions were at the same levels of the default case, which showed that the tested CMM drift has an acceptably low influence on the results.

Multiple sources may lead to higher CMM drift, including using a middle-class or low-cost CMM, lower grade of environment control, thermal control issues of motors and mechanical structures due to long-time continuous movement. For investigation, the amplitudes of the acquired drift data were amplified with an amplification factor, where the factor for the original data equaled to 1. As shown in Figure 3.12, the $\mu_{|E_{\max}|}$ of error motions increased linearly with the amplification factor, at a low rate. When the amplification factor was set to 3, the results of $\mu_{|E_{\max}|} \approx 0.1 \mu\text{m}$ for translational terms and $\mu_{|E_{\max}|} \in [0.15, 0.22]$ arcsec for rotational terms were still acceptable.

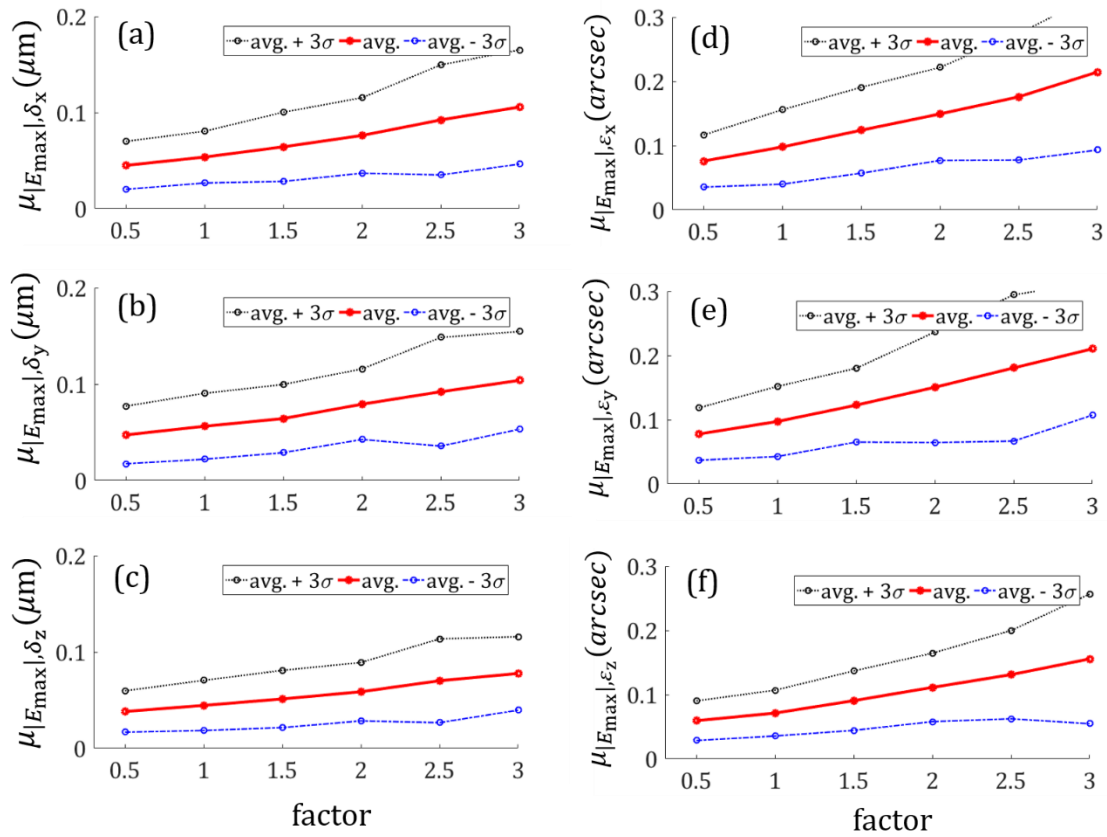


Figure 3.12. $\mu_{|E_{max}|}$ and $\mu_{|E_{max}|} \pm 3\sigma_{|E_{max}|}$ ranges between the sampled input and output values, when the amplification factor of CMM drift increased from 0.5 to 3: (a) δ_x (b) δ_y (c) δ_z (d) ε_x (e) ε_y (f) ε_z .

CHAPTER 4: EXPERIMENTS

The purpose of this chapter is to validate the proposed error separation solution experimentally. The separated CMM deviations were compared with experimental results from a ball step gage (BSG). The separated error motions were compared with results from a spindle error analyzer (SEA).

4.1 CBP artifact

4.1.1 Design of a CBP artifact

Both Physikalisch-Technische Bundesanstalt (PTB) and Hexagon Manufacturing Intelligence, Germany (HMI) built single layer circular ball plate (CBP) artifacts [52]. The one made by HMI was 50% smaller to achieve higher portability (\varnothing 200 mm vs. \varnothing 400 mm). PTB's artifact used twelve ceramic spheres, while HMI's artifact had a mixture of six ceramic spheres and six tungsten carbide spheres (Figure 4.1). Tungsten carbide spheres were suitable for HP-O optical sensor, which is based on frequency-modulated interferometric optical distance measurement. The spheres were glued to countersinks on the base plate.

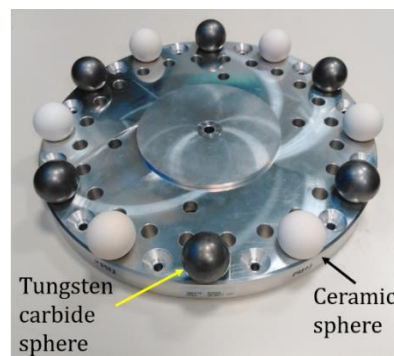


Figure 4.1. A CBP artifact made by Hexagon Manufacturing Intelligence, Germany.

To secure the artifact on the RT, clamping force was applied directly on the base plate. The resulting distortion might cause a considerable amount of time to reach an equilibrium status. More importantly, it changed the relative z coordinates of all the sphere.

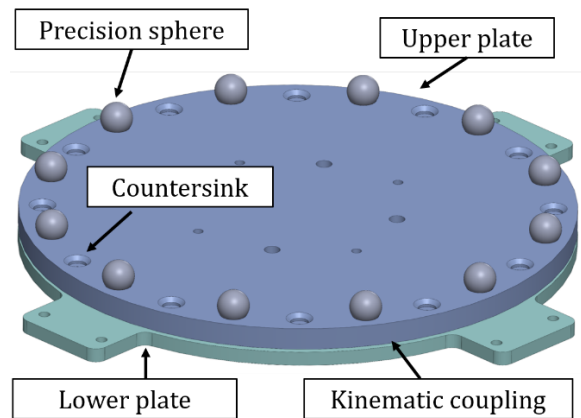


Figure 4.2. Schematic of double plate artifact.

In this study, a double layer configuration for the CBP was proposed by absorbing the advantages of the above ones (Figure 4.2). The lower plate functioned as a sacrificing layer to isolate clamping forces away from the primary artifact (upper plate). Therefore, the upper plate was freed from distortion. A Maxwell style kinematic coupling between the upper and lower plates constrained the upper plate's six degrees of freedom. Instead of adding additional vee blocks, v-grooves were directly machined into the lower plate to reduce the overall height. The outer cylindrical surface assisted the centering of the lower plate. Kinematic coupling also enabled an efficient removal and installation of the upper plate, which was critical to protect the artifact at manipulating the loads on the table.

To achieve minimum deflection of the upper plate with three-point support configuration, the radial positions of support points were 65% of the radius of plate [56].

Therefore, the radial positions of the three 12.7 mm diameter spheres for kinematic mount were set as 140 mm from the center of upper plate (Figure 4.3).

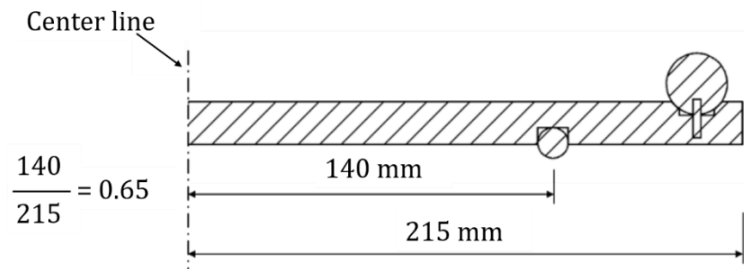


Figure 4.3. Least deformation of top plate.

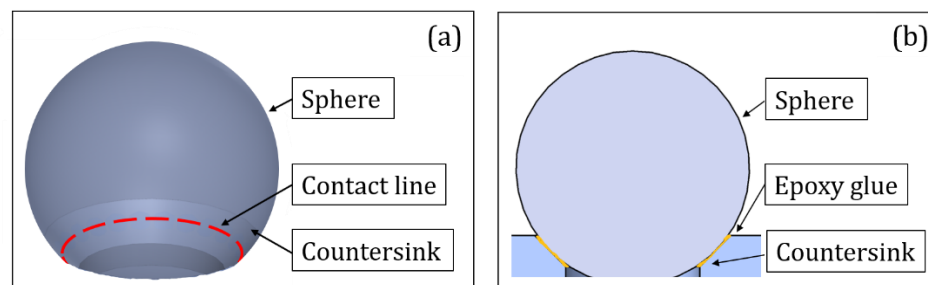


Figure 4.4. Fixing a sphere on the base plate: (a) schematic of circular contact line between the sphere and countersink (b) epoxy glue applied between the sphere and the surface of countersink.

The designed CBP had 12 spheres evenly distributed in a circular pattern. Using a relatively large diameter of $\varnothing 400$ mm helped to reduce uncertainties of calculated tilt error motions and angular positioning deviations resulting from the CMM, as discussed in Chapter 3.

Countersinks assisted the precise positioning of spheres at installation. Ideally, the contact area between a sphere and a countersink was a circle (Figure 4.4(a)). However, if glue was applied to the surface of the countersink for fixture purpose (Figure 4.4(b)), it was unavoidable that the glue thickness between the sphere and countersink at the contact zone

was uneven. Moreover, if it were necessary, it would be difficult to remove and reinstall the sphere without fully cleaning up the glue residual on the countersink.

To solve this problem, 0.3mm gaps were left between the bottom of spheres and the bottom surfaces of countersinks. Proper amount of epoxy glue filled the gap to fix the spheres, so that the circular contact lines between spheres and countersinks remained clean (Figure 4.5(a)). If complete spheres were used, they may be knocked off accidentally by horizontal forces, because they were secured on the plate only with thin layers of glue. For this artifact, 25.4 mm diameter grade 3 spheres with 3.175 mm diameter pin holes were used. Grade 3 sphere had allowable diameter variation of 76.2 nm, allowable form deviation of 76.2 nm and allowable surface roughness of 12.7 nm. By drilling the same size pin holes at the bottom of the countersinks, the spheres were fixed to the base plate firmly with short pins and epoxy glue. In Figure 4.5(b), the three spheres for kinematic coupling was glued to the three 12.7 mm diameter, 7 mm deep holes, respectively. The sphere can also be secured in the hole within press fit, which is one kind of fastening between two parts that the inner component is larger than outer component.

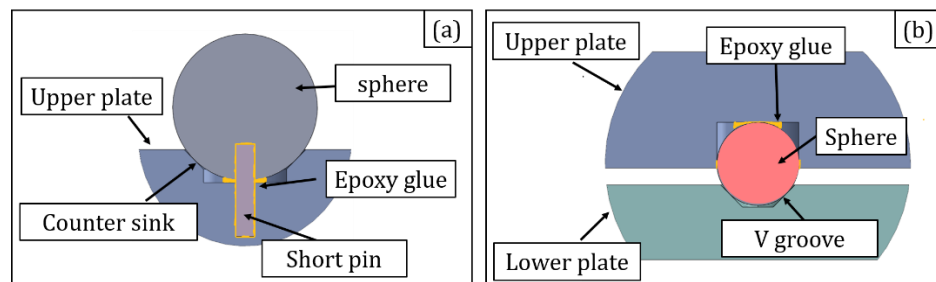


Figure 4.5. Illustration of assembly details: (a) fixturing a precision sphere on the countersink (b) Maxwell kinematic coupling between two plates.

4.1.2 Fabrication and stability test of the artifact

6061 Aluminum was chosen as the material for the base plates. It had the advantage of light weight, low cost and easy-to-machine. On the other hand, the major shortcoming was the relatively high coefficient of thermal expansion (CTE) at $23.4 \times 10^{-6}/^{\circ}\text{C}$ (ppm/ $^{\circ}\text{C}$). Common grades of Invar (36% nickel and 64% iron) have a very low CTE of around 1.2 ppm/ $^{\circ}\text{C}$, which makes Invar the ideal material for artifacts. However, the price of Invar is much higher than aluminum or steel.

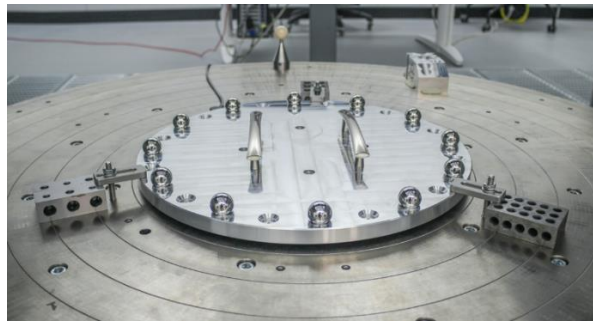


Figure 4.6. Upper plate clamped on the RT for stability test

Once the aluminum base plate for the upper plate had been machined on a Mori Seiki CNC machine, 12 spheres were secured on the plate as discussed before. At the 52nd hour after assembling, the upper plate was secured on the RT to check the stress release of the aluminum plate and the curing progress of epoxy glue. The coordinate of all the spheres were measured continuously for 16.8 hours, when the table was at stationary condition (Figure 4.6). Figure 4.7(a) demonstrates the position change of each sphere in the z direction, compared to its initial position. All the spheres drifted upwards in the first two hours, and then drifted downwards continuously in the rest of time. Figure 4.7(b) shows the differences between the final and initial heights. Except the spheres #10 and #11,

all spheres moved downwards. The whole plate tilted from sphere #10 and #11 towards sphere #6. It probably reflects that the 2nd and 3rd spheres for kinematic coupling were still in curing process.

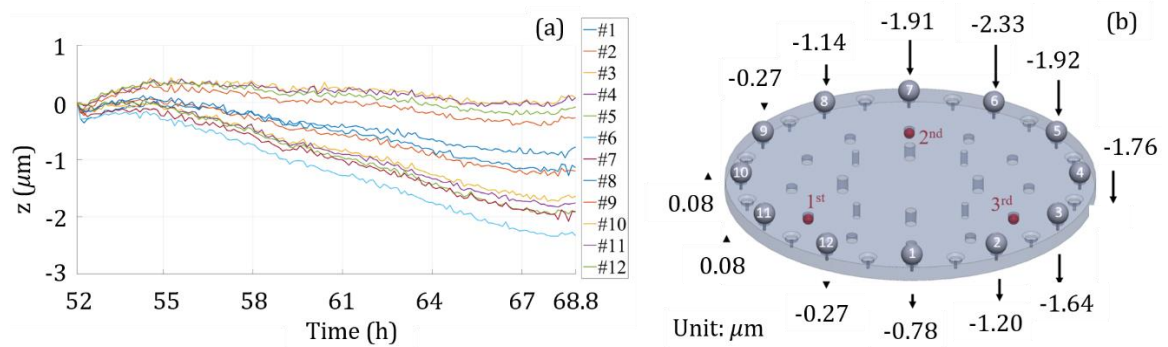


Figure 4.7. Monitored position variation of spheres after assembly: (a) relative z coordinates of spheres from the 52th hour to 68.8th hour (b) schematic of z coordinate variations of spheres between the 52th hour and 68.8th hour.

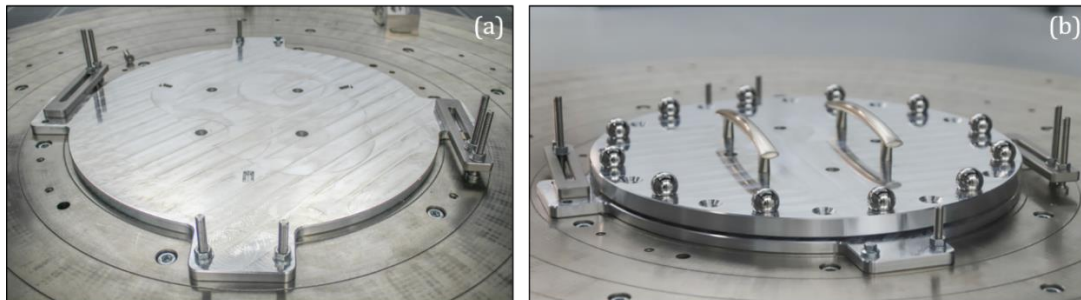


Figure 4.8. Assembled artifact: (a) lower plate fixed on the RT (b) entire artifact.

After the lower plate was fabricated, the whole artifact (upper and lower plates) was secured on the static RT, as showed in Figure 4.8(a). The second stability test was carried out from the 74th hour to the 158th hour after the assembly of the whole artifact (Figure 4.8(b)).

The position variations of spheres came from several sources: (i) clamping force on the lower plate; (ii) unreleased stress of the lower and upper aluminum plates from machining process; glue curing process of the 12 high precision spheres; (iii) glue curing process of the 3 spheres for kinematic coupling; (iv) soaking process of artifact to reach thermal equilibrium status. The whole artifact became more stable as time elapsed (Figure 4.9). The sudden change of sphere coordinates at the 116th hour in Figure 4.9 resulted from the interruption of experiment. The CMM was stopped, and z column were moved up by 1 m for several minutes. It seems the CMM took time to reach a new thermal equilibrium status after resuming the experiment. At the last six hours, the variation rate in the x, y and z directions was less than $0.3 \mu\text{m}$. Because the y axis was realized by the bridge of this CMM, its temperature drift was higher than the other two axes.

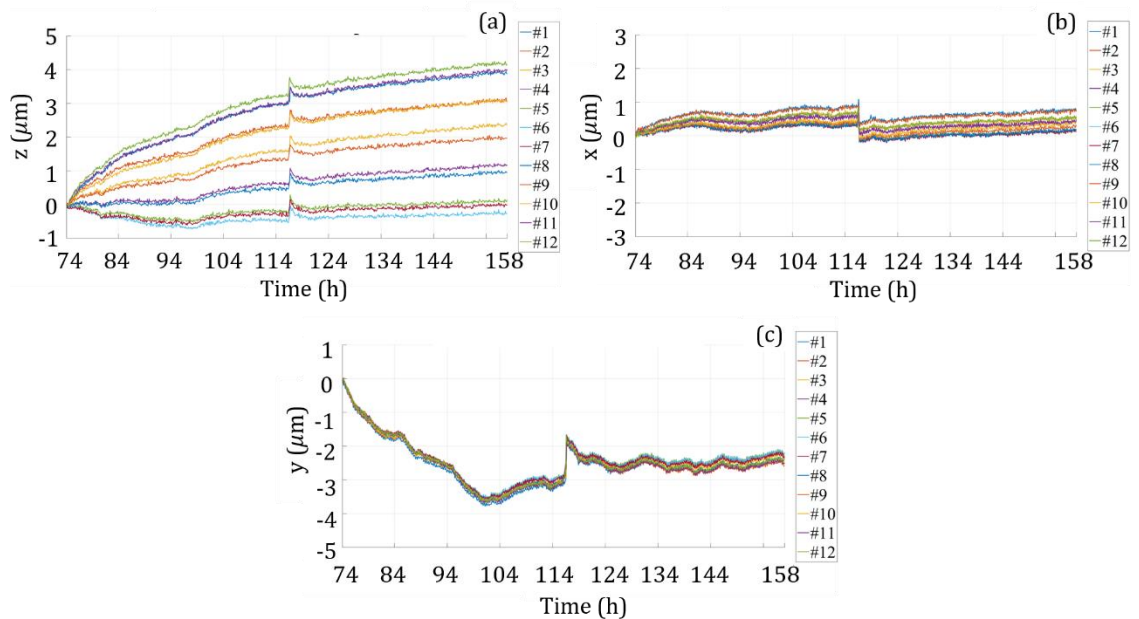


Figure 4.9. Position changes of spheres from the 74th hour to the 158th hour: (a) z coordinates (b) x coordinates (c) y coordinates (the sudden change of sphere coordinates at the 116th hour resulted from the interruption of experiment).

After one week, the coordinates of every sphere varied within $\pm 0.2 \mu\text{m}$ in 24 hours, indicating that the artifact reached an equilibrium status. This environment had excellent temperature control. The drifts of ambient temperature, part temperature and temperature of CMM components were less than 0.1°C in 24 hours.

4.2 Setup of ball step gage (BSG)

A BSG can be used to calibrate the CMM's geometric deviations at measuring the length between two pre-defined points in the measuring volume. An 8-ball BSG (Figure 4.10 (a) and (b)) with a nominal step of 100 mm was used to test the geometric deviations of the CMM at the defined measuring positions (Section 2.3). The BSG was aligned along the x axis of the frame CS. Kinematic coupling allowed free expansion of the BSG. The #4 ball was centered on the RT, with eccentricity of $69.3 \mu\text{m}$ (Figure 4.10(c)).

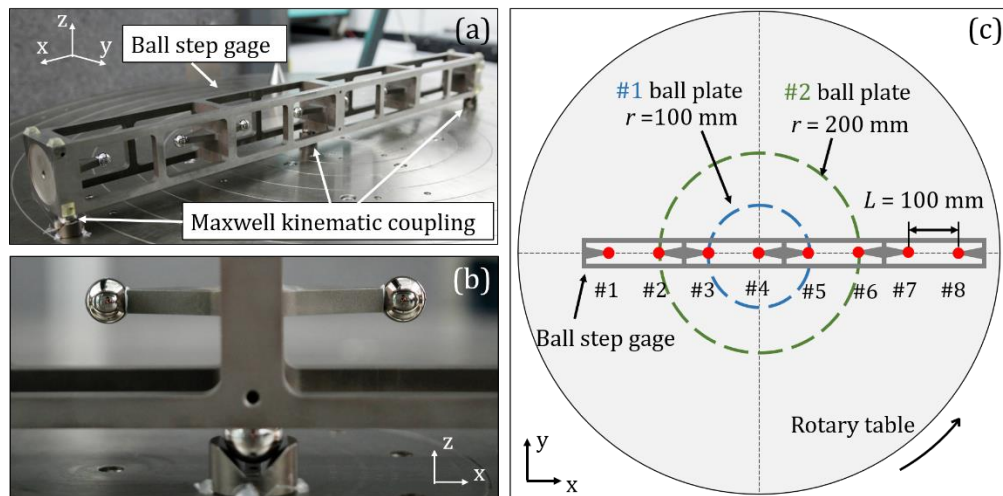


Figure 4.10. Setup of BSG on the RT: (a) structure and kinematic coupling (b) detailed view of the triangular beams supporting the spheres (c) schematic of location and alignment of BSG at the initial rotary position (0°).

4.3 Spindle error analyzer (SEA)

4.3.1 Setup of SEA

The SEA measures and analyzes a spindle's five error motions, including three translational error motions δ_x, δ_y and δ_z , and two tilt error motions ε_x and ε_y . Lion Precision SEA system consists of a 25.4 mm diameter dual master ball target, five noncontact capacitive sensors, a nest (sensor holder), seven temperature sensors, a data acquisition (DAQ) device and SEA software. The target is normally installed in the spindle's tool holder, and the nest is clamped on the table.

In RT calibration, the target was centered and fixed on the RT with three toe clamps. However, mounting the sensor holder on the probe head of the CMM was not feasible, because the weight of the sensor holder exceeded the load limit of the probe head. As shown in Figure 4.11, an in-house made metrology frame fixed the sensor holder over the RT.

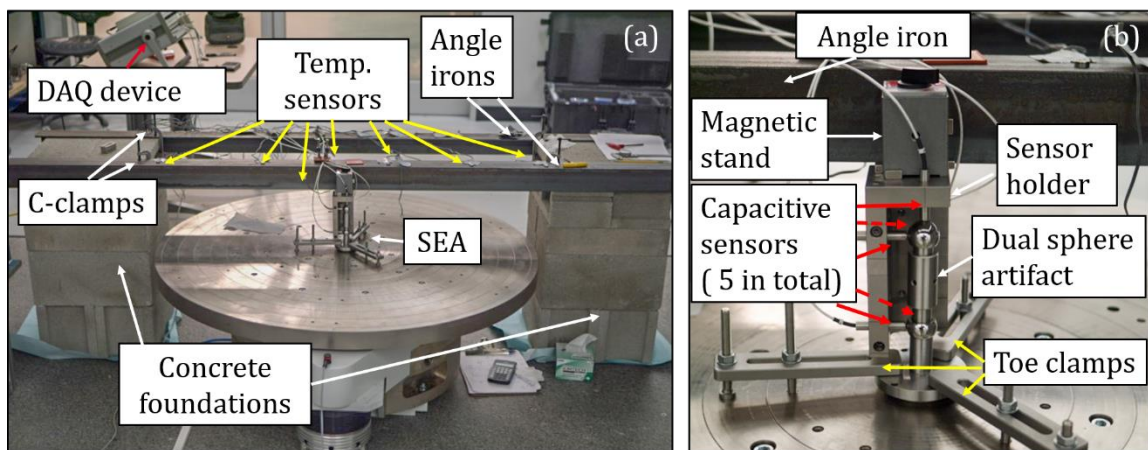


Figure 4.11. Setup of spindle error analyzer on a Zollern ZART 1200.0390.0 aerostatic rotary table: (a) illustration of an in-house made metrology frame, which fixed the sensor holder over the rotary table (b) fixture of SEA system on rotary table.

The beam bridge type metrology frame consisted of two concrete towers and two angle irons. In a four-layer configuration of concrete block towers, each of the 1st, 2nd and 4th layers had two standard cored concrete blocks ($0.194\text{ m} \times 0.194\text{ m} \times 0.397\text{ m}$), while the 3rd layer had two cap concrete blocks ($0.921\text{ m} \times 0.194\text{ m} \times 0.397\text{ m}$). Blocks in the even layers were oriented perpendicular to the ones in odd layers. Loctite Power Grab Ultimate construction adhesive was applied to bond the blocks. Functioning as horizontal beams across the two towers, two $1.500\text{ m} \times 0.076\text{ m}$ angle irons were fixed at the edges of the concrete towers with c-clamps. 0.163 meter working space existed between the angle irons and RT.

The sensor holder was attached to an angle iron using a magnetic stand. Noncontact capacitive sensors X1 and X2 recorded the x displacements of the lower and upper spheres, respectively. Sensors Y1 and Y2 measured the y displacements of the two spheres. Sensor Z2 measured the z displacement of the upper sphere. Alignments of the target and sensor holder were completed by trial and error method. In each iteration, the RT was rotated by one cycle. Offsets of the target in the x and y directions were observed using SEA software. A T-handle hex wrench functioned as a micro-hammer to adjust the initial position of the target.

4.3.2 Drift test of SEA system

An 18-hour drift test was performed to evaluate the stability of the metrology frame, sensor holder, artifact and associated fixtures. The RT was held static throughout the test.

The 1st to 6th temperature sensors were attached to the top of the angle iron, which held the magnetic stand and nest (Figure 4.11(a)). Six sensors were evenly distributed

between two concrete towers. Less than 0.05°C temperature variation was observed (Figure 4.12(a)). The 7th sensor reported 0.1°C variation of ambient air temperature near the nest (Figure 4.12 (b)). Less than $0.3\ \mu\text{m}$ drifts were reported by sensors X1, X2, Y1 and Y2 (Figure 4.12(c)). Sensor Z recorded $1.5\ \mu\text{m}$ drift, which might have been caused by a creeping of the sensor holder due to gravitational force. Later experiments reflected much less drift.

However, the X1, X2 and Z displacement sensors, as well as the seven temperature sensors, recorded oscillations with 4-minute periods (Figure 4.12(d)). The X1 and X2 sensors showed stable oscillation, while the Z sensor was more correlated with ambient temperature. The Y1 and Y2 data were stable throughout the drift test.

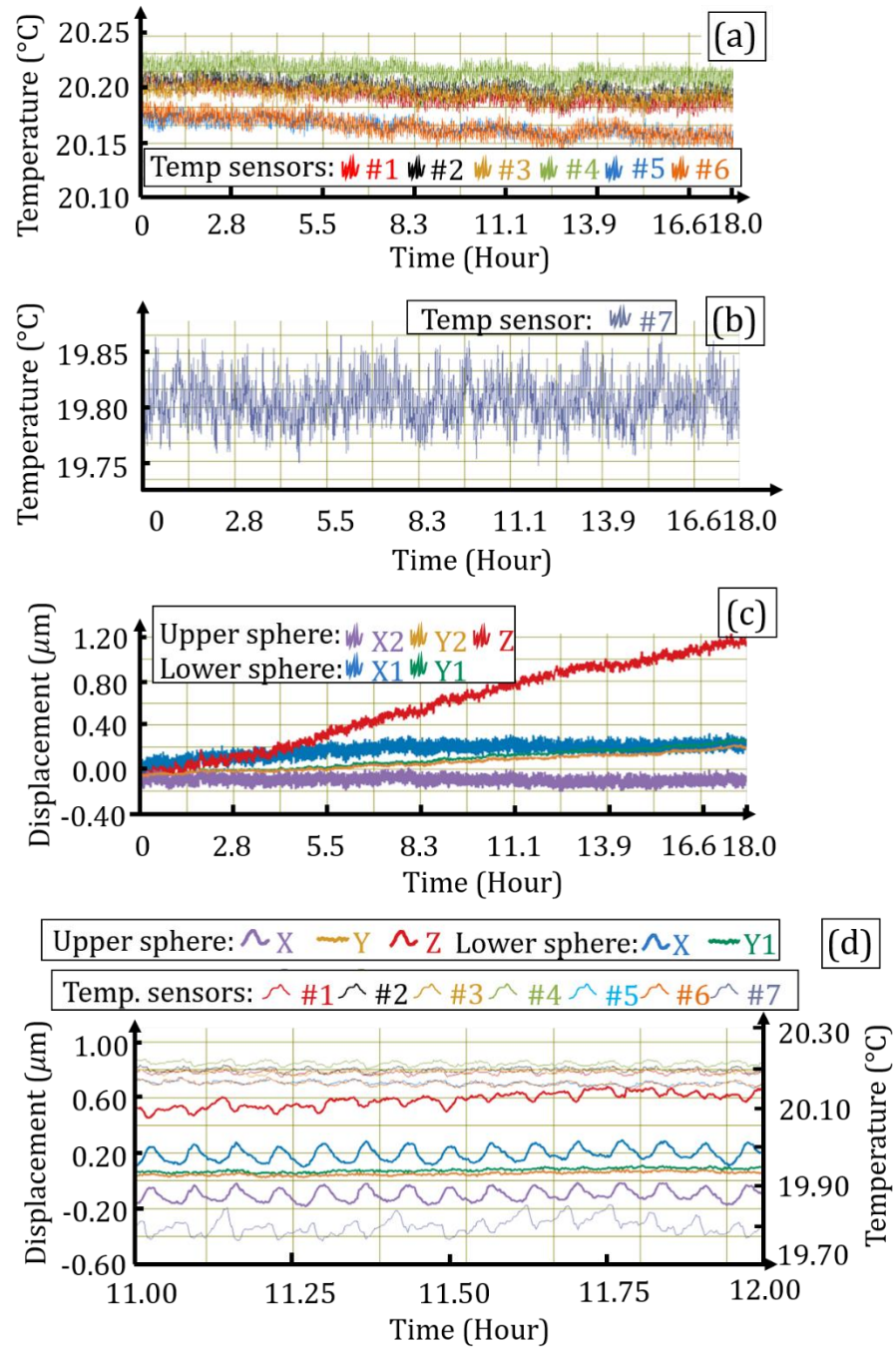


Figure 4.12. 18-hour drift test of SEA system: (a) temperature data of six sensors attached on an angle iron (b) ambient temperature near ball target (c) displacements data of five capacitive sensors (d) displacements and temperatures from the 11th hour to 12th hour.

Two possible explanations regarding the cause of the oscillation were discussed.

The first was that the air temperature of the room oscillates with a period of 4 minutes,

caused by cycling of the environment control system. Then, the thermal expansion of the metrology frame, magnetic stand and nest would theoretically shift the positions of the capacitive sensors and their readings. A second possible explanation was that the facility regulated the air pressure supplying the aerostatic bearings with a period of 4 minutes. Because the film thickness of axial and radial air bearings of the RT varied with the supplied pressure, the positions of rotor and attached double master sphere target were not expected to be constant. In the mechanical design of the RT, there is a belt which causes a net force in the x direction. The recorded temperatures were correlated with the pressure variation and the displacement sensors, because the supplied pressure variation also influenced the outlet temperature of air bearings.

Another test was carried out to further study the phenomena. A master sphere was fixed at the center of the static RT. Every two seconds, the CMM probed an equator point of the master sphere, in the -x direction. Displacements of the master sphere along the x-axis were recorded for 30 minutes. A similar test was carried out by repeatedly probing the pole of the sphere in the -z direction.

As shown in Figure 4.13, the displacements had periods of 4-minutes, matching the results from the drift test. X and z displacements of the master sphere had magnitudes of $0.15\ \mu\text{m}$ and $0.08\ \mu\text{m}$, respectively, which were similar to results from the previous drift test (Figure 4.12(d)). Because the CMM had higher non-repeatable probing deviations along the x-axis than along the z-axis, Figure 4.13(a) showed more scatter data than Figure 4.13(b). It is likely that oscillations with 4-minute periods originated from the oscillations of supplied air pressure.

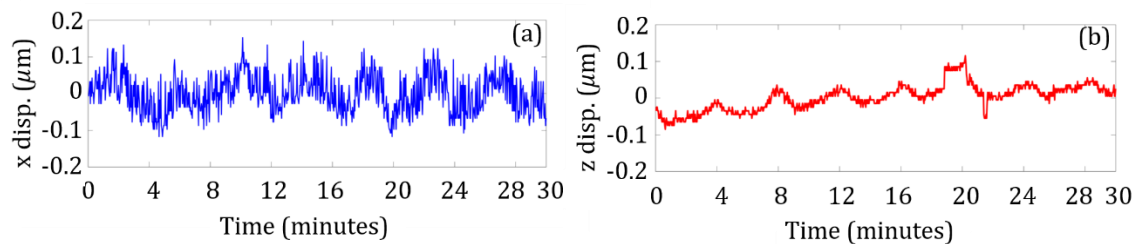


Figure 4.13. Displacements of a master sphere, fixed at the center of RT, and repeatedly probed at a point in $-x$ and $-z$ directions, respectively: (a) displacement along x -axis (b) displacement along z -axis.

For verification purpose, a pressure sensor was connected to the inlet pipe to monitor the inlet pressure. As shown in Figure 4.14, the inlet pressure oscillated between 99.2 psi and 99.5 psi, with a period around 4 minutes. The deep valleys occurring at the 3.5th, 12.7th and 22th minutes were originated from the associated air filter system, which regularly opened a side valve for several seconds to remove any accumulated oil and water in the supplied air.

In total, the built metrology frame provided very stable support to the sensor holder of the SEA.

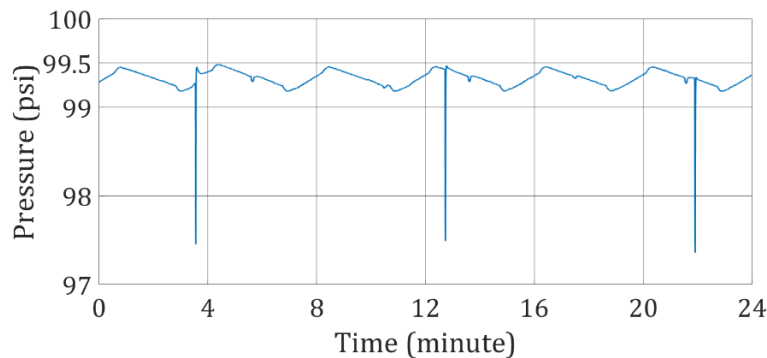


Figure 4.14. Sample inlet air pressure of the entire system.

4.4 Separation of CMM deviations

4.4.1 BSG

In this test, the BSG functioned as an uncalibrated double ball bar. As shown in Figure 4.10 and Figure 4.15, the #4 sphere was centered on the RT, while the #6 sphere was placed 200 mm off-centered. The table was rotated by 15 cycles in the CCW direction in a step of 7.5° . The coordinate system rotated together with the RT. At each step, the #4 and #6 spheres were measured. The relative coordinates of the #6 sphere to the #4 sphere at the t^{th} cycle ($t = 1, \dots, 10$) and i^{th} rotary position ($i = 1, \dots, 48$) are presented in Equation 4.1.

$$\begin{bmatrix} x'_{6,t,i} \\ y'_{6,t,i} \\ z'_{6,t,i} \end{bmatrix} = \begin{bmatrix} x_{6,t,i} \\ y_{6,t,i} \\ z_{6,t,i} \end{bmatrix} - \begin{bmatrix} x_{4,t,i} \\ y_{4,t,i} \\ z_{4,t,i} \end{bmatrix} \quad (t = 1, 2, \dots, 10; i = 1, 2, \dots, 48) \quad (4.1)$$

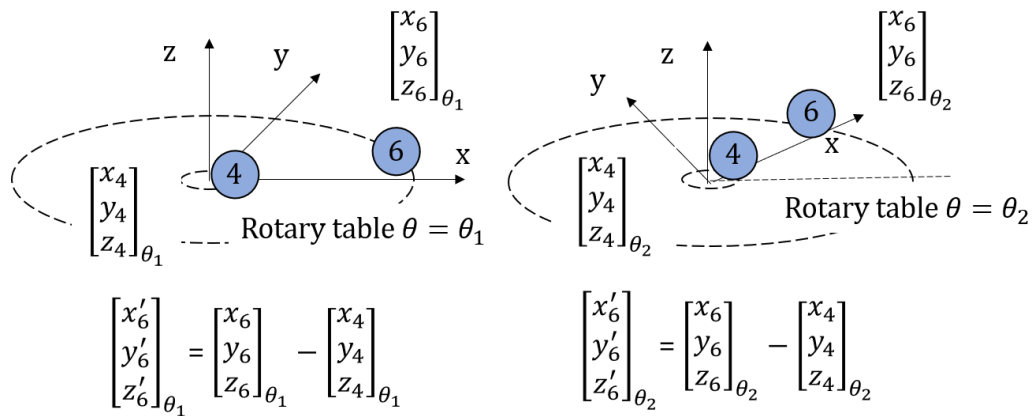


Figure 4.15. Schematic of sphere positions in the test.

Equation 4.2 gives the position deviations of the #6 sphere at (t^{th} , i^{th}) measurement from the mean values of all measurements.

$$\begin{bmatrix} \Delta x'_{6,t,i} \\ \Delta y'_{6,t,i} \\ \Delta z'_{6,t,i} \end{bmatrix} = \begin{bmatrix} x'_{6,t,i} \\ y'_{6,t,i} \\ z'_{6,t,i} \end{bmatrix} - \frac{1}{10 \times 48} \begin{bmatrix} \sum_{t=1}^{10} \sum_{i=1}^{48} x'_{6,t,i} \\ \sum_{t=1}^{10} \sum_{i=1}^{48} y'_{6,t,i} \\ \sum_{t=1}^{10} \sum_{i=1}^{48} z'_{6,t,i} \end{bmatrix} \quad (t = 1, 2, \dots, 10; i = 1, 2, \dots, 48)$$

(4.2)

The position deviations originated from three sources: (i) error motions of the RT (Section 4.4.1.1); (ii) CMM's probing error (Section 4.4.1.2); (iii) CMM's geometric deviations (Section 4.4.1.3). The contribution of three sources are discussed in detail.

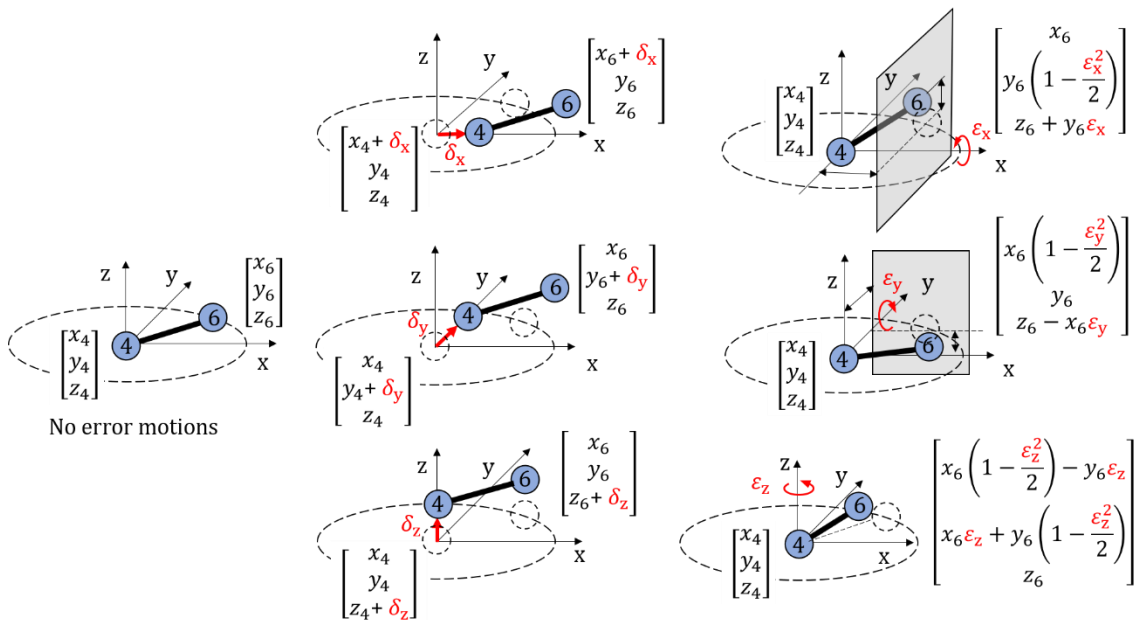


Figure 4.16. Influence of each error motion to the coordinates of two spheres (small-angle approximation was applied: e.g., $\sin \varepsilon_x \approx \varepsilon_x$ and $\cos \varepsilon_x \approx 1 - \frac{\varepsilon_x^2}{2}$).

4.4.1.1 Error motions of RT

As illustrated in Figure 4.16, the δ_x varied the positions of two spheres simultaneously. Therefore, the relative coordinates of the #6 sphere to the #4 sphere were

unchanged. In a similar manner, δ_y and δ_z had no effect on the relative coordinates of the #6 sphere. ε_x and ε_y mainly changed the z coordinates of the #6 sphere, while ε_z varied the x and y coordinates of the #6 sphere. Obviously, the influences of ε_x , ε_y and ε_z to the position of centered #4 sphere were negligible. The effects of error motions to the measured relative coordinates of the #6 sphere are summarized in

Table 4.1. The non-zero terms are uncertainty contributors in this test.

Table 4.1. Influence of each error motion to the measured relative position of the off-centered #6 sphere to the centered #4 sphere.

	$\Delta x'_{6,t,i}$	$\Delta y'_{6,t,i}$	$\Delta z'_{6,t,i}$
$\delta_{x,t,i}$	0	0	0
$\delta_{y,t,i}$	0	0	0
$\delta_{z,t,i}$	0	0	0
$\varepsilon_{x,t,i}$	0	$-\frac{\varepsilon_{x,t,i}^2}{2} y_{6,t,i} \approx 0$	$\varepsilon_{x,t,i} y_{6,t,i}$
$\varepsilon_{y,t,i}$	$-\frac{\varepsilon_{y,t,i}^2}{2} x_{6,t,i} \approx 0$	0	$-\varepsilon_{y,t,i} x_{6,t,i}$
$\varepsilon_{z,t,i}$	$-\frac{\varepsilon_{z,t,i}^2}{2} x_{6,t,i} - \varepsilon_{z,t,i} y_{6,t,i}$ $\approx 0 - \varepsilon_{z,t,i} y_{6,t,i}$	$-\frac{\varepsilon_{z,t,i}^2}{2} y_{6,t,i} + \varepsilon_{z,t,i} x_{6,t,i}$ $\approx 0 + \varepsilon_{z,t,i} x_{6,t,i}$	0

4.4.1.2 Probing error

As shown in Figure 4.10(b), each sphere was supported by a triangular beam, which reduced the accessibility of the sphere near the equator. As demonstrated in Figure 4.17(a), a 10-point probing strategy was applied to cover a sufficient area on the upper hemisphere, while avoiding collisions between the probe stylus and the triangular beam.

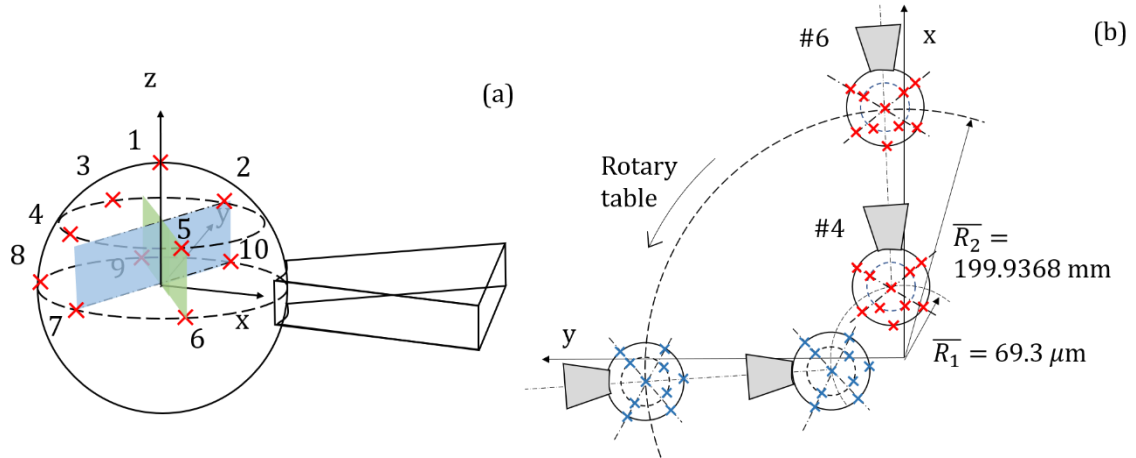


Figure 4.17. Probing strategy for a sphere on the BSG: (a) locations of probing points (b) orientation of probing points at rotary position of 0° and 90° (top view).

For each sphere at each step, the least square center and least square radius were calculated. In Equation 4.3, $L_{q,6,t,i}$ represents the distance from the coordinates of the q^{th} probing point ($q = 1, 2, \dots, 10$) to the least square center of the #6 sphere at the t^{th} cycle, i^{th} rotary position. The difference between $L_{q,6,t,i}$ and $R_{6,t,i}$ were used to calculate the probing error $\Delta P_{q,6,t,i}$ in Equation 4.4. The probing error is also illustrated in Figure 4.18(b). Figure 4.18(c) shows that the probing system measured the #8 point on the sphere #6 from all eight probing directions in Figure 4.18(a), after the table was rotated by one cycle. The results represented the probing errors when the probing system touches a point on sphere.

$$\Delta L_{q,6,t,i} = L_{q,6,t,i} - R_{6,t,i} \quad (q = 1, 2, \dots, 10, t = 1, 2, \dots, 10; i = 1, 2, \dots, 48) \quad (4.3)$$

$$\Delta P_{q,6,t,i} = \Delta L_{q,6,t,i} - \frac{1}{48} \sum_{i=1}^{48} \Delta L_{q,6,t,i} \quad (q = 1, 2, \dots, 10, t = 1, 2, \dots, 10) \quad (4.4)$$

The locations of probing points were rotated with the RT (Figure 4.17(b)). Namely, the probe touched the same set of points on the targeted ball. As shown in Figure 4.18(a), the same #8 point on the #6 sphere was probed at various rotary positions. Therefore, the

form deviation of #6 sphere would not affect the separated probing error. Moreover, the error motions of RTs and the geometric deviations of CMM also had negligible effects on the calculation of probing error.

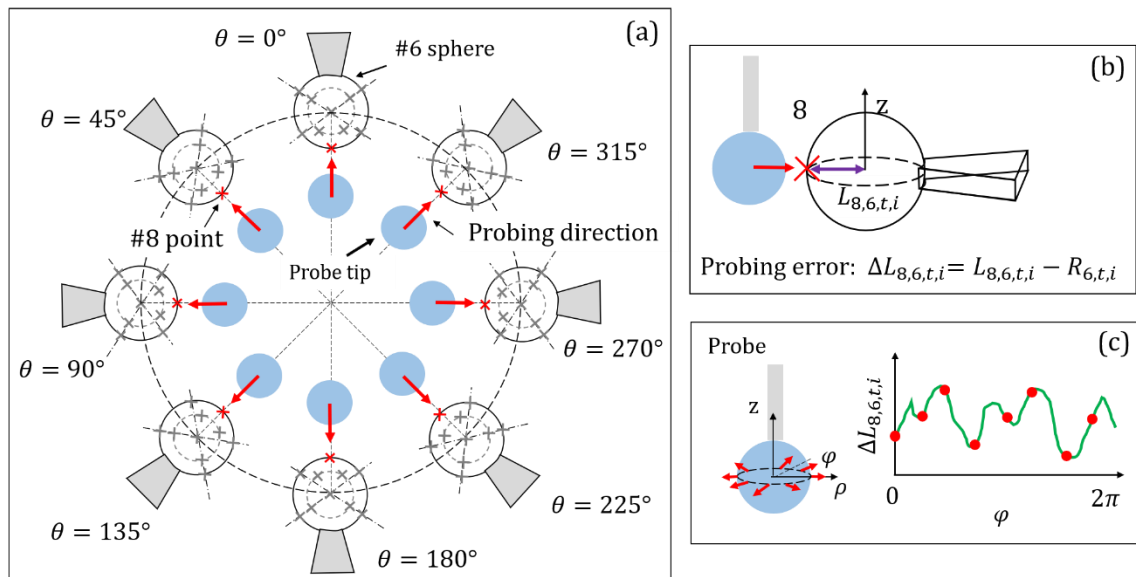


Figure 4.18. Schematic of probing error detection: (a) Probing direction for the same point on a probed sphere at various rotary position (b) Probing error calculation of an arbitrary measurement for the #8 point (c) Detected probing error at the eight sampled directions using the #8 point.

The recorded probing errors are shown in Figure 4.19. The #1 point was the contact point between the bottom of the probe and the pole of sphere. Compared with the other probing points, the #1 point had relatively low probing errors. For any of the other probing points, the probe tip always touched a same point on the sphere along the normal directions.

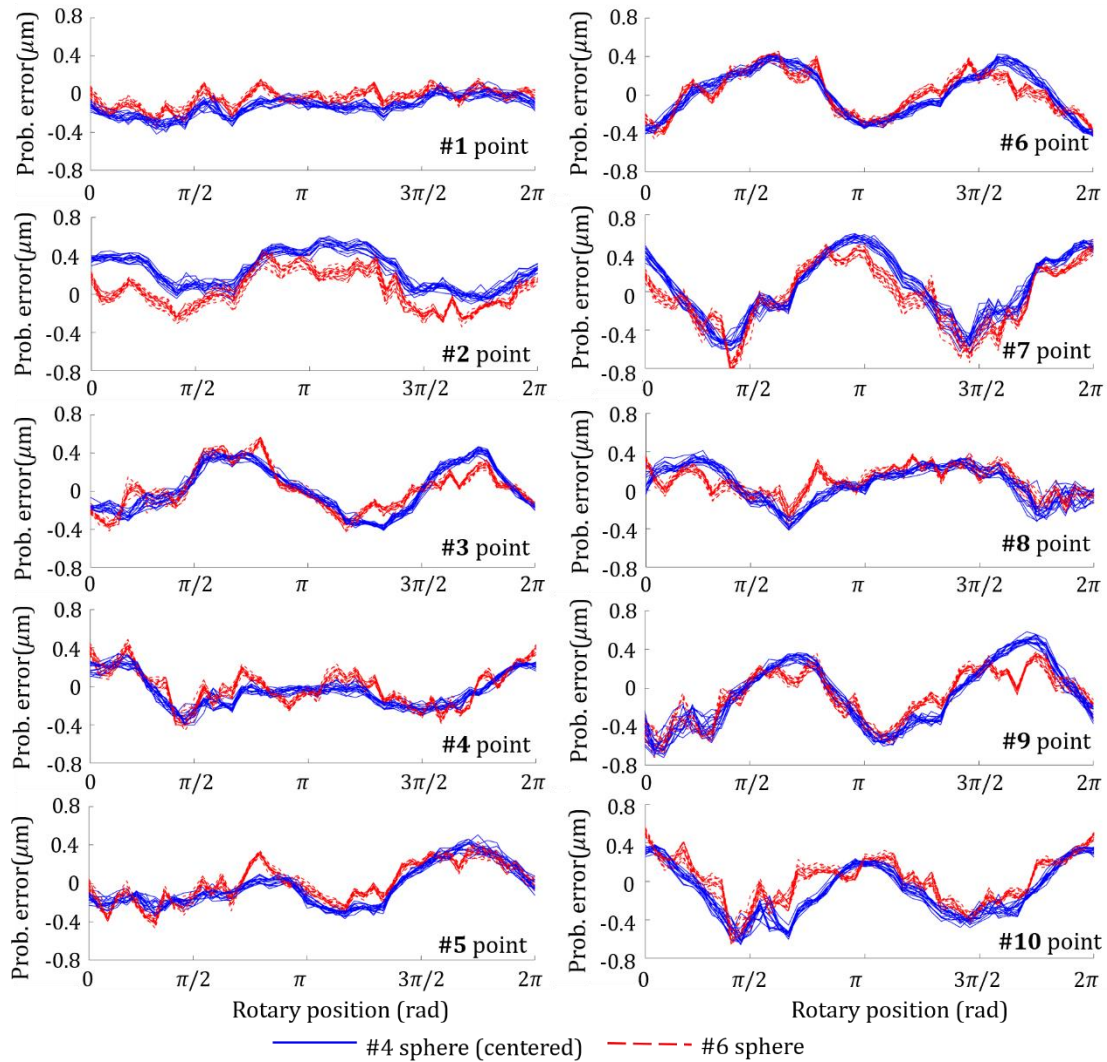


Figure 4.19. Separated probing errors at 10 probing points on the #4 and #6 spheres when the table was rotated by 10 cycles in steps of 7.5° .

As shown in Figure 4.17(a), the #6 and #9 points were two equator points opposite to each other. Comparable error patterns were observed. Similar results were found for the #7 and #10 points. Apparently, the different initial contact direction of the #6 to #10 points in the frame CS resulted in the phase shifts, which should be compensated. The elliptical patterns in Figure 4.20 reflect the probing errors detected using different probing points.

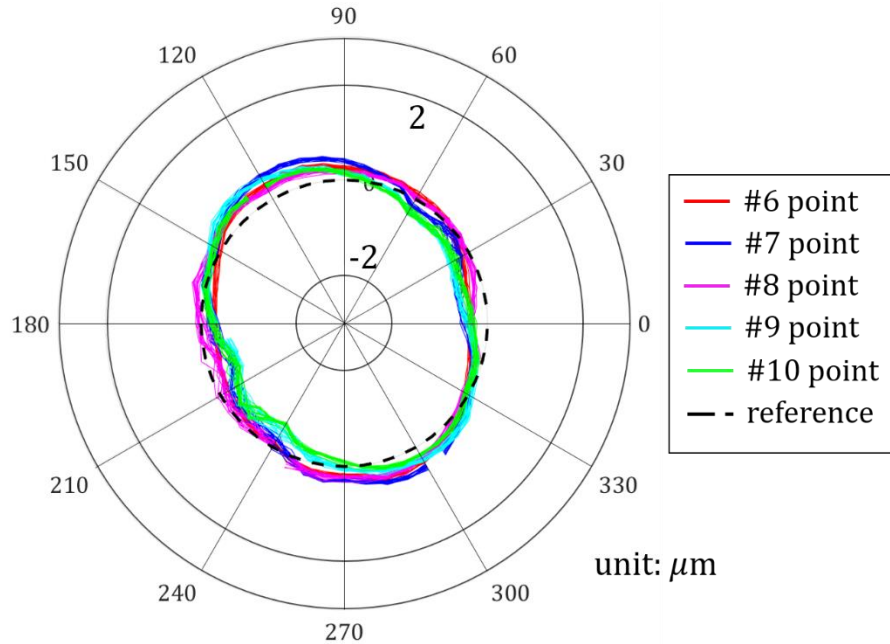


Figure 4.20. Detected probing errors using different probing points, after removing the phase shifts due to different initial position.

As shown in Figure 4.10(c), the triangular beams for even spheres were oriented along the -x direction at the initial rotary position (0°). Therefore, the same set of probing points were applied for the # 4 and #6 spheres (Figure 4.17(b)). In Figure 4.19, probing errors on the # 4 and #6 were similar, which indicated that the probing error were independent from location of the probing system.

In the next step, the x, y and z deviations of two spheres resulting from the probing system were calculated. The averaging effect of multiple points made the magnitudes of x and y deviations much smaller than the magnitudes of single-point probing errors. Two spheres had similar patterns for the y deviations, so as for the z deviations. In the x direction, for each measuring position, the probing error at measuring the #6 sphere (Figure 4.21(a)) minus the probing error at measuring the #4 sphere (Figure 4.21(b)) were called residuals in Figure 4.21(c). These residuals were equal to the overall influence of the

probing system on the relative x coordinates of the #6 sphere. In a similar way, the overall influence of the probing system on the relative y and z coordinates of the #6 sphere were calculated (Figure 4.21 (f) and (i)).

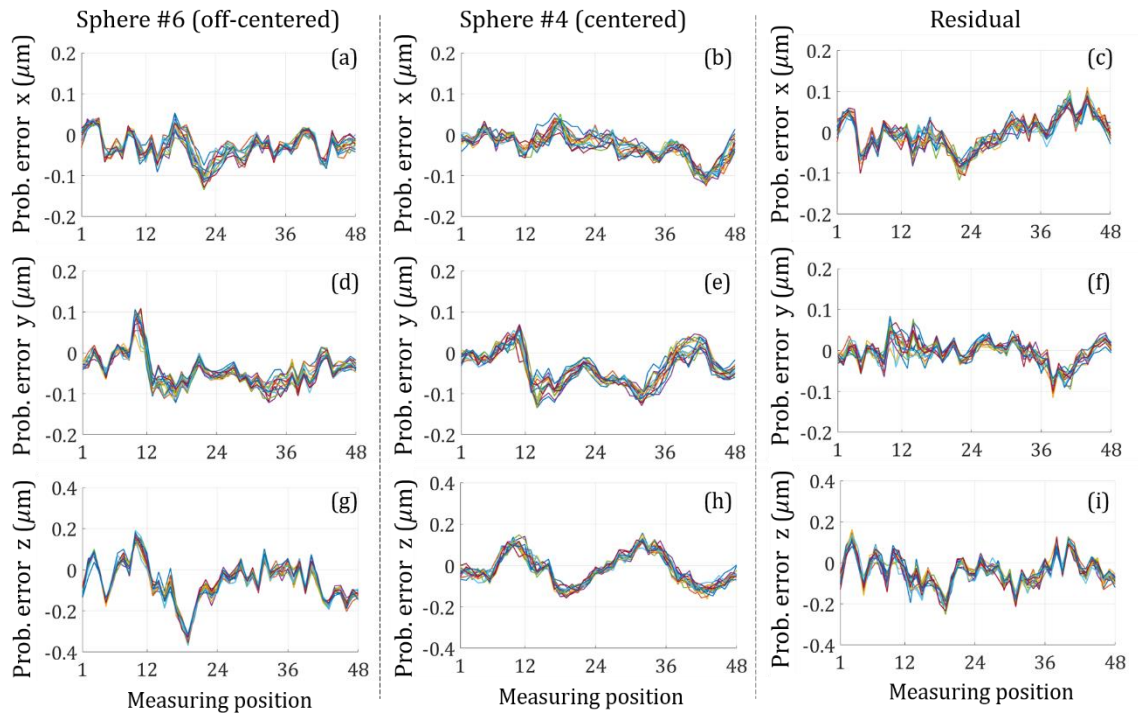


Figure 4.21. Deviations of sphere coordinates resulting from the probing system: (a), (d), (g) probing deviations at measuring the #6 sphere (b), (e), (h) probing deviations at measuring the #4 sphere (c), (f), (i) overall influence of the probing system on the relative coordinates of the #6 sphere.

4.4.1.3 CMM's geometric deviations

Next, the systematic component of the CMM's geometric deviations ΔP_{gs} were investigated. The radial, tangential and z coordinates of the #4 and #6 spheres are presented in Figure 4.22. As shown in Figure 4.16, the radial coordinates of the two spheres were affected by the error motions δ_x and δ_y of the RT, while other error motions resulted in second order errors. Moreover, because the periodicity of the δ_x error motion of this RT

was not equal to 2π (discussed later in Section 4.5), the radial deviations of either sphere in multiple cycles were not repeatable (Figure 4.22 (a) and (b)). The unknown error motion δ_x (or δ_y) had exactly same effects on both spheres at an arbitrary rotary position. Therefore, comparing the recorded radial deviation curves of two spheres can remove the unknown error motions δ_x (and δ_y). The results revealed the radial components of the CMM's geometric deviations, as shown in Figure 4.22(c). The influences of unknown ε_x , ε_y and ε_z to the separated tangential and z deviations of CMM's geometric deviations cannot be removed. It should be noted that the effect of probing error (Figure 4.21) had not been removed in Figure 4.22.

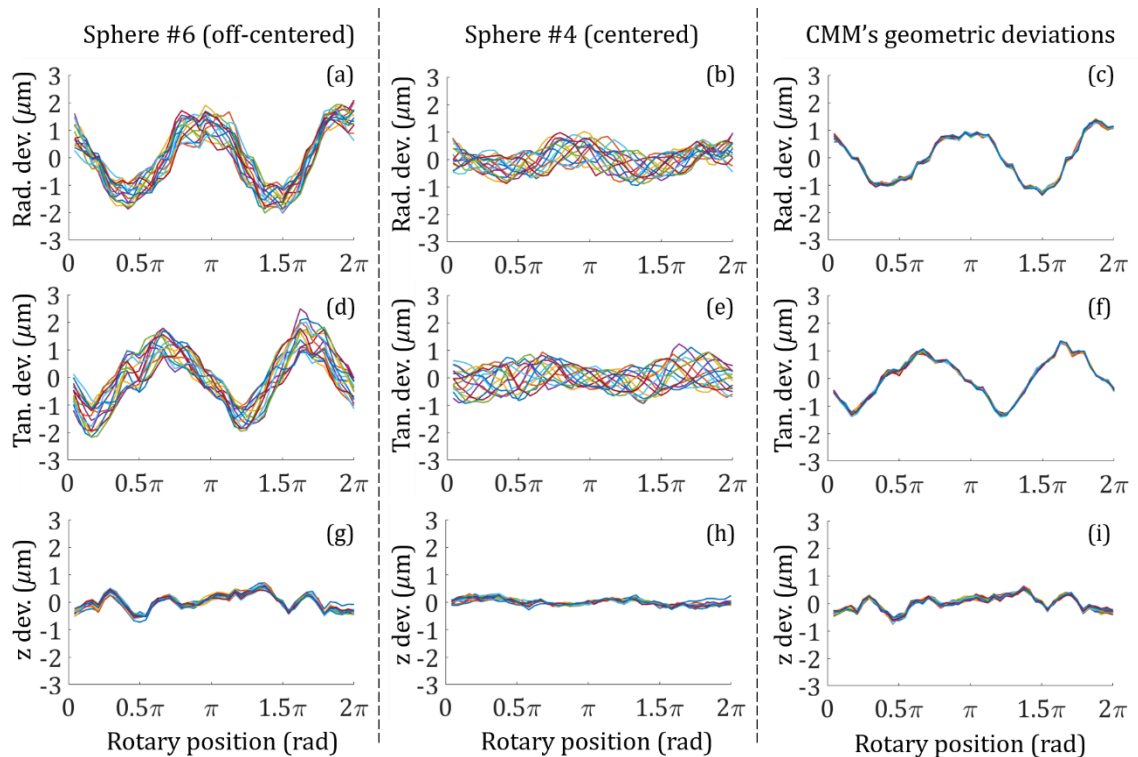


Figure 4.22. Separated systematic components of the CMM's geometric deviations at 48 measuring positions by comparing the coordinates of the #4 and #6 spheres in 10 cycles: (a), (d), (g) deviations of the #6 sphere in three directions from its average path in each cycle (b), (e), (h) deviations of the #4 sphere in three directions from its average path in each cycle (c), (f), (i) separated CMM geometric deviations.

In the second test, the #4 and #5 spheres were used in the similar testing procedure. As shown in Figure 4.23, the amplitudes of the separated radial and tangential deviations were about half for the previous test, while axial deviations were comparable. The CMM had lower geometric deviations at $r_{s0} = 100$ mm than at $r_{s0} = 200$ mm. Polar plots and 3D plots of the separated systematic components of the CMM's geometric deviations in two tests are presented in Figure 4.24.

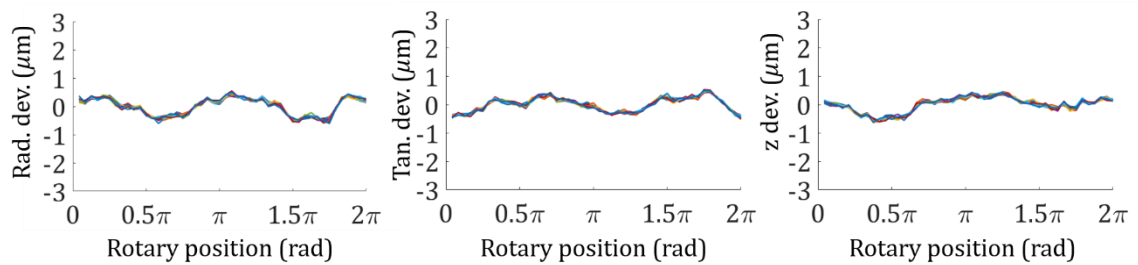


Figure 4.23. Separated systematic components of the CMM's geometric deviations by comparing the coordinates of the #4 and #5 spheres in 10 cycles: (a) radial deviations (b) tangential deviations (c) z deviations.

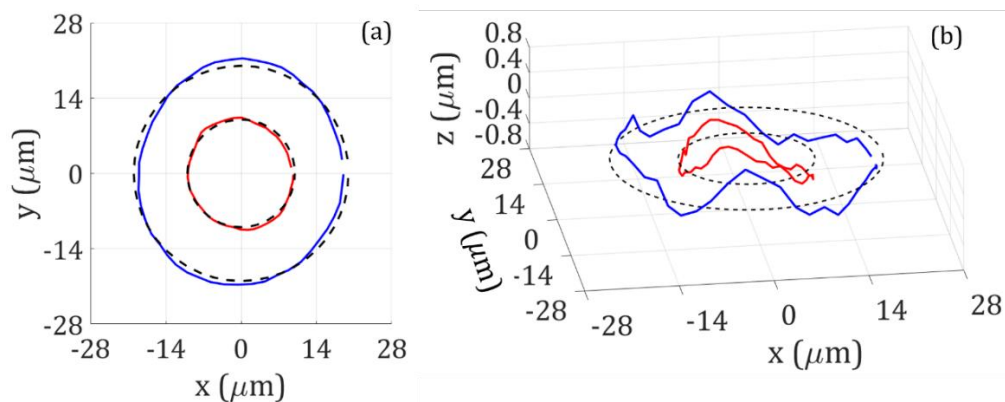


Figure 4.24. Separated systematic components of the CMM's geometric deviations at 48 measuring positions, where the ideal paths was reduced by a factor of 0.00001: (a) polar plot (top view) (b) 3D plot.

4.4.2 CMM systematic geometric deviations determined by the BSG and the CBP

For the CBP test, the RT was rotated by 8 cycles in the CCW rotating direction in steps of 7.5° . At each step, 15 points were probed on the #1, #3, #5, #7, #9 and #11 spheres. The number of measuring positions M was equal to the number of rotary positions in a cycle.

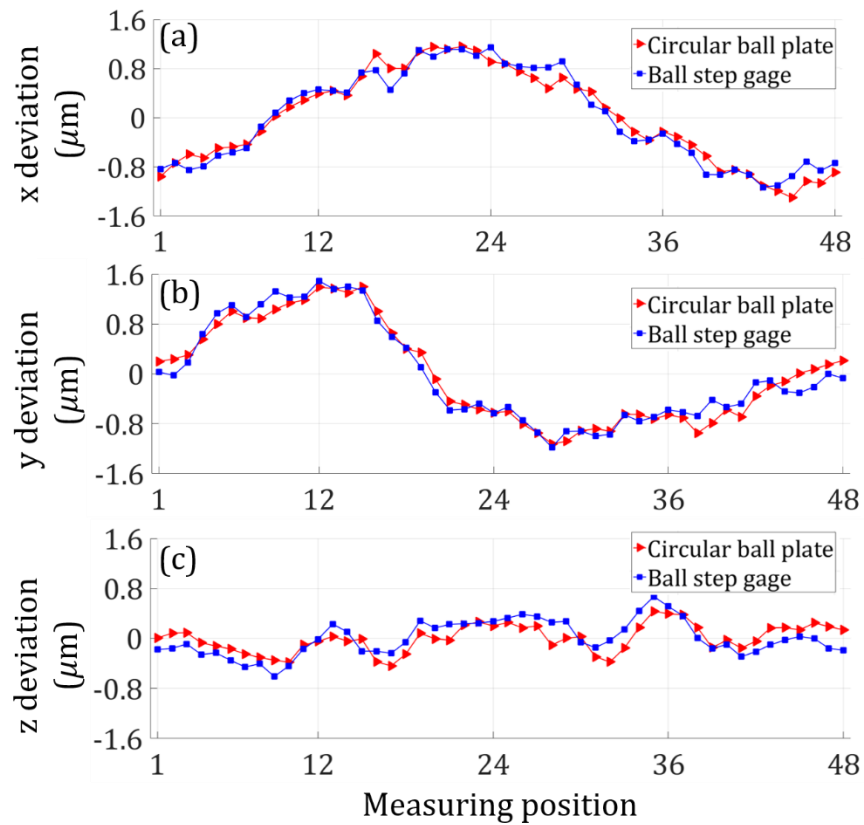


Figure 4.25. Systematic components of geometric deviations of the CMM at the 48 measuring positions: (a) x deviations (b) y deviations (c) z deviations.

The determined systematic components of geometric errors of the CMM at the 48 measuring positions were presented in Figure 4.25. Results from the BSG test in Figure 4.23 were translated from the Cylindrical CS to the Cartesian CS. It should be noted that

the 1st measuring position for the BSG test was opposite to the one in the CBP test. Therefore, results were shifted correctly for comparison.

The red curves and blue curves represented results obtained by the CBP and the BSG tests, respectively. Two methods detected similar results for the CMM's systematic geometric deviations. Hence, it validated that the proposed solution can separate CMM's deviation at the defined measuring positions.

4.4.3 Random components of the CMM's geometric deviations

The #2, #4 and #6 spheres were used to simulate the case when $r_{s0} = 200$ mm. At each step, the #2 sphere was rotated to the k^{th} ($k = 1, 2, \dots, M$) pre-defined measuring position. Meanwhile, the #6 sphere was at the opposite $\left(k + \frac{M}{2}\right)^{\text{th}}$ measuring position.

The random components of CMM's geometric deviations ΔP_{gr} were investigated first. At each measuring position, the CMM first measured the coordinates of the #2 and #4 spheres in turns for 12 repetitions. The relative coordinates of the #2 sphere with respect to #4 sphere were recorded. The residuals between the single distances and the mean value were regarded as the random components. The results of the 1st and 2nd repetitions were discarded to reduce the influences of CMM's warm-up process. Since 12 repetitions were completed within several minutes, the CMM's drift were neglected. Then, the relative coordinates of the #6 sphere with respect to #4 were also measured in same procedure.

As shown in Figure 4.26, the standard deviations of the radial, tangential and z components of ΔP_{gr} ranged from $0.02 \mu\text{m}$ to $0.06 \mu\text{m}$. Differences of results between using the #2 and #6 spheres were partially explained by the drift of CMM.

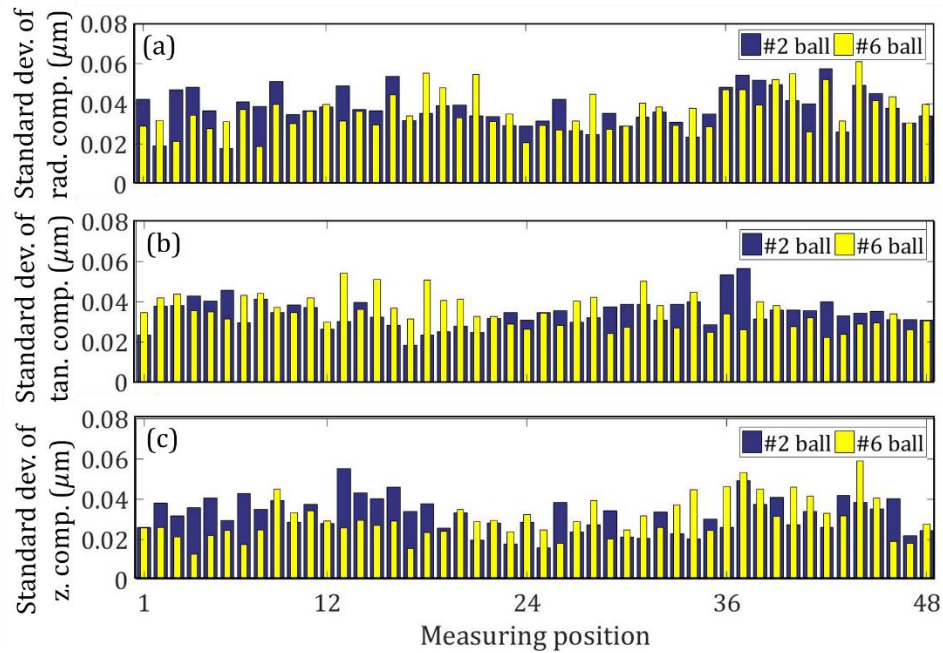


Figure 4.26. Standard deviations of the radial, tangential and z components of ΔP_{gr} from the reference point (#4 sphere) to 48 measuring positions, by measuring the relative coordinates of the #2 sphere to the #4 sphere, as well as the #6 sphere to the #4 sphere: (a) radial deviations (b) tangential deviations (c) z deviations.

In a similar way, the #3, #4 and #5 balls were used to simulate the case when r_{s0} was equal to 100 mm (Figure 4.27). No significant differences were observed in the two cases.

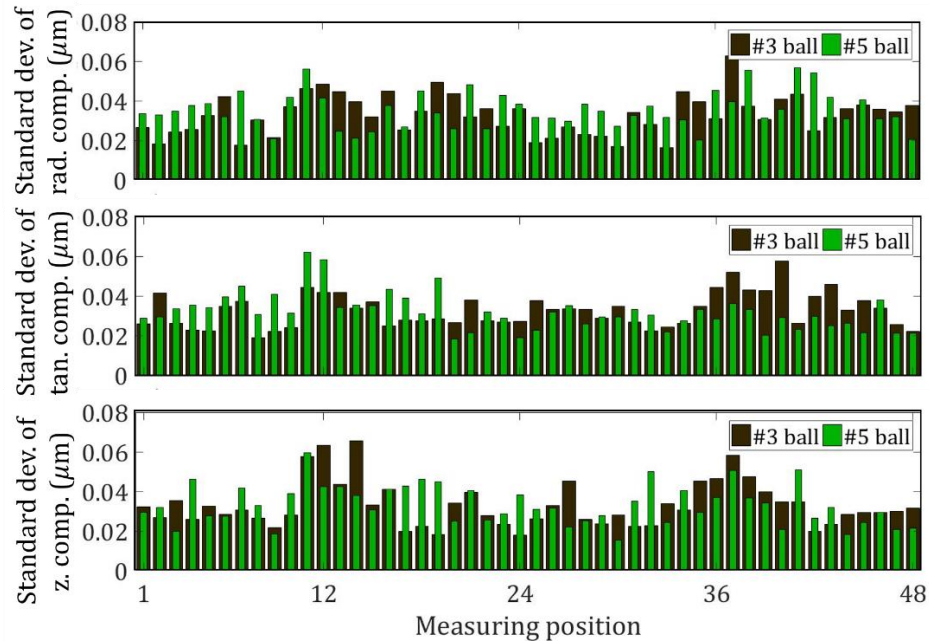


Figure 4.27. Standard deviations of the radial, tangential and z components of ΔP_{gr} from the reference point (#4 sphere) to 48 measuring positions. by measuring the relative coordinates of the #3 sphere to the #4 sphere, as well as the #5 sphere to the #4 sphere: (a) radial deviations (b) tangential deviations (c) z deviations.

4.5 Error motions of RT

4.5.1 Calibration procedure using spindle error analyzer

In the first SEA test (SEA T1), the RT was rotated by 4 cycles in the CCW direction in a step of 7.5° . The RT stayed at each rotary position for 20 seconds to obtain stable readings from the X1, X2, Y1, Y2 and Z1 capacitive gages. Then, the RT was calibrated in the CW direction in a similar procedure.

The SEA was uninstalled and reinstalled before performing the second SEA test (SEA T2). The RT was calibrated by 10 cycles in both CCW and CW directions. Experimental procedure for the CBP test was described in Section 4.4.2.

4.5.2 Experimental results

The separated error motions are presented in Figure 4.28 and Figure 4.29. Because the CBP test was completed several months later than the SEA T1 and SEA T2, the three experiments did not have a common reference rotary position. Therefore, data from the three experiments was aligned laterally for comparison.

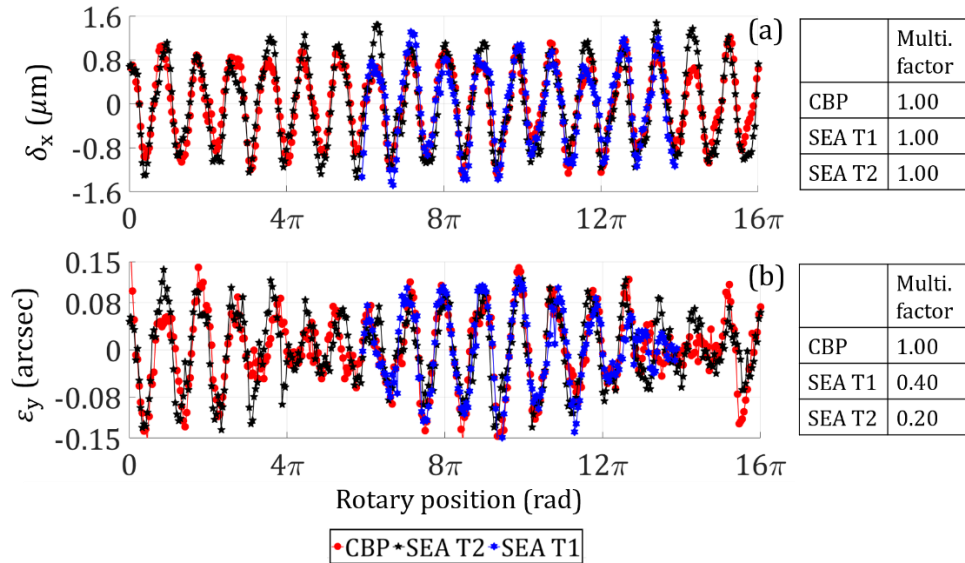


Figure 4.28. Error motions of the RT separated by the SEA T1 (blue curve), SEA T2 (black curve) and the CBP (red curve): (a) δ_x (b) ε_y .

The δ_x , δ_y and δ_z separated by the three tests were comparable. δ_y and δ_z were between $\pm 0.2 \mu\text{m}$, which were considered small for a large scale RT. δ_x was one order larger than δ_y and δ_z , which indicated that, at rotation, the whole RT mainly had a translational error motion along the x direction in the frame CS.

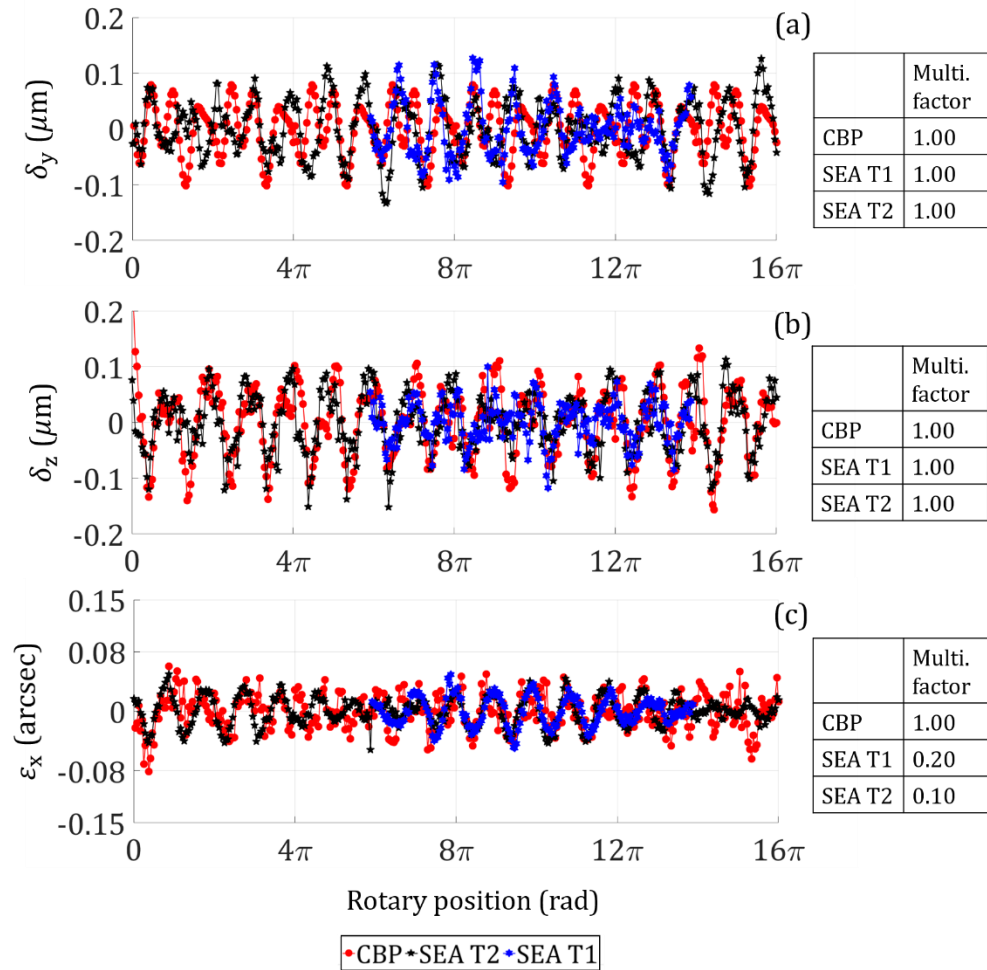


Figure 4.29. Error motions of the RT separated by the SEA T1 (blue curve), SEA T2 (black curve) and the CBP (red curve): (a) δ_y (b) δ_z (c) ε_x .

As shown in Figure 4.30, a flat belt was used to transmit the motor movement to the rotary table. The tension of the belt was the decisive factor for transmission of power. In this measuring system, the motor and two pinions of RT were aligned along the x-axis. During operation the driving power pulled the pinions towards the center. Hence, it was reasonable to observe larger δ_x than δ_y for this RT.

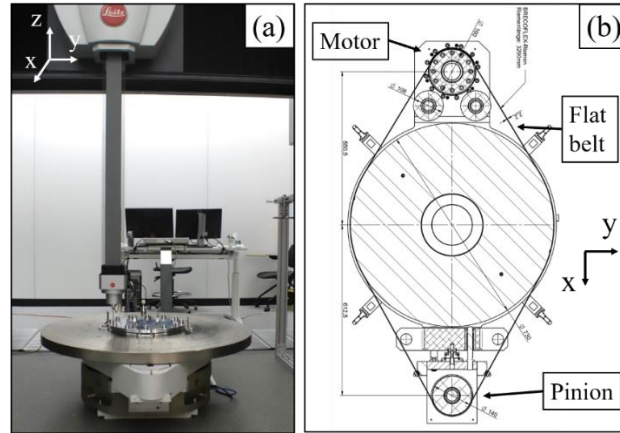


Figure 4.30. RT at UNC Charlotte: (a) orientation of the RT in the measuring system (b) schematic of driving train (bottom view).

Obviously, the periods of δ_x and ε_y were longer than 2π . The δ_x and ε_y obtained by the CBP test were replot in Figure 4.31 for detailed view. It seemed that the period of ε_y was around 8π by comparing data points in the 8 cycles ($[0, 16\pi]$). However, taking Figure 4.28 into account, the actual period were around 10π . Similar results for δ_y , δ_z and ε_x can be found in Figure 4.29.

The phenomena may have resulted from multiple sources. The first one was that the driving and driven pinions might have non-integer ratios of diameter. Moreover, one or more pinions may not have been positioned along the central line very accurately in the assembling process.

Although the ε_x and ε_y separated by the three tests have similar patterns, the amplitudes of ε_x and ε_y determined by SEA T1 and T2 were much larger than the ones by the CBP test. After multiplying the amplitudes of ε_x obtained from SEA T1 and T2 by 0.2 and 0.1, respectively, the results of all three tests results were comparable. Amplification factors of 0.4 and 0.2 for SEA T1 and T2 lead to close amplitudes of ε_y in the three tests.

It was likely that a scaling error existed in the SEA test data. The amplitudes of ϵ_x and ϵ_y were less than 0.3", which shows that the RT had low tilt error motions in non-load condition.

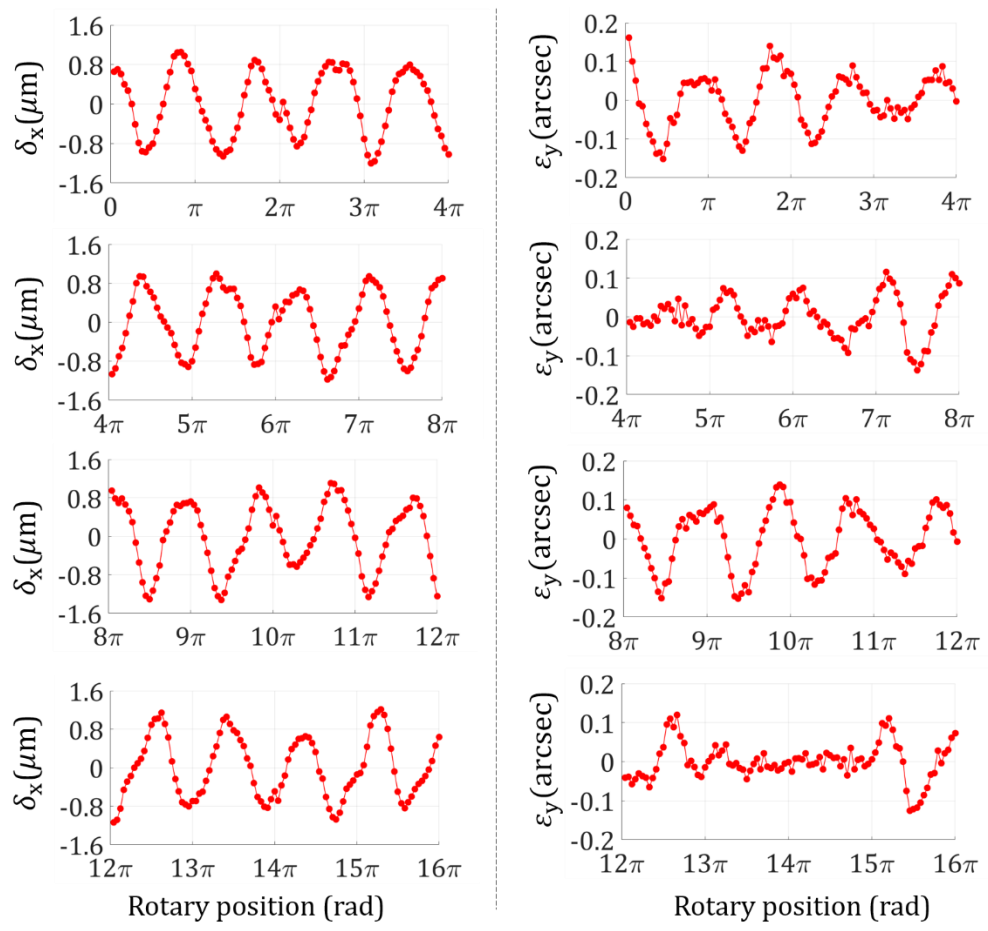


Figure 4.31. Separated δ_x and ϵ_y of the RT by the CBP test.

CHAPTER 5: ROTARY TABLES UNDER SYMMETRIC LOADS

In this chapter, the performances of one hydrostatic RT and two aerostatic RTs under symmetric loads were investigated.

5.1 Introduction of tested rotary tables

5.1.1 Hydrostatic RT

A Zollern ZHRT 1000.0340.0550 hydrostatic RT at the Bremen Institute for Metrology, Automation and Quality Science (BIMAQ), University of Bremen, Germany, was investigated. This table and a Leitz PMM-F 30.20.07 (CMM A) formed a 4-axis CMM for large scale metrology applications. A delivery system was designed and installed to facilitate the handling of large and heavy parts (Figure 5.1). Workpieces were loaded onto a steel or granite measuring palette using a traveling overhead crane or fork lifter at the loading gate. Then, the measuring palette was transported to and loaded on the RT. The unloading process was performed in the reverse way. Kinematic coupling between the RT and the palette assured positioning repeatability.

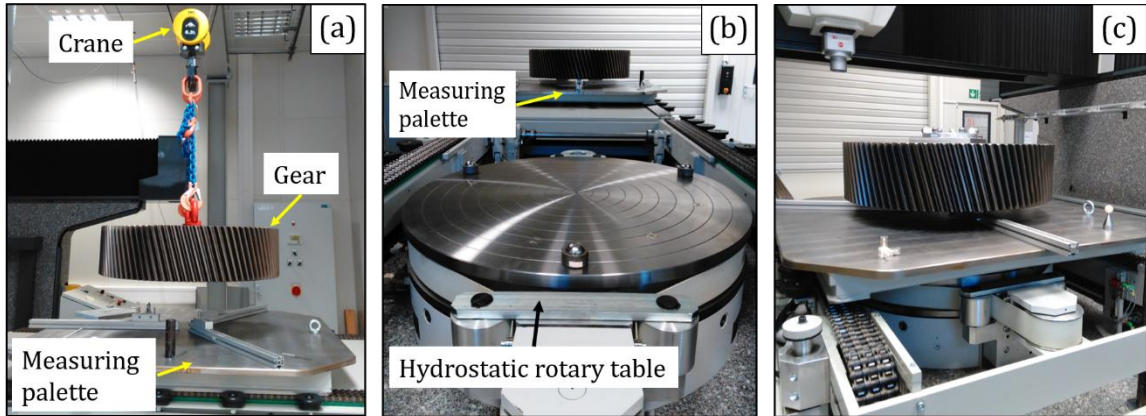


Figure 5.1. Loading procedure of a heavy gear onto hydrostatic RT: (a) preparation and placement of a helical gear on a measuring palette using traveling overhead crane (b) transportation of the measuring palette from loading gate to RT, with three hemisphere gate components for kinematic coupling (c) loading the measuring palette on RT.

5.1.2 Aerostatic RTs

For 4-axis CMMs, the RTs can be installed in three different ways: (i) embedded into the granite floor; (ii) fixed on the granite floor; (iii) fixed on a removable frame.

The first configuration is very common for small and mid-size CMMs, because it offers the maximum measuring volume. For large CMMs, considerable efforts are needed to build the foundation. Especially, additional space below the granite floor must be created without affecting the damping system of the whole device.

4-axis CMM at Physikalisch-Technische Bundesanstalt (PTB) consisted of a Leitz PMMG 50.40.20 (CMM B) and a Zollern aerostatic RT (RT B) (Figure 5.2). It adopted the third configuration at building the 4-axis CMM. The RT was placed on a 0.5 m high Strothmann steel frame. If necessary, the steel frame together with the RT can be lifted by a jack and transported to the adjacent climate-controlled storage room.

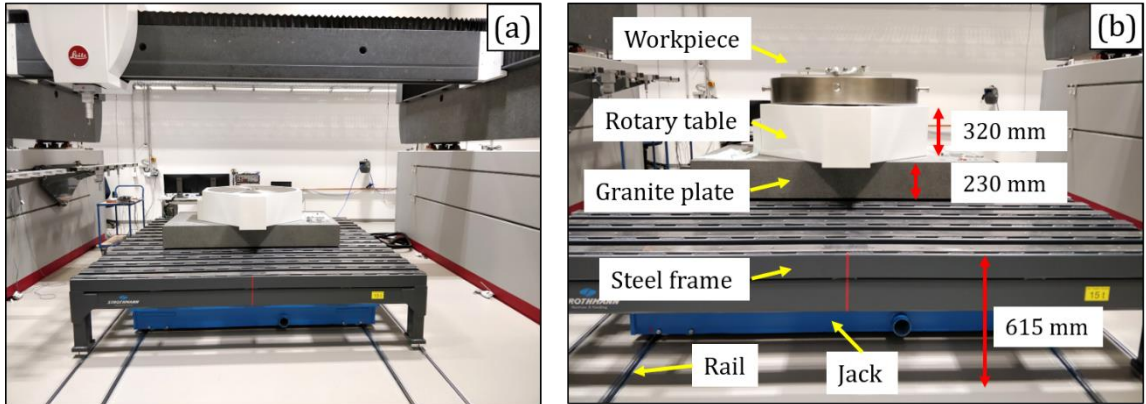


Figure 5.2. Configuration of 4-axis CMM at PTB.

The second configuration is the easiest way to add a RT, at the expense of reducing the measuring volumes. The RT and workpiece delivery system at BIMAQ also reduced the usable z range to 0.700 m. At UNC Charlotte, a Zollern ZART 1200.0390.0 aerostatic RT (RT C) was placed at near the center of the measuring volume of a Leitz PMM-F 30.20.16 (CMM C) (Figure 5.3(a)). The $\varnothing 1.200\text{ m} \times 0.440\text{ m}$ aerostatic RT reduced the usable z range at the central space of the CMM from 1.600 m to 1.160 m.

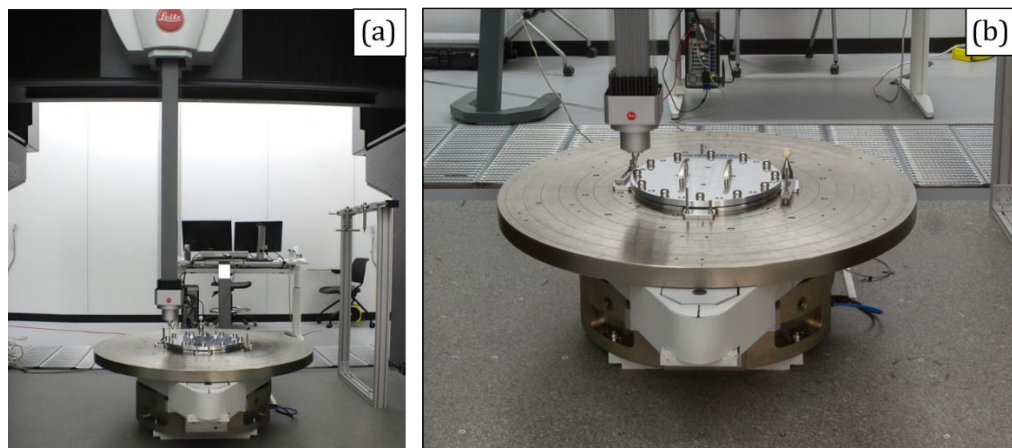


Figure 5.3. Configuration of 4-axis CMM at UNC Charlotte: (a) Leitz PMM-F 30.20.16 (b) Zollern ZART 1200.0390.0 aerostatic RT.

5.2 Experimental setups

5.2.1 Experimental setup for the RT A

In the first set of experiments, five symmetric loads up to $F = 33.8$ kN were designed (Figure 5.4): (1) non-load; (2) palette only; (3) palette and a helical external gear as measuring object; (4) palette, a helical gear and 4 spur gears as additional load; (5) palette, a helical gear and 8 spur gears. From case 3 to case 5, multiple points were measured on the top lands of gears to determine the coordinates of their gravity centers. Then, the overall eccentricities were calculated. Since the eccentricities were less than 5.0 mm, the RT was considered as symmetrically loaded.

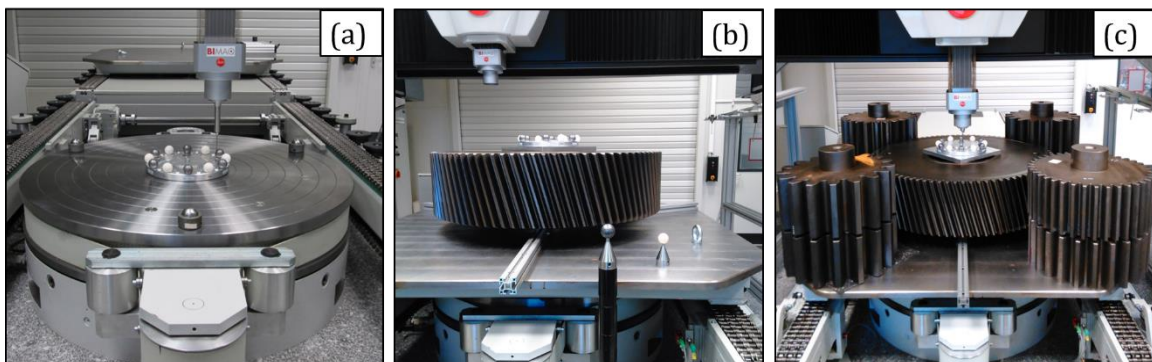


Figure 5.4. Experimental setup for RT under symmetric loads: (a) case 1: non-load (b) case 3: measuring palette and a helical ring gear (c) case 5: palette, a helical ring gear and 8 spur gears as additional load.

The CBP artifact consisted of a base plate, 6 tungsten carbide spheres and 6 ceramic spheres (Figure 4.1). The base plate had a tapered hole at the center, which matched the shape and size of a cylindrical fixturing component. In case 1 and 2 of symmetrically loading experiments, the artifact was fixed on the RT or the measuring palette, respectively. Figure 5.5 illustrates how the artifact was clamped on the measuring palette.

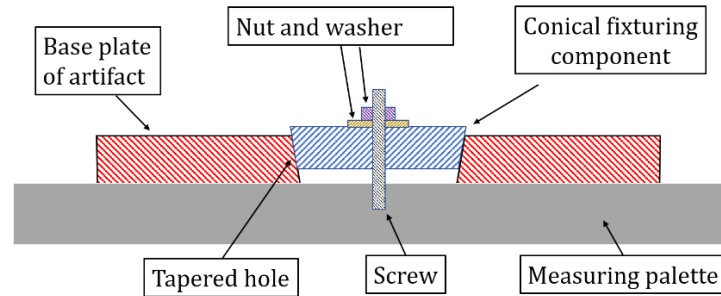


Figure 5.5. Schematic of clamping method for the artifact on measuring palette.

In the other cases, the artifact was moved up to the top of the helical gear for good accessibility. However, the artifact had a smaller diameter than the inner cylindrical surface of the gear. To solve this problem, the artifact was put on a rectangular plate, which was placed on top of the gear (Figure 5.6).

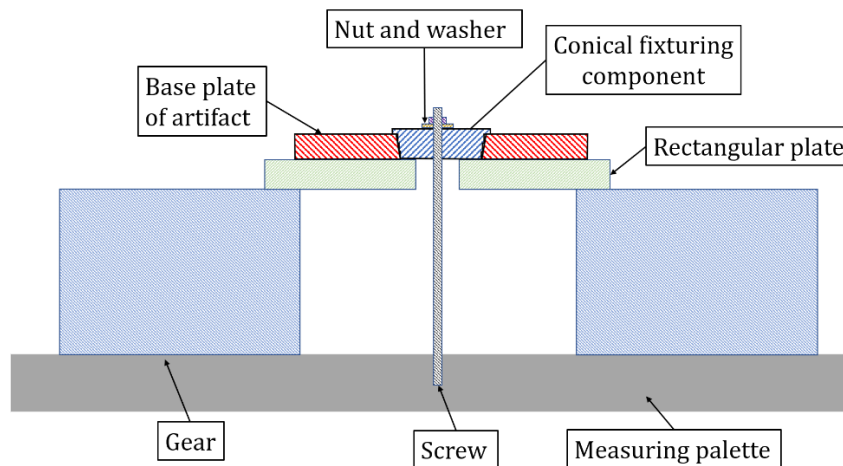


Figure 5.6. Schematic of clamping method for artifact on top of helical gear.

5.2.2 Experimental setup for the RT B

The error motions under no load, 1 ton and 2 ton of symmetric loads were studied. For the no load case, the ball plate was clamped directed onto the RT. For the other two cases, 1-ton steel disks were used to create symmetric loads. Because no hole exists on the

top side of the 1-ton reference disks, a solution was needed to fix the CBP. Three white rectangular steel plates were placed on top of the disk. The longer sides of plates were oriented along the radial direction and adjusted properly to avoid changing of the symmetric loads. Because the total mass of the three plates is less than 100 kg, the added load to the existing load were neglected in following discussion. The three plates sit on top of the disk stably regardless of the movement of RT. Then, the CBP was clamped on top of the white plates (see Figure 5.7(d)).

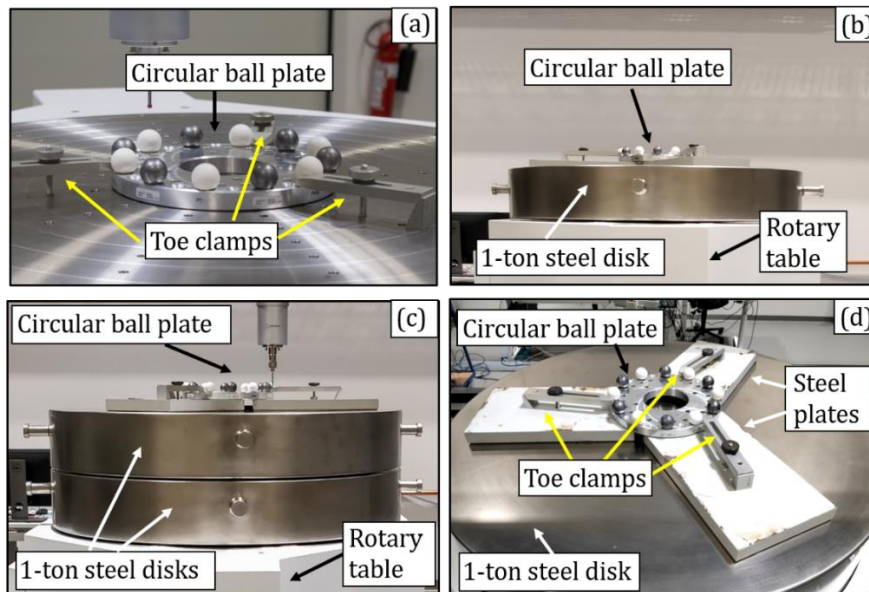


Figure 5.7. Experimental setups to identify the error motions of RT under symmetric loads: (a) no load (b) 1 ton (c) 2 tons (d) the CBP fixed on top of steel disk in (b) and (c) with help of toe clamps and steel plates.

5.2.3 Experimental setup for the RT C

14 raw steel slugs were used to create ring shape loads for the RT C at UNC Charlotte. 10 of them had diameters of 140 mm, with masses between 43.6 kg and 45.0 kg. the other 4 slugs had larger diameters of 190 mm, with masses between 54.6 kg and

57.8 kg. The total mass of 666.2 kg exceeds 50% of the maximum load. As shown in Figure 5.8 (d)-(f), the CBP artifact is centered on the RT. 16 nominal positions for the steel slugs are evenly distributed on a $\varnothing 900$ mm circle, with a nominal angular step of 22.5° . Four levels of symmetric loads were created: (1) no load; (2) 224.6 kg; (3) 489.2 kg; (4) 666.2 kg. The load distribution from the #2 to #4 cases are demonstrated in Figure 5.8.

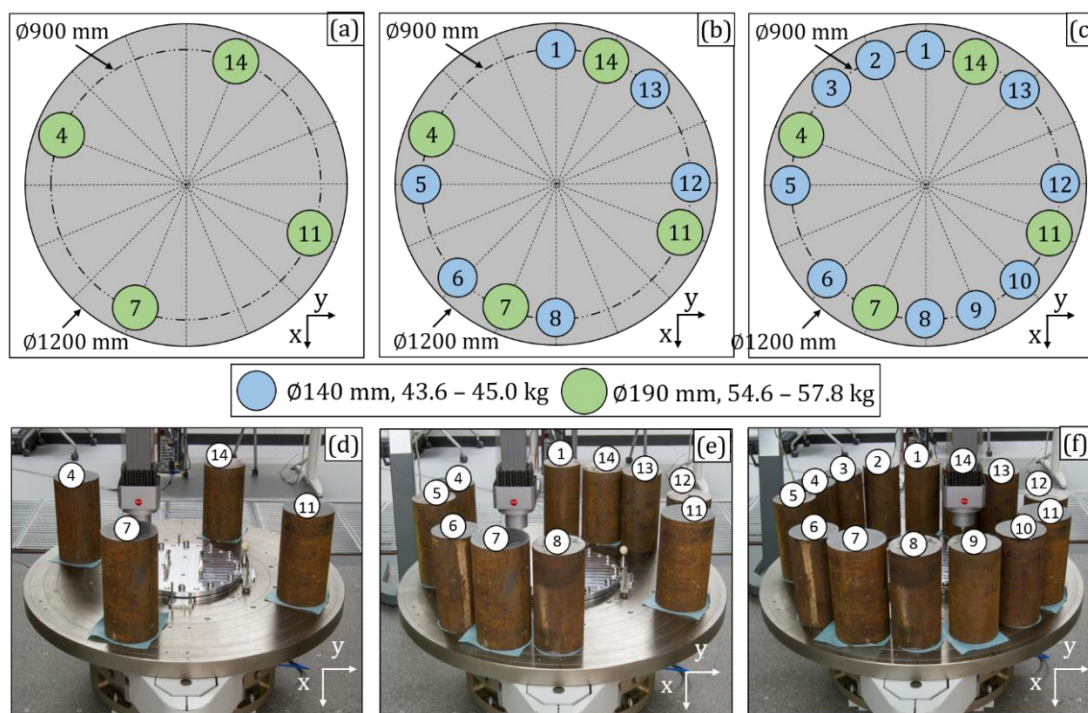


Figure 5.8. Distribution of loads on the RT C at UNC Charlotte: (a), (d) 224.6 kg symmetric load (b), (e) 489.2 kg symmetric load (c), (f) 666.2 kg symmetric load.

In the #4 case, the slugs occupied 14 out of 16 nominal positions, leaving 2 spots unused. Each pair of slugs with similar masses were placed diagonally, in order to create symmetric loads. The detail arrangements are demonstrated in Figure 5.8 (a) to (c). The x and y coordinates of slugs were determined by measuring circles on the cylindrical surfaces. Because the slug was not machined, several hundred micrometer form deviations

of the measured circles were observed. The trial and error method was used to lower the position deviations of slug centers to less than 0.5 mm. The coordinates of each slug is listed in Table 5.1. The gravity centers of loads in four cases are summarized in Table 5.2. With one-digit millimeter eccentricity, all four cases were considered as symmetric loads.

Table 5.1. Mass and position deviations of steel slugs (symmetric loads). The coordinates of the #6, #7 and #8 slugs in load case #4 were different from the ones in the load cases #2 and #3 (see Table 5.2).

#	Mass (kg)	Nominal Position		Actual Position (mm)		Form deviation (mm)	Case			
		x (mm)	y (mm)	x dev. (mm)	y dev. (mm)		# 1	# 2	# 3	# 4
1	44.2	-450.000	0.000	-0.224	-0.182	0.235			•	•
2	45.0	-415.749	-172.208	-0.106	0.245	0.524				•
3	44.2	-318.198	-318.198	0.113	-0.043	0.304				•
4	56.0	-172.208	-415.746	-0.011	0.071	0.192		•	•	•
5	43.8	-0.000	-450.000	-0.205	0.249	0.612			•	•
6	43.6	318.198	-318.198	-0.255	-0.377	-			•	
6*	43.6	318.198	-318.198	0.235	0.094	0.467				•
7	57.8	415.746	-172.208	-0.384	0.187	-		•	•	
7*	57.8	415.746	-172.208	0.016	0.337	0.283				•
8	44.6	450.000	-0.000	-0.086	-0.268	-			•	
8*	44.6	450.000	-0.000	0.181	0.146	0.505				•
9	43.6	415.749	172.208	0.079	0.113	0.404				•
10	44.2	318.198	318.198	-0.109	-0.148	0.284				•
11	56.2	172.208	415.746	-0.065	0.338	0.320		•	•	•
12	44.4	0.000	450.000	-0.228	-0.186	0.241			•	•
13	44.0	-318.198	318.198	-0.152	0.118	0.219			•	•
14	54.6	-415.746	172.208	0.333	-0.107	0.220		•	•	•

Table 5.2. Gravity centers of loads.

Case	Load (kg)	Gravity center of load	
		x (mm)	y (mm)
#1	0	0.000	0.000
#2	224.6	6.040	-1.959
#3	489.2	2.777	0.146
#4	666.2	1.164	-0.458

5.2.4 Reference point

In experiment setups for the RT A, the artifact was positioned at three different heights (see Figure 5.9). The center of the approximated workpiece coordinate system at the #3 position was defined as the reference point. Separated error motions of case 1 and case 2 were transformed to the reference point to be compared with results of the other cases. δ_x and δ_y were recalculated according to Equation 5.1:

$$\begin{bmatrix} \delta_x \\ \delta_y \end{bmatrix}_{AW,new} = \begin{bmatrix} \delta_x \\ \delta_y \end{bmatrix}_{AW} + H_c \begin{bmatrix} \varepsilon_y \\ -\varepsilon_x \end{bmatrix}_{AW} \quad (5.1)$$

H_c was the height difference between the #1 (or #2) position and the #3 position of the artifact. Subscript AW denoted the approximated workpiece coordinate system (WCS) at the #1 or #2 position. Subscript AW, new denoted the transformed approximated WCS.

For the RT B and RT C experiments, the centers of the approximated workpiece coordinate system at no load cases were set as the reference points.

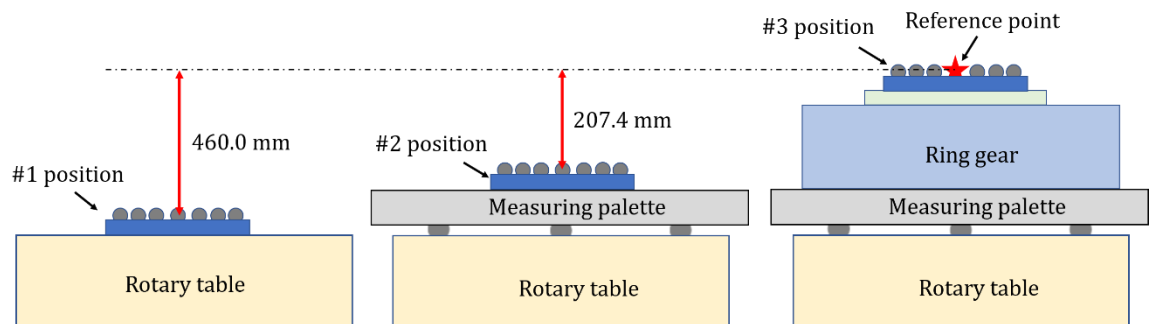


Figure 5.9. Illustration of three artifact positions in the experiments, with a reference point defined as the center of approximated workpiece coordinate system at the #3 position.

5.3. Calibration procedure

5.3.1 Warm up procedure

In all experiments performed with the RT A, the RT A was rotated by four cycles in the counter-clock-wise (CCW) direction in steps of 7.5° . At each step, 15 points were probed on every tungsten carbide sphere (#1, #3, #5, #7, #9 and #11).

Figure 5.10 demonstrates measured z coordinates of six sphere centers in four cycles. As a uniform warm-up routine was not found and executed before the experiments, the RT took the first cycle to reach a stable operating condition. Therefore, only data from cycle 2 to cycle 4 was used for analysis.

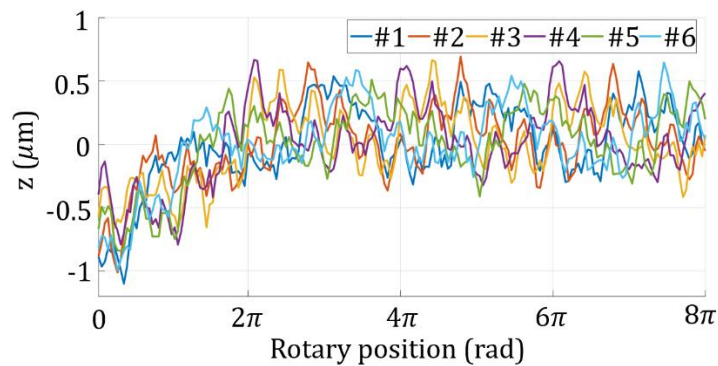


Figure 5.10. Measured z coordinates of six sphere centers in four cycles in non-load case. No warm-up routine was executed.

In all experiments performed with the RT B, the RT B was rotated by 6 cycles in the CCW direction first. Then, it was rotated back in the CW direction to the original position. The angular step was 10° ($M = 36$). In a similar way, the RT C was rotated by 8 cycles in the CCW direction first and 8 cycles in the CW direction then. The angular step was set to 7.5° ($M = 48$).

5.3.2 CMM deviations

The systematic components of geometric deviations of the CMM A (BIMAQ) and CMM B (PTB) were identified by the proposed data processing method (Section 2.4.3). The dots on dash-dot curves in Figure 5.11 represent the separated systematic components of geometric deviations of CMM B at 48 measuring positions at three heights. In Figure 5.11(a), each dash-dot curve has six peaks and six valleys.

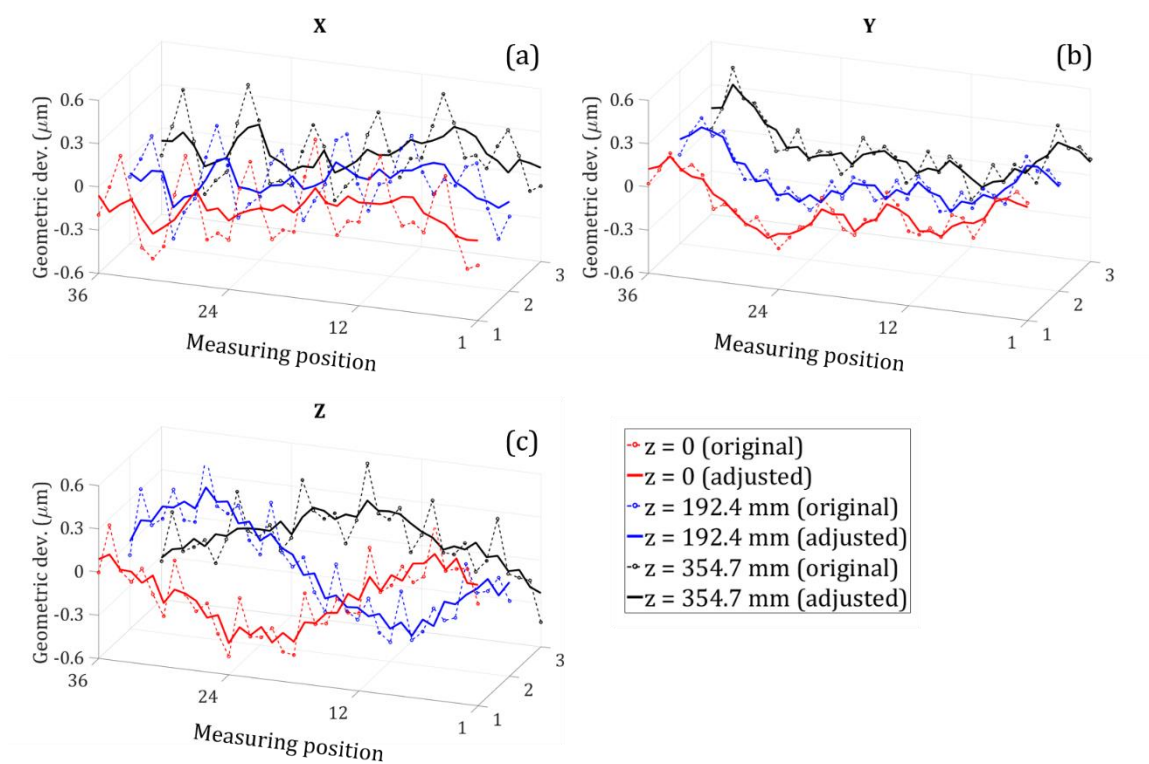


Figure 5.11. Original and adjusted geometric deviations of CMM B at 48 measuring positions at three heights: (a) x deviations (b) y deviation (c) z deviations.

As discussed in Section 2.4.1, the 3-axis CMM was assumed to perform consistently such that the probe returned the same position following a closed loop.

Therefore, the accumulative deviations of the CMM along the closed x, y and z paths equal to zeros, respectively (Equation 5.2).

$$\begin{bmatrix} \sum_{k=1}^M \Delta x_{gs(k)} \\ \sum_{k=1}^M \Delta y_{gs(k)} \\ \sum_{k=1}^M \Delta z_{gs(k)} \end{bmatrix} = \begin{bmatrix} 0 \\ 0 \\ 0 \end{bmatrix} \quad (5.2)$$

The $\Delta x_{gs(k)}$ ($k = 1, 2, \dots, M$) was represented by a trigonometric polynomial with a period of 2π (Equation 5.3).

$$F_{\Delta x_{gs}} = \sum_{n=1}^{N_1} [a_n \cos(n\theta + \varphi_n)] \quad (5.3)$$

The $\Delta x_{gs(k)}$ ($k = 1, 2, \dots, M$) was processed with fast Fourier transformation (FFT) to decompose the coefficient a_n (amplitude) and phase φ_n of all polynomial components in Equation 5.3.

To understand the observed phenomenon in Figure 5.11, the $\Delta x_{gs(k)}$ at three heights in Figure 5.11(a) were processed by FFT. Because the number of rotary positions M was equal to 36 for CMM B, degree $N_1 = 17$ polynomials were decomposed. In a similar way, the $\Delta y_{gs(k)}$ at three heights in Figure 5.11(b) and the $\Delta z_{gs(k)}$ at three heights in Figure 5.11(c) were processed. The amplitudes of polynomial components are shown in Figure 5.12. In each of three subplots, the coefficients a_6 and a_{12} in were much larger than the adjacent terms, respectively.

Because the number of spheres N was equal to 6, the coefficients a_6 and a_{12} contained the components from the CMM and the error motions. Unfortunately, without an additional technique, the percentages of separated a_6 and a_{12} originating from the CMM B cannot be quantified. In Figure 5.12, it is likely that the a_6 and a_{12} was primarily affected by the error motions of rotary table rather than the geometric deviations of

CMM B. Hence, the a_6 and a_{12} terms for the CMM B were set to zero. The adjusted results are represented by the solid lines in Figure 5.11. The X components of the CMM deviations at three heights were comparable, so as the Y components.

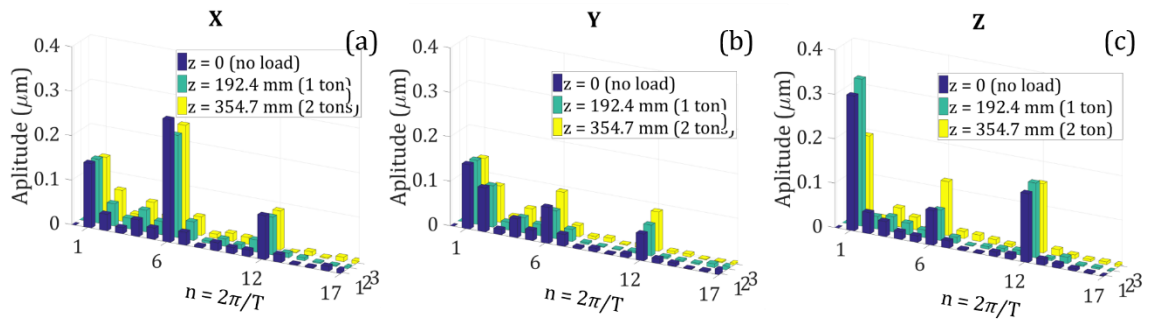


Figure 5.12. Amplitudes of polynomial components for CMM B's geometric deviations at three heights: (a) x deviations (b) y deviations (c) z deviations.

In a similar way, the systematic components of geometric deviations of the CMM A (BIMAQ) were processed. Because M was equal to 48 for CMM A, degree $N_1 = 23$ were decomposed respectively. Figure 5.13 shows the amplitudes of all polynomial components. a_6 , a_{12} and a_{18} were set to zero. The original and compensated deviations of CMM A at 48 measuring positions at three heights are shown in Figure 5.14.

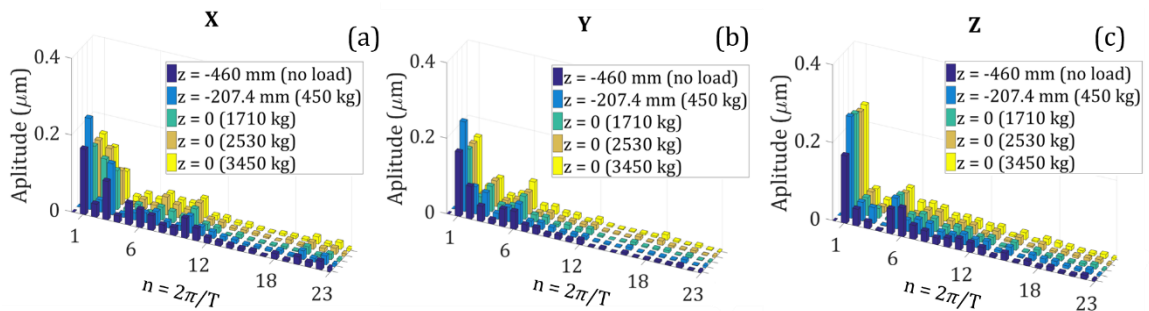


Figure 5.13. Amplitudes of polynomial components for CMM A's geometric deviations in five cases: (a) x deviations (b) y deviations (c) z deviations.

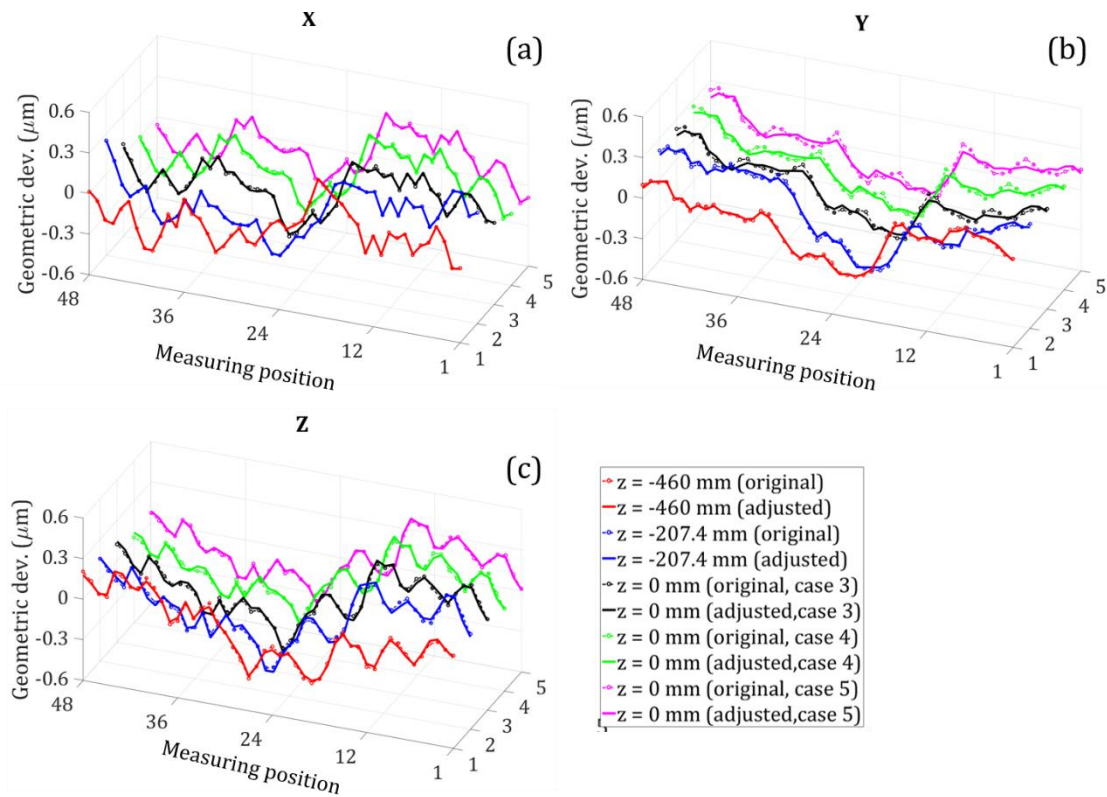


Figure 5.14 Original and adjusted geometric deviations of CMM A at 48 measuring positions in five cases: (a) x deviations (b) y deviation (c) z deviations.

5.4 Experimental results

5.4.1 RT A

Figure 5.15 shows the approximated error motions in symmetric load cases from no load to 3.45 ton. In most metrology tasks, the measuring palette is loaded onto the RT together with the workpiece. Case 2 to case 5 led to similar ε_x , ε_y and ε_z , which showed that changing values of symmetric loads had negligible influence on the tilt error motions and angular positioning deviations of the RT. The error motions of the non-load case were different from the ones of other cases.

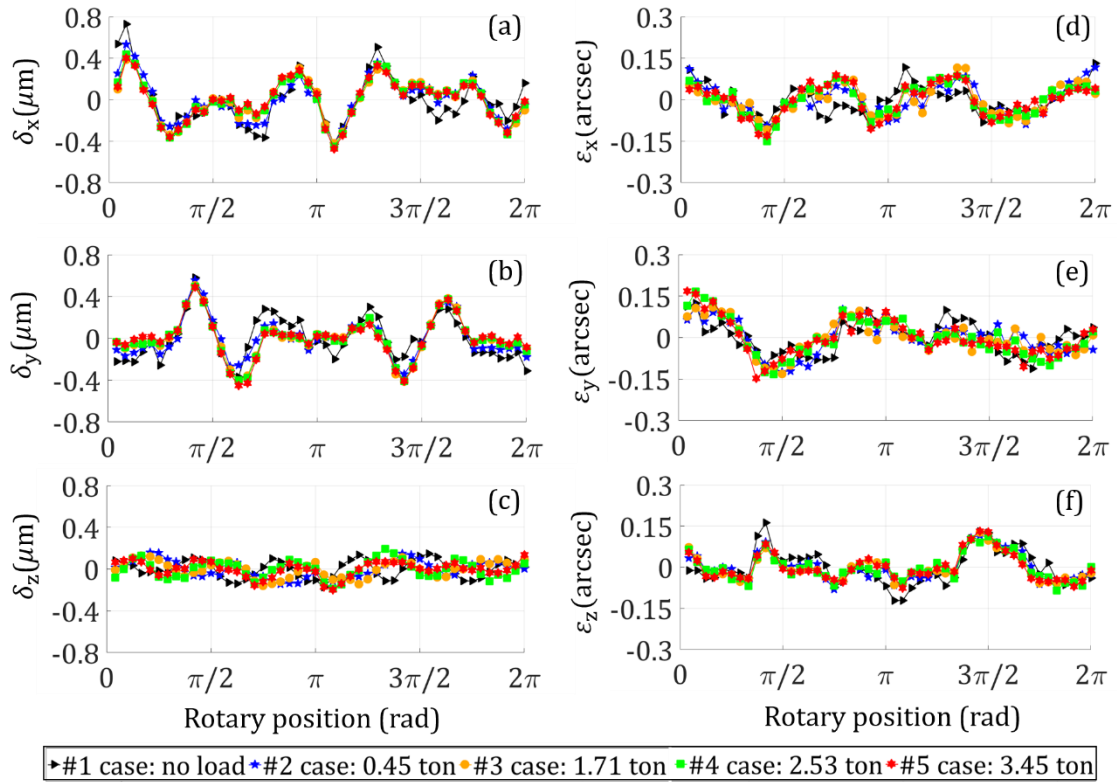


Figure 5.15. Separated error motions of a hydrostatic RT under symmetric loads from no load to 3.45 ton: (a) δ_x (b) δ_y (c) δ_z (d) ε_x (e) ε_y (f) ε_z .

This RT had consistent δ_x and δ_y from medium load (case 3) to heavy load (case 5). However, δ_x and δ_y under no load were different from heavy loads. Because δ_z was not repeatable in multiple cycles, the approximated curves in the five cases are different.

All error motions except δ_z had periods of 2π in the no load case. δ_z did not have a fully repeatable pattern in three cycles, which may result from the thickness variation of the oil film used for the hydrostatic bearing, because temperature control of an oil film in a closed system was very challenging. Similar phenomena existed in the other tested loading scenarios.

5.4.2 RT B

The periods of all six error motions were 2π . Although the amplitudes of error motions were higher than those of RT A, the four-axis deviation of the CMM was still within acceptance range. As shown in Figure 5.16, the RT B had comparable δ_x , δ_y , δ_z and ε_z in three levels of symmetric loads. For ε_x and ε_y , there were noticeable differences among the three cases. The curves of the 1 ton case were in between the curves of no load and 2 ton cases.

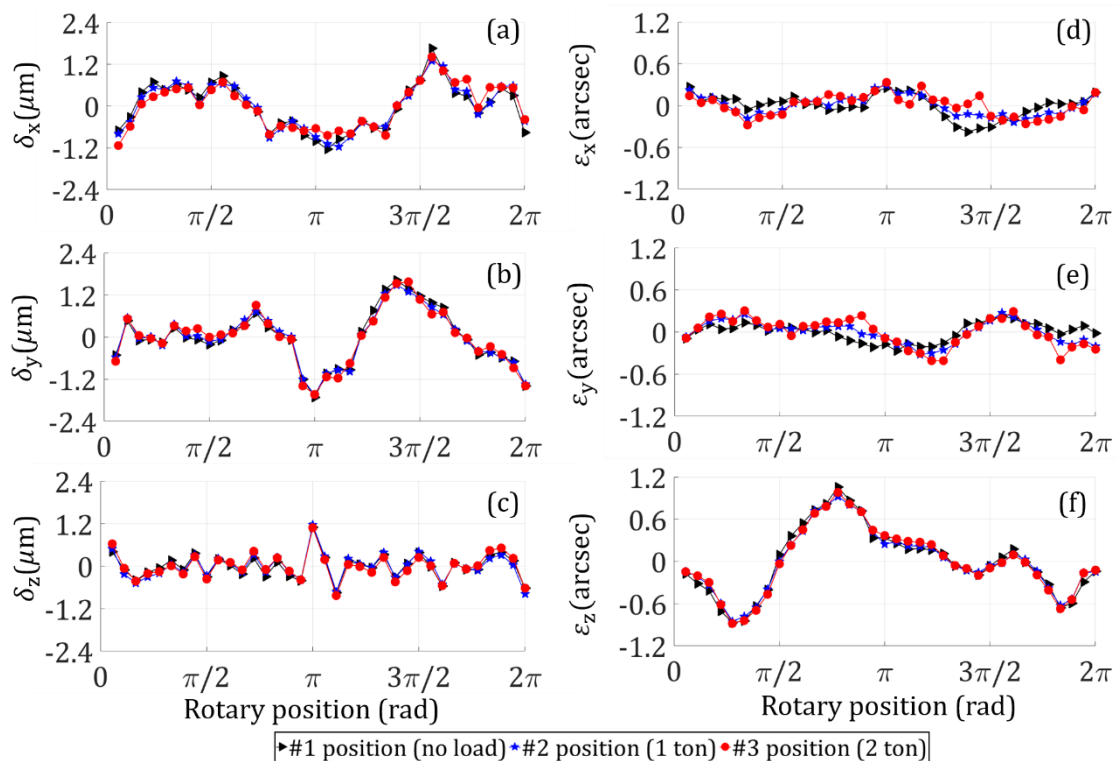


Figure 5.16. Six error motions of the rotary table B under three levels of symmetric loads: (a) δ_x (b) δ_y (c) δ_z (d) ε_x (e) ε_y (f) ε_z .

5.4.3 RT C

The separated error motions of the RT C under four levels of symmetric loads are presented in Figure 5.17 and Figure 5.18. Compared with the error motions of the RT A,

the RT C had larger δ_x and smaller δ_y . The amplitudes of the other error motions were at the same levels of the RT A.

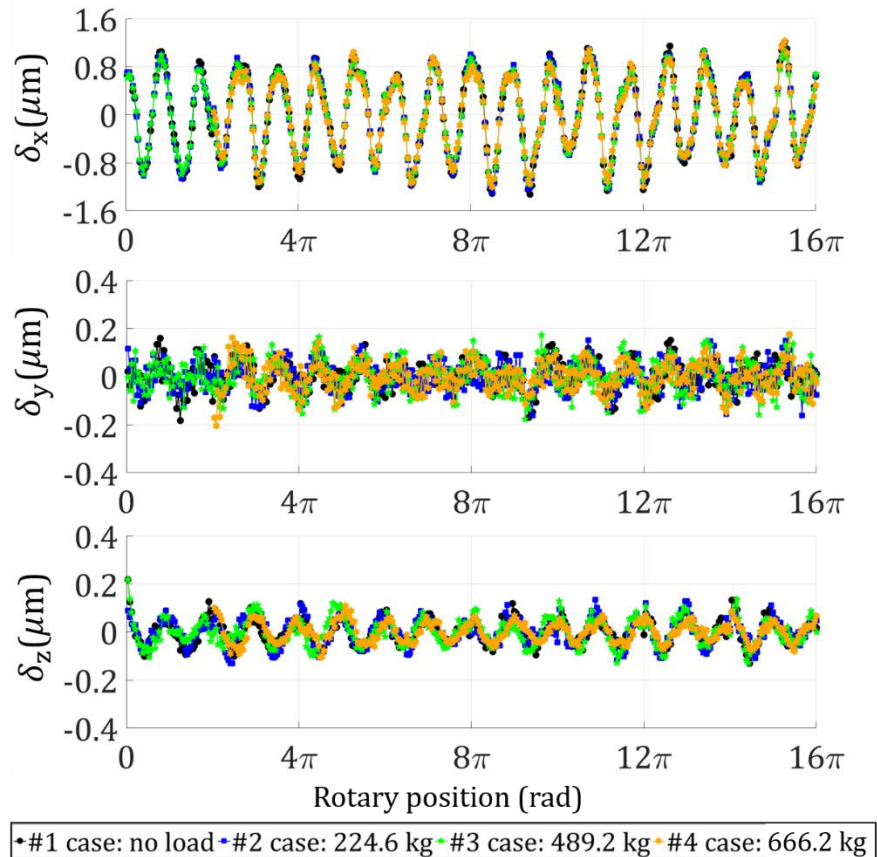


Figure 5.17. Separated δ_x , δ_y and δ_z of the rotary table C under four levels of symmetric loads.

The periods of all error motions were not changed. The amplitude of ε_y had negative correlation with the load value. Namely, higher symmetric loads lead to lower wobbling of the rotary table. Nevertheless, the amplitude of ε_y were small enough that ε_y was negligible. The other error motions were not influenced by the load value. Therefore, the error motion calibrated under no load case can be used for error mapping in symmetric loading cases.

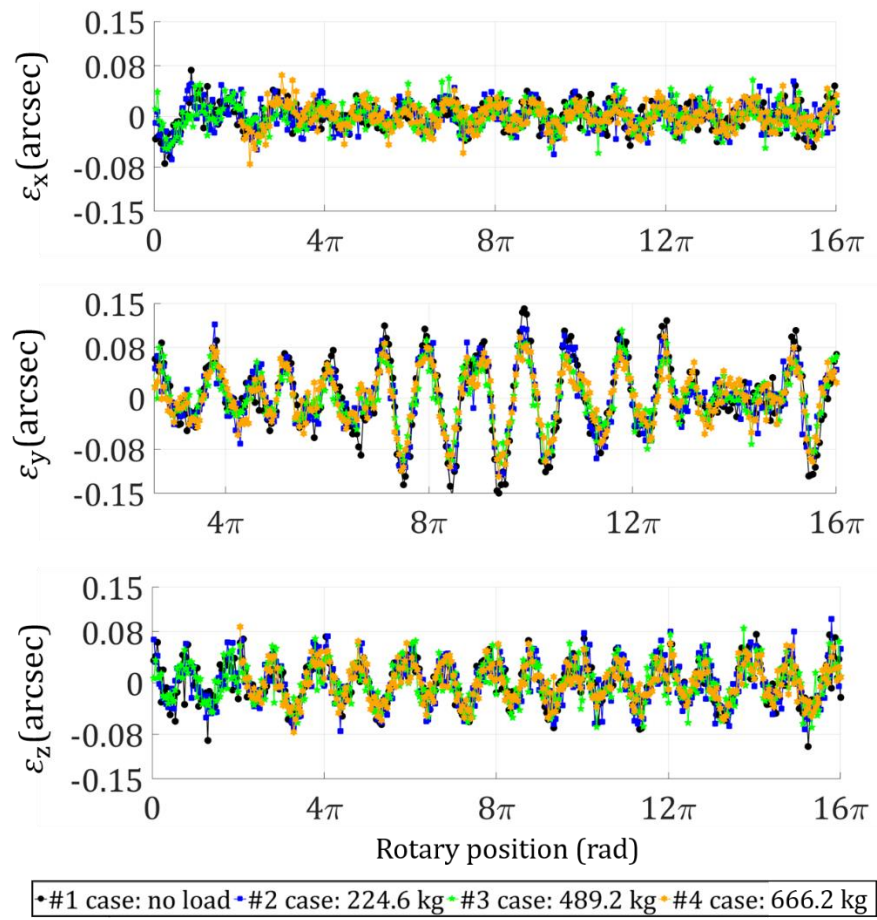


Figure 5.18. Separated ε_x , ε_y and ε_z of the RT C under four levels of symmetric loads.

CHAPTER 6: ROTARY TABLE UNDER ASYMMETRIC LOADS

6.1 Experimental setups

6.1.1 Weak asymmetric loads for RT A

For weak asymmetric loads, the ring gear was shifted off-center intentionally to create seven slight asymmetric loading cases. These sets of experiments mimicked measuring tasks, where positioning accuracies of heavy parts were limited.

Figure 6.1 illustrates the positioning process of a helical ring gear. The gear was placed on the blocks of three linear motions guides, which were fixed on the measuring palette. Three short pins inserted into the blocks had contact with the inner cylindrical surface of the gear. By calculating and adjusting the position of the short pins and blocks before loading the ring gear, the eccentricity value of the ring gear can be set. The inner cylindrical surface was measured to calculate the overall eccentricity.

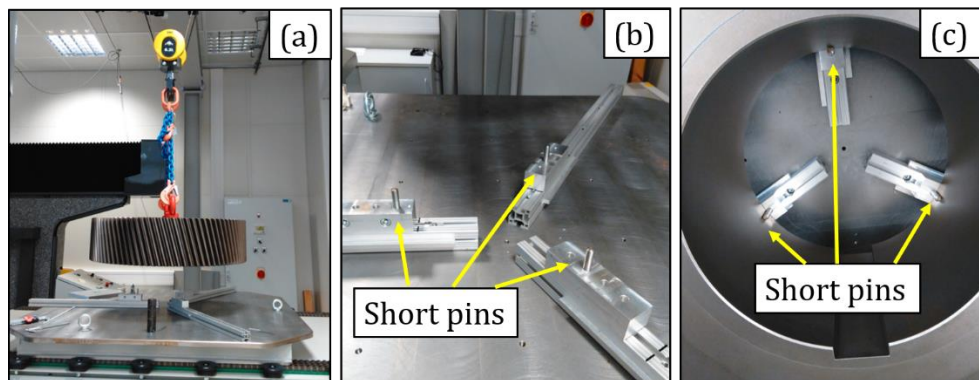


Figure 6.1. Experimental setup for RT under weak asymmetric loads: (a) loading the ring gear onto the linear motion guides; (b) three linear motion guides and accessories; (c) preset the positions of three blocks and three short pins to constraint the position of the gear.

6.1.2 Asymmetric loads for the RT C

In Chapter 5, steel slugs were used to create five symmetrical loading scenarios. The case 1 with 14 steel slugs was used as the reference for asymmetric load scenarios (Figure 6.2(a)). In case 2, the #8 slug was removed while the positions of the other slugs were unchanged (Figure 6.2(b)). The gravity center of all the loads shifted from the center of RT C towards the #1 slug, which was placed radially opposite to the original place of #8 slug. The 13 slugs were almost symmetrically loaded with respect to the x-axis.

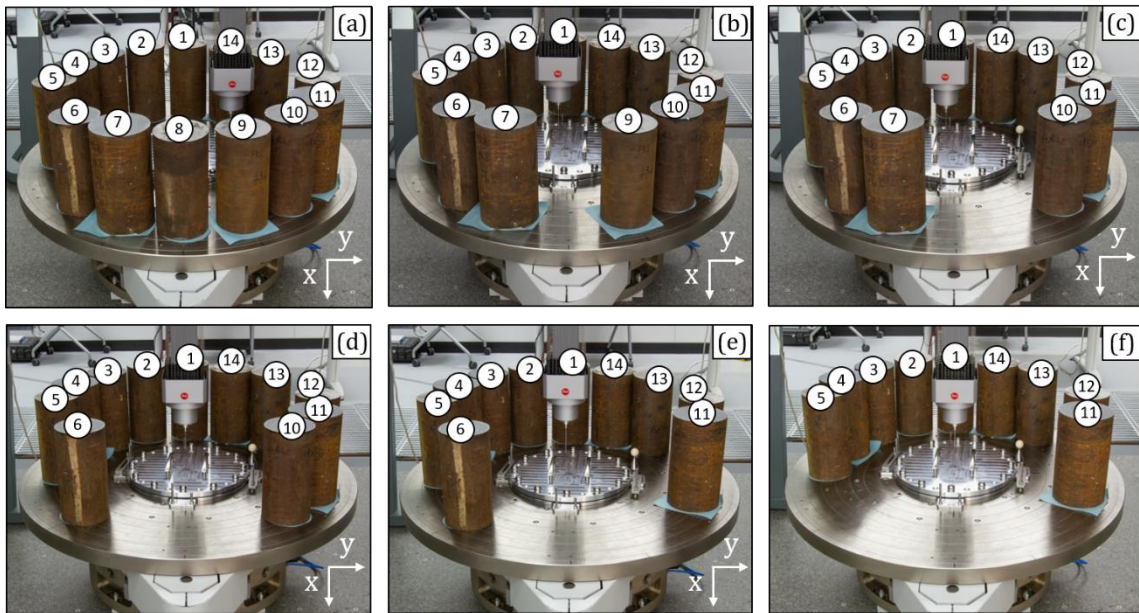


Figure 6.2. Asymmetric loading cases for the RT C: (a) case 1 (reference case, symmetric load) (b) case 2 (c) case 3 (d) case 4 (e) case 5 (f) case 6.

As shown in Figure 6.2 (c) - (f), in each of case 3 to case 6, one slug was removed from the RT. The total load and torque were standardized relative to $m_{\max} = 666.2 \text{ kg}$ and $m_{\max}gR_0 = 2937.942 \text{ Nm}$, respectively (Table 6.1). Here, the nominal radial position R_0 of each slug was equal to 450 mm. In Table 6.1, angle ξ describes the angular position of a gravity center with respect to the +x direction of the frame CS.

Table 6.1. Load values and gravity centers for asymmetric loads.

Case #	Result			Standardized result		
	Load (kg)	Gravity center		Load	Torque	Angle ξ ($^\circ$)
		x (mm)	y (mm)			
1	666.2	1.2486	-0.3861	1.0000	0.0029	-17.1815
2	621.6	-30.9625	-0.4242	0.9331	0.0642	-179.2150
3	578.0	-64.6648	-13.4548	0.8676	0.1273	-168.2462
4	520.2	-118.0456	4.1469	0.7808	0.2050	177.9880
5	476.0	-158.5438	-25.0012	0.7145	0.2548	-171.0387
6	432.4	-206.6386	4.5531	0.6491	0.2981	178.7377

As shown in Figure 6.3(b), the total load dropped linearly from case 1 to case 6, but the gravity center was shifted away from the center of RT. As a comprehensive result of these two factors, the momentum increased linearly (Figure 6.3(c)).

Detailed information of the asymmetrically loading cases are given in Table 6.2 and Table 6.1.

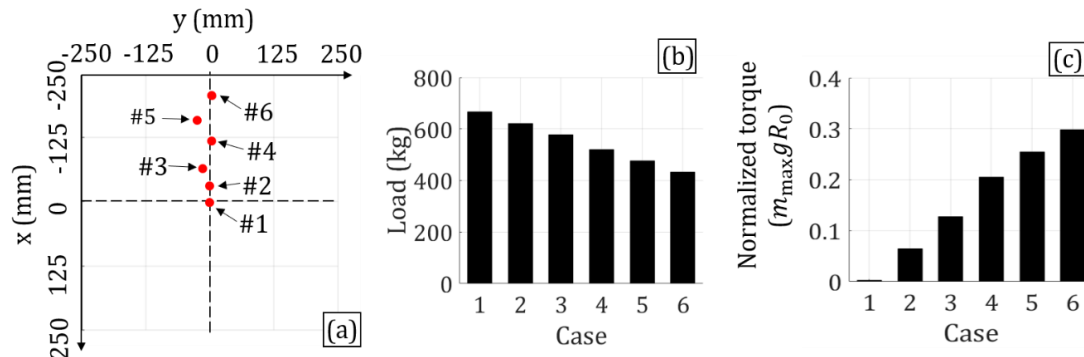


Figure 6.3. Asymmetric loading cases: (a) x and y coordinates of the gravity centers (b) load values (c) normalized torques.

Table 6.2. Mass and position deviations of steel slugs (asymmetric loads).

#	Mass (kg)	Nominal Position (mm)		Deviation (mm)		Case					
		x	y	x	y	Asymmetric load					
						1	2	3	4	5	6
1	44.2	-450.000	0.000	-0.224	-0.182	●	●	●	●	●	●
2	45.0	-415.749	-172.208	-0.106	0.245	●	●	●	●	●	●
3	44.2	-318.198	-318.198	0.113	-0.043	●	●	●	●	●	●
4	56.0	-172.208	-415.746	-0.011	0.071	●	●	●	●	●	●
5	43.8	-0.000	-450.000	-0.205	0.249	●	●	●	●	●	●
6	43.6	318.198	-318.198	0.235	0.094	●	●	●	●	●	
7	57.8	415.746	-172.208	0.016	0.337	●	●	●			
8	44.6	450.000	-0.000	0.181	0.146	●					
9	43.6	415.749	172.208	0.079	0.113	●	●				
10	44.2	318.198	318.198	-0.109	-0.148	●	●	●	●		
11	56.2	172.208	415.746	-0.065	0.338	●	●	●	●	●	●
12	44.4	0.000	450.000	-0.228	-0.186	●	●	●	●	●	●
13	44.0	-318.198	318.198	-0.152	0.118	●	●	●	●	●	●
14	54.6	-415.746	172.208	0.333	-0.107	●	●	●	●	●	●

6.2 Experimental results

6.2.1 Weak asymmetric loads for RT A

Figure 6.4. shows the approximated error motions in the asymmetric loading cases when 1.71 ton load was shifted along the x-axis from with eccentricity from $x = -10.80$ mm to $x = 10.00$ mm. No significant differences in all seven cases were found. This set of experiments confirmed that the performance of RT A was nearly not affected when a symmetric medium level load was placed with an eccentricity in the millimeter range. This is meaningful because the positioning accuracies of workpieces in many applications are limited due to their large size and heavy weight.

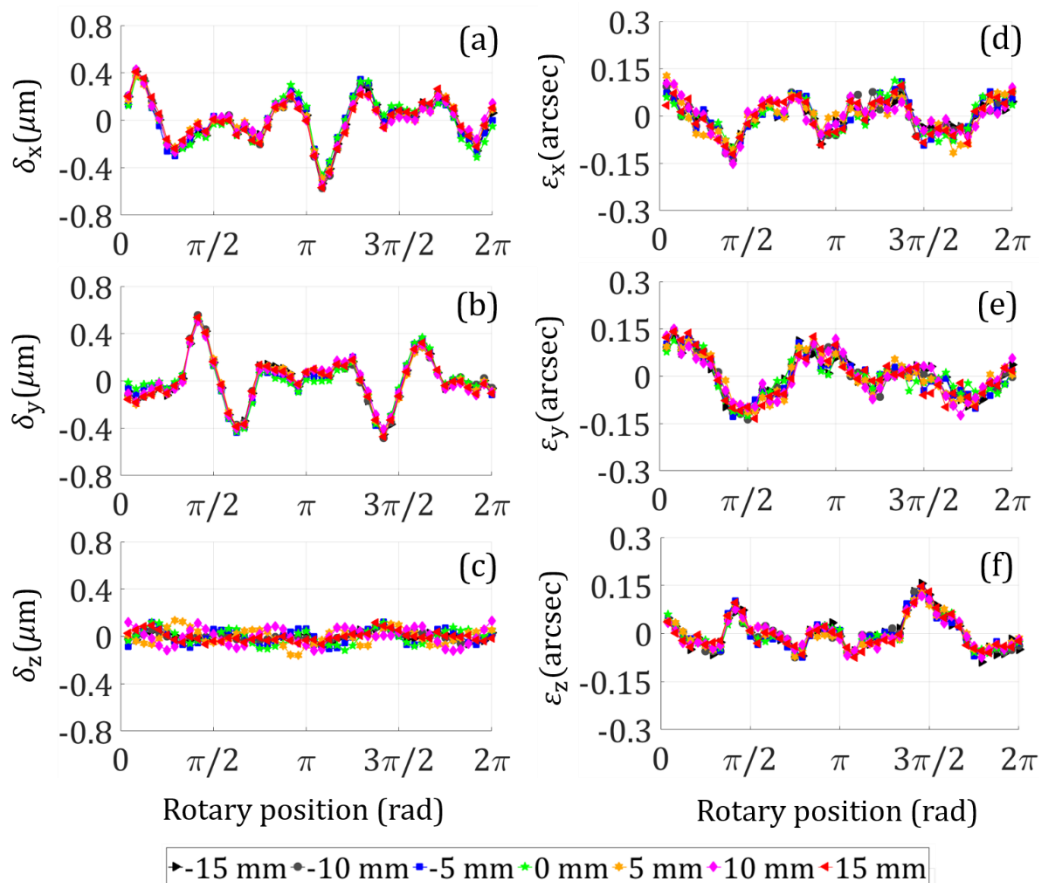


Figure 6.4. Separated error motions of a hydrostatic RT under seven asymmetric 1.7 tons loads: (a) δ_x (b) δ_y (c) δ_z (d) ε_x (e) ε_y (f) ε_z .

6.2.2 Asymmetric loads for the RT C

The separated error motions of the RT C under asymmetric loading cases are presented in Figure 6.5 and Figure 6.6. The δ_z increased when the standardized torque increased. The asymmetric loads changed the angle of the average axis of rotation. However, the tilt error motions were almost not influenced. The other error motions were constant in the tested cases.

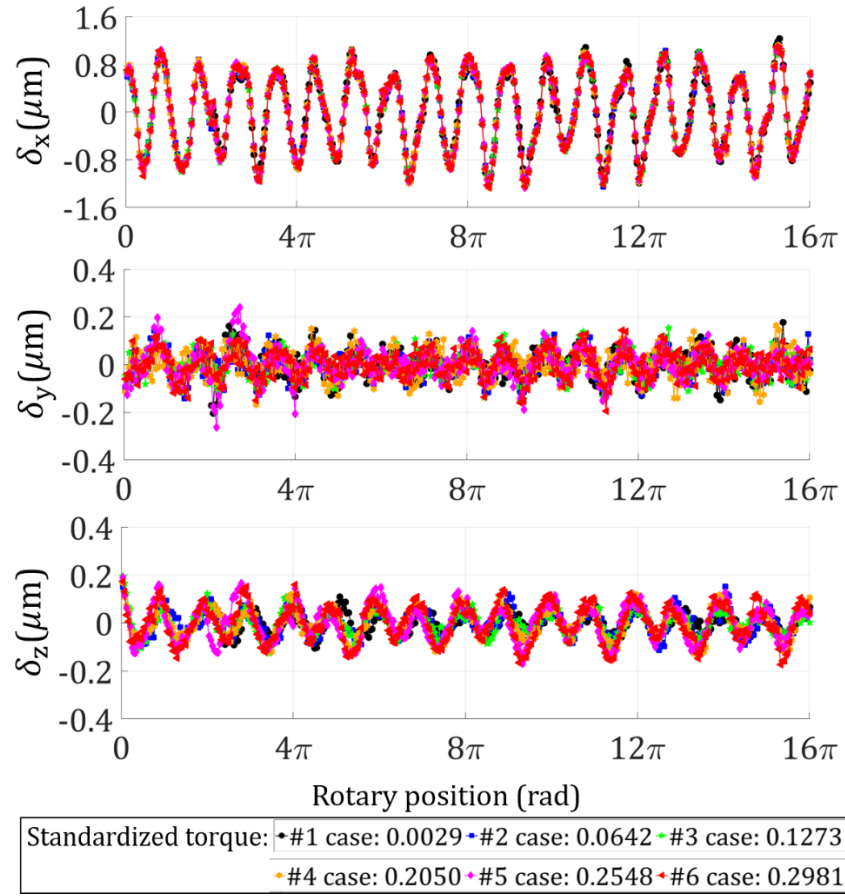


Figure 6.5. Separated δ_x , δ_y and δ_z of the RT C under asymmetric loads.

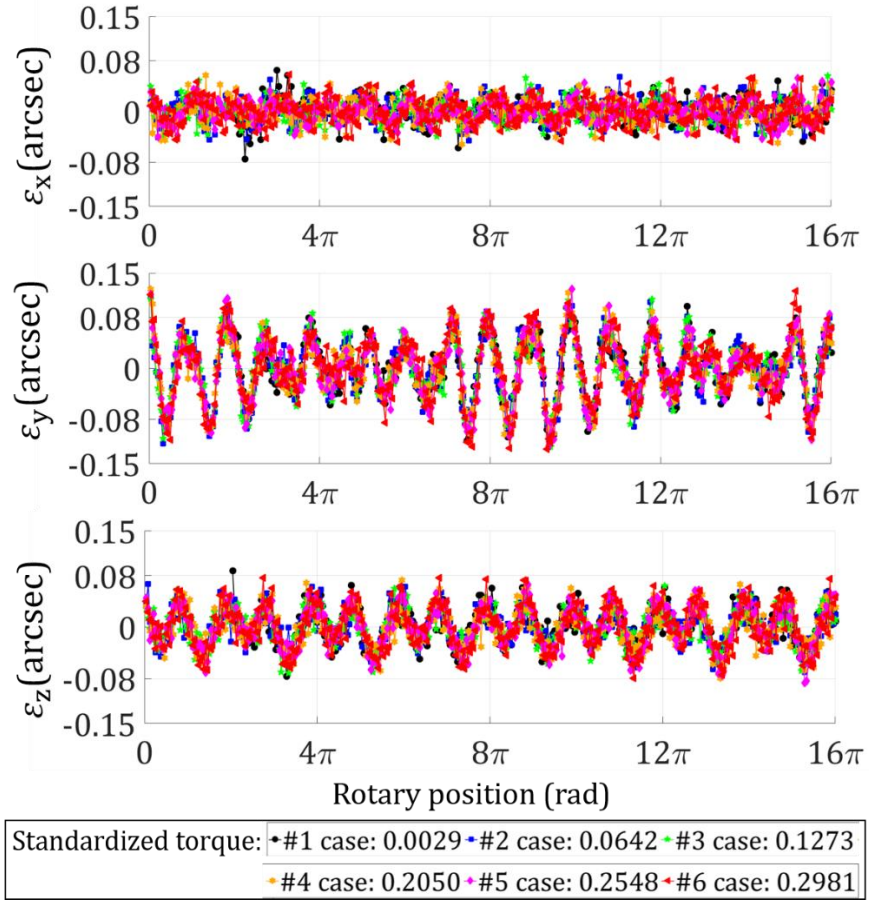


Figure 6.6. Separated ε_x , ε_y and ε_z of the RT C under asymmetric loads.

CHAPTER 7: SUMMARY

A new calibration technique was proposed to determine the six error motions of rotary tables of a 4-axis CMM. The CMM was used as the measuring device and a circular ball plate artifact was used as the artifact. The data processing technique can separate the deviations of CMM, the error motions of rotary table and the deviations of the artifact.

The experimental setup and a complete solution were proposed in Chapter 2. Based on a mathematical model, the data processing technique was discussed in detail.

Numerical simulation was carried out to validate the proposed solution in Chapter 3. Simulation inputs were generated from experimental data or proper assumptions based on product sheets. Numerical simulation proved that the proposed solution can separate the deviations of CMM, artifact and the rotary table. Monte Carlo simulation was performed to investigate how the separation of error motions were influenced by four key parameters, including the ball plate radius, number of spheres, number of measuring positions, CMM's random deviations. The influence of CMM's drift during the experiment was also investigated.

Experiments were performed to validate the proposed solution in Chapter 4. A circular ball plate was designed and built for the calibration of an aerostatic rotary table. The separated CMM's geometric deviations were comparable to results obtained with a ball step gage. The separated error motions were compared to results from a spindle error analyzer.

This rotary table calibration technique was applied to investigate the performances of one Zollern hydrostatic rotary table and two Zollern aerostatic rotary tables under

symmetric loads. The results showed that these three rotary table had consistent error motions under different levels of symmetric loads. In Chapter 6, the performances of the hydrostatic rotary table and one aerostatic rotary table under designed asymmetric loading scenarios were tested.

CHAPTER 8: FUTURE WORK

In this research, the proposed solution was validated via numerical simulation and experiments. It is promising to apply the technique in the production line of 4-axis CMM to calibrate the error motions of rotary table after the assembly phase. The separated error motions can be fed to the CMM for error compensation purpose. If the acceptance test of the 4-axis CMM following the ISO standard [20] reports lower deviations when the error compensation of rotary table is activated, the effectiveness of this technique is further validated.

A main shortcoming of this error mapping technique is the efficiency. Hence, reducing the time and thus also the cost is meaningful for future application. Hexagon Manufacturing Intelligence has released the HP-O optical sensor based on frequency-modulated interferometric optical distance measurement [57]. Hexagon claims that this sensor has high flexibility, high accuracy and high sampling rate (1000 Hz). Similar to tactile probe, HP-O sensor can determine the coordinates of a sphere (made of tungsten carbide) by sampling multiple points in single-point mode or scanning mode. It is promising that the efficiency of rotary table calibration can be significantly improved by using the HP-O sensor. More experiments are necessary to confirm the applicability.

The tested Zollern hydrostatic table has consistence performance under weak asymmetric loads. Next, more experiments should be designed and carried out to investigate the behavior of this table under heavy asymmetric loads.

REFERENCES

- [1] Goch, G., Knapp, W., & Härtig, F. (2012). Precision engineering for wind energy systems. *CIRP Annals*, 61(2), 611-634.
- [2] en.wikipedia.org/wiki/General_Electric_GE90. Retrieved 2019, July 19.
- [3] www.ge.com/reports/guinness-work-worlds-largest-aluminum-smelter-meets-worlds-efficient-gas-turbine. Retrieved 2019, July 19.
- [4] www.wikov.com/en/mechanical-gearboxes/according-to-application/wind-and-tidal. Retrieved 2019, July 19.
- [5] www.reddit.com/r/MachinePorn/comments/20e8sx/ships_gearbox_29282082. Retrieved 2019, July 19.
- [6] autowpaper.com/bugatti-veyron-engine-block1.html. Retrieved 2019, March 10.
- [7] www.mytoyotamirai.com/toyota-mirai-pictures/2016-toyota-fcv-mirai-fuel-cell-sub-frame. Retrieved 2019, July 19.
- [8] Peggs, G. N., Maropoulos, P. G., Hughes, E. B., Forbes, A. B., Robson, S., Ziebart, M., & Muralikrishnan, B. (2009). Recent developments in large-scale dimensional metrology. *Proceedings of the Institution of Mechanical Engineers, Part B: Journal of Engineering Manufacture*, 223(6), 571-595.
- [9] www.gleason.com. Retrieved 2019, July 19.
- [10] en.wikipedia.org/wiki/Rotary_table. Retrieved 2019, July 19.
- [11] www.model-engineer.co.uk/forums/postings.asp?th=91627. Retrieved 2019, July 19.
- [12] www.zollern.com/en. Retrieved 2019, July 19.
- [13] www.schaeffler.de. Retrieved 2019, July 19.

- [14] Rowe, W. B. (2012). *Hydrostatic, aerostatic, and hybrid bearing design*. Elsevier.
- [15] Al-Bender, F. (2009). On the modelling of the dynamic characteristics of aerostatic bearing films: From stability analysis to active compensation. *Precision Engineering*, 33(2), 117-126.
- [16] https://en.wikipedia.org/wiki/Magnetic_bearing. Retrieved 2019, July 19.
- [17] <http://radiantphysics.com/2017/02/08/how-oems-can-afford-magnetic-bearings>. Retrieved 2019, July 19.
- [18] Lu, X. D., Paone, M. P., Usman, I., Moyls, B., Smeds, K., Rotherhofer, G., & Slocum, A. H. (2009). Rotary-axial spindles for ultra-precision machining. *CIRP Annals*, 58(1), 323-326.
- [19] Lei, W. T., Sung, M. P., Liu, W. L., & Chuang, Y. C. (2007). Double ballbar test for the rotary axes of five-axis CNC machine tools. *International Journal of Machine Tools and Manufacture*, 47(2), 273-285.
- [20] ISO 10360-3:2000, Acceptance test and reverification test for CMMs - Part 3: CMMs with the axis of a rotary table as the fourth axis.
- [21] Bryan, J. B. (1982). A simple method for testing measuring machines and machine tools Part 1: Principles and applications. *Precision Engineering*, 4(2), 61-69.
- [22] Bryan, J. B. (1982). A simple method for testing measuring machines and machine tools. Part 2: Construction details. *Precision Engineering*, 4(3), 125-138.
- [23] Lei, W. T., & Hsu, Y. Y. (2002). Accuracy test of five-axis CNC machine tool with 3D probe-ball. Part I: Design and modeling. *International Journal of Machine Tools and Manufacture*, 42(10), 1153-1162.

- [24] Lei, W. T., & Hsu, Y. Y. (2003). Error measurement of five-axis CNC machines with 3D probe-ball. *Journal of Materials Processing Technology*, 139(1-3), 127-133.
- [25] Weikert, S. (2004). R-test, a new device for accuracy measurements on five axis machine tools. *CIRP Annals*, 53(1), 429-432.
- [26] www.ibspe.com. Retrieved 2019, July 19.
- [27] www.fidia.it. Retrieved 2019, July 19.
- [28] Hong, C., & Ibaraki, S. (2013). Non-contact R-test with laser displacement sensors for error calibration of five-axis machine tools. *Precision Engineering*, 37(1), 159-171.
- [29] Zargarbashi, S. H. H., & Mayer, J. R. R. (2009). Single setup estimation of a five-axis machine tool eight link errors by programmed end point constraint and on the fly measurement with Capball sensor. *International Journal of Machine Tools and Manufacture*, 49(10), 759-766.
- [30] Ibaraki, S., Iritani, T., & Matsushita, T. (2012). Calibration of location errors of rotary axes on five-axis machine tools by on-the-machine measurement using a touch-trigger probe. *International Journal of Machine Tools and Manufacture*, 58, 44-53.
- [31] Ibaraki, S., Iritani, T., & Matsushita, T. (2013). Error map construction for rotary axes on five-axis machine tools by on-the-machine measurement using a touch-trigger probe. *International Journal of Machine Tools and Manufacture*, 68, 21-29.
- [32] Zhang, G., Veale, R., Charlton, T., Borchardt, B., & Hocken, R. (1985). Error compensation of coordinate measuring machines. *CIRP Annals*, 34(1), 445-448.

- [33] Schwenke, H., Knapp, W., Haitjema, H., Weckenmann, A., Schmitt, R., & Delbressine, F. (2008). Geometric error measurement and compensation of machines—an update. *CIRP Annals*, 57(2), 660-675.
- [34] Abbaszadeh-Mir, Y., Mayer, J. R. R., Cloutier, G., & Fortin, C. (2002). Theory and simulation for the identification of the link geometric errors for a five-axis machine tool using a telescoping magnetic ball-bar. *International Journal of Production Research*, 40(18), 4781-4797.
- [35] Bringmann, B., & Knapp, W. (2006). Model-based ‘chase-the-ball’ calibration of a 5-axes machining center. *CIRP Annals*, 55(1), 531-534.
- [36] Tsutsumi, M., & Saito, A. (2003). Identification and compensation of systematic deviations particular to 5-axis machining centers. *International Journal of Machine Tools and Manufacture*, 43(8), 771-780.
- [37] Tsutsumi, M., & Saito, A. (2004). Identification of angular and positional deviations inherent to 5-axis machining centers with a tilting-rotary table by simultaneous four-axis control movements. *International Journal of Machine Tools and Manufacture*, 44(12-13), 1333-1342.
- [38] Suh, S. H., Lee, E. S., & Jung, S. Y. (1998). Error modelling and measurement for the rotary table of five-axis machine tools. *The International Journal of Advanced Manufacturing Technology*, 14(9), 656-663.
- [39] Lion Precision, www.lionprecision.com
- [40] Schwenke, H., Schmitt, R., Jatzkowski, P., & Warmann, C. (2009). On-the-fly calibration of linear and rotary axes of machine tools and CMMs using a tracking interferometer. *CIRP Annals*, 58(1), 477-480.

- [41] Zargarbashi, S. H. H., & Mayer, J. R. R. (2006). Assessment of machine tool trunnion axis motion error, using magnetic double ball bar. *International Journal of Machine Tools and Manufacture*, 46(14), 1823-1834.
- [42] Lei, W. T., Sung, M. P., Liu, W. L., & Chuang, Y. C. (2007). Double ballbar test for the rotary axes of five-axis CNC machine tools. *International Journal of Machine Tools and Manufacture*, 47(2), 273-285.
- [43] Lee, K. I., Lee, D. M., & Yang, S. H. (2012). Parametric modeling and estimation of geometric errors for a rotary axis using double ball-bar. *The International Journal of Advanced Manufacturing Technology*, 62(5-8), 741-750.
- [44] Lee, K. I., & Yang, S. H. (2013). Robust measurement method and uncertainty analysis for position-independent geometric errors of a rotary axis using a double ball-bar. *International Journal of Precision Engineering and Manufacturing*, 14(2), 231-239.
- [45] Kunzmann, H., Schepperle, K., Trieb, G., & Wäldele, F. (1989). U.S. Patent No. 4,819,339. Washington, DC: U.S. Patent and Trademark Office.
- [46] Evans, C. J., Hocken, R. J., & Estler, W. T. (1996). Self-calibration: reversal, redundancy, error separation, and 'absolute testing'. *CIRP Annals*, 45(2), 617-634.
- [47] Troughton, E. (1832). An account of a method of dividing astronomical and other instruments, by ocular inspection; in which the usual tools for graduating are not employed; the whole operation being so contrived, that no error can occur but what is chargeable to vision, when assisted by the best optical means of viewing and measuring minute quantities. In: *Abstracts of the Papers Printed in the Philosophical*

Transactions of the Royal Society of London (Vol. 1, pp. 323-325). The Royal Society.

- [48] Reeve, C.P. (1975). The calibration of indexing table by subdivision, NBSIR 75-750.
- [49] Kniel, K., Härtig, F., Osawa, S., & Sato, O. (2009). Two highly accurate methods for pitch calibration. *Measurement Science and Technology*, 20(11), 115110.
- [50] Osawa, S., Busch, K., Franke, M., & Schwenke, H. (2005). Multiple orientation technique for the calibration of cylindrical workpieces on CMMs. *Precision Engineering*, 29(1), 56-64.
- [51] Härtig, F. & Kniel, K. (2007). Fehlertrennverfahren: ein Weg zu hochgenauen Verzahnungsmessungen. In: GETPRO—Kongress zur Getriebeproduktion, Würzburg, Germany.
- [52] Günther, A., Stöbener, D., & Goch, G. (2016). Self-calibration method for a ball plate artefact on a CMM. *CIRP Annals*, 65(1), 503-506.
- [53] Hocken, R. J., & Pereira, P. H. (2016). *Coordinate measuring machines and systems*. CRC Press.
- [54] ASME B89.3.4:2010, *Axes of rotation: methods for specifying and testing*.
- [55] ISO 10360-2: 2009, *Acceptance test and reverification test for CMMs - Part 2: CMMs used for measuring linear dimensions*.
- [56] Craig, L. D., & Boulet, J. A. M. (1999). Deflections of a uniformly loaded circular plate with multiple support points. NASA/TM-1999-209631.
- [57] <https://www.hexagonmi.com/products/coordinate-measuring-machines/cmm-sensors/non-contact-sensors/hp-o-optical-sensors>. Retrieved 2019, July 19.